Cell Systems

Article

Biphasic JNK-Erk signaling separates the induction and maintenance of cell senescence after DNA damage induced by topoisomerase II inhibition

Graphical abstract

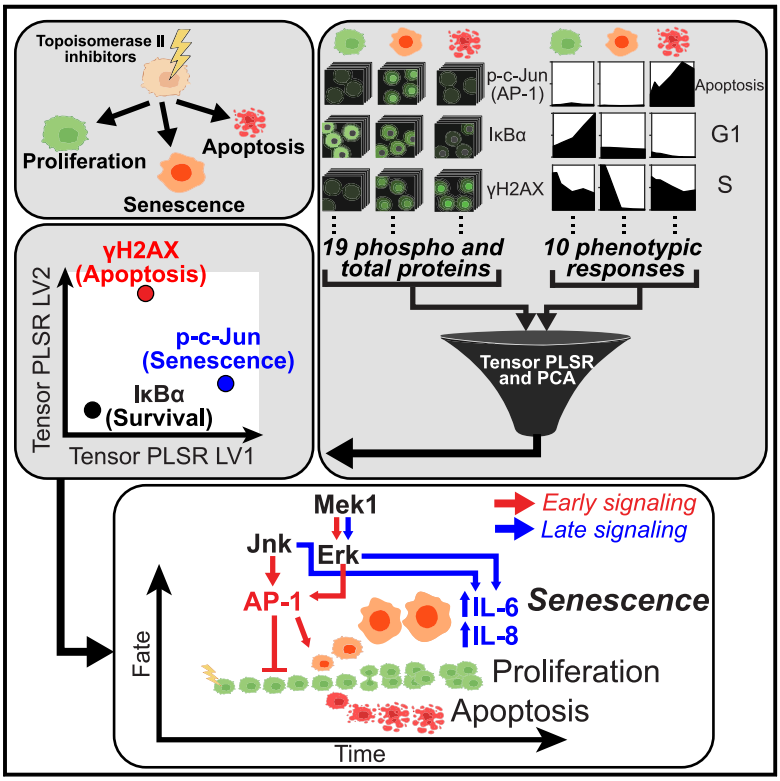

Highlights

DNA damage from topoisomerase II inhibitors induces senescence through phospho-c-Jun

JNK and Erk MAPK activity within 12 h of damage controls senescence through c-Jun

Late JNK and Erk MAPK activity after 12 h controls cytokine release during the SASP

Tensor PLSR and PCA can be used to map cell phenotypes to specific signaling dynamics

Authors

Tatiana S. Netterfield, Gerard J. Ostheimer, Andrea R. Tentner, ..., Kevin A. Janes, Douglas A. Lauffenburger, Michael B. Yaffe

Correspondence

myaffe@mit.edu

In brief

Netterfield and colleagues used a two-pronged tensor PLSR and PCA approach to link upstream signaling events to downstream cell fates after topoisomerase II inhibition in cancer cells, identifying roles for γH2AX in apoptosis, early JNK and Erk activity in senescence induction, and late JNK/Erk activity in cytokine secretion during the SASP.

Netterfield et al., 2023, Cell Systems 4, 582–604
July 19, 2023
https://doi.org/10.1016/j.cels.2023.06.005

CellPress

CellPress

Cell Systems

Article

Biphasic JNK-Erk signaling separates the induction and maintenance of cell senescence after DNA damage induced by topoisomerase II inhibition

Tatiana S. Netterfield,[1,2,3,9] Gerard J. Ostheimer,[1,4,9] Andrea R. Tentner,[1] Brian A. Joughin,[1,2,3,4] Alexandra M. Dakoyannis,[1,2,3] Charvi D. Sharma,[2,3,5] Peter K. Sorger,[6] Kevin A. Janes,[7] Douglas A. Lauffenburger,[1,2] and Michael B. Yaffe[1,2,3,4,8,10,*]

[1]Department of Biological Engineering, Massachusetts Institute of Technology, Cambridge, MA 02139, USA
[2]David H. Koch Institute for Integrative Cancer Research, Massachusetts Institute of Technology, Cambridge, MA 02139, USA
[3]Center for Precision Cancer Medicine, Massachusetts Institute of Technology, Cambridge, MA 02139, USA
[4]Department of Biology, Massachusetts Institute of Technology, Cambridge, MA 02139, USA
[5]Department of Computer Science and Molecular Biology, Massachusetts Institute of Technology, Cambridge, MA 02139, USA
[6]Laboratory of Systems Pharmacology, Department of Systems Biology, Harvard Medical School, Boston, MA 02115, USA
[7]Department of Biomedical Engineering and Department of Biochemistry & Molecular Genetics, University of Virginia, Charlottesville, VA 22908, USA
[8]Division of Acute Care Surgery, Trauma, and Surgical Critical Care, and Division of Surgical Oncology, Department of Surgery, Beth Israel Deaconess Medical Center, Harvard Medical School, Boston, MA 02215, USA
[9]These authors contributed equally
[10]Lead contact
*Correspondence: myaffe@mit.edu
https://doi.org/10.1016/j.cels.2023.06.005

SUMMARY

Genotoxic stress in mammalian cells, including those caused by anti-cancer chemotherapy, can induce temporary cell-cycle arrest, DNA damage-induced senescence (DDIS), or apoptotic cell death. Despite obvious clinical importance, it is unclear how the signals emerging from DNA damage are integrated together with other cellular signaling pathways monitoring the cell s environment and/or internal state to control different cell fates. Using single-cell-based signaling measurements combined with tensor partial least square regression (t-PLSR)/principal component analysis (PCA) analysis, we show that JNK and Erk MAPK signaling regulates the initiation of cell senescence through the transcription factor AP-1 at early times after doxorubicin-induced DNA damage and the senescence-associated secretory phenotype (SASP) at late times after damage. These results identify temporally distinct roles for signaling pathways beyond the classic DNA damage response (DDR) that control the cell senescence decision and modulate the tumor microenvironment and reveal fundamental similarities between signaling pathways responsible for oncogene-induced senescence (OIS) and senescence caused by topoisomerase II inhibition. A record of this paper s transparent peer review process is included in the supplemental information.

INTRODUCTION

Eukaryotic cells recognize and respond to DNA damage by activating an evolutionarily conserved set of signaling pathways that are essential for maintaining genomic integrity and preventing cancer.[1,2] These DNA damage response (DDR) signaling pathways regulate DNA damage-induced cellular activities and outcomes, including DNA repair, cell-cycle arrest, senescence, and apoptosis.[3,4] Cellular senescence and apoptosis are actively regulated cellular responses that reduce the likelihood of cancer by preventing cells with genomic damage (or cells at risk of genomic damage) from proliferating.[5–8] Mutations and/or acquired defects that compromise the function of these DDR pathways result in enhanced mutagenesis and underlie the development and progression of cancer.[9–11]

In the canonical DDR signaling pathway, double-stranded breaks (DSBs) in DNA stimulate the kinase activity of ATM that phosphorylates and recruits a suite of proteins, including the histone variant H2AX, thereby creating detectable foci of DDR proteins in the area adjacent to the DSB.[1–3,12] ATM effectors include the checkpoint kinases Chk2, Chk1, and MAPKAP kinase-2 (MK2) and the multi-functional transcription factor p53, which together communicate DNA damage to the cellular machinery responsible for cell-cycle arrest and the induction of programmed cell death.[13] p53 is a central node in the DDR signaling network that contributes to transient cell-cycle arrest and

senescence by upregulating the cyclin-dependent kinase inhibitor (CDKI) $p21^{Waf1}$ and to apoptosis by transactivation of pro-apoptotic Bcl-2 protein family members.[14–17] Tumor cells often have mutations in DDR components, including p53, which allows the evasion of normal cell-cycle control mechanisms and contributes to genomic instability. However, such defects can also sensitize tumor cells to killing and/or cell-cycle arrest and senescence by classical DNA-damaging agents, such as ionizing radiation (IR) and chemotherapies used to treat cancer.[18–21]

Cellular senescence is a "catch-all" term that refers to three classes of irreversible cell-cycle arrest—replicative senescence (RS), oncogene-induced senescence (OIS), and DNA damage-induced senescence (DDIS).[22] RS occurs after eukaryotic cells have undergone sufficient rounds of replication to cause exposure of unprotected telomeric DNA, resembling an un-repairable DNA double-strand break (DSB). This triggers DDR signaling, resulting in permanent cell-cycle arrest.[23–25] OIS occurs when oncogene expression results in inappropriately high levels of proliferation, leading to DNA replication stress and collapsed replication forks. The resulting DSBs induce a DDR-dependent permanent cell-cycle arrest.[5,9] DDIS occurs after exposure to sub-apoptotic, "intermediate" levels of DNA damage-inducing agents, such as IR and doxorubicin, that are too high for repair and cell-cycle re-entry but not high enough to induce cell death.[6,15] Senescent cells of all three classes are viable, metabolically active, enlarged, and/or flattened in morphology and strongly positive for CDKIs, persistent DNA damage-induced foci (PDDF), and senescence-associated heterochromatic foci (SAHF).[26] In addition, senescent cells secrete a panel of inflammatory cytokines featuring high levels of IL-6 and IL-8.[27–31] Campisi and co-workers showed that this senescence-associated secretory phenotype (SASP) requires DDR[28] and p38/NF-κB[32] signaling. Although DDR signaling is fundamental to regulation of the senescent cell fate, the additional role of cytokine signaling pathways has not been as clearly defined.

DNA damage-induced cell commitment to either cell-cycle arrest, senescence, or apoptosis likely involves integrating DDR signaling with additional signaling pathways governing general stress and survival responses such as the PI 3-kinase/Akt pathway, the NF-κB pathway, and the stress- and mitogen-activated protein kinase (SAPK/MAPK) pathways. Since cell stress and extracellular signals are both transduced through these pathways, they may serve as information-processing junctions that integrate signals from the microenvironment with DDR signaling. Previous studies have indicated roles for the ERK, JNK, and p38 SAPK/MAPK pathways in cell-fate determination after DNA damage.[33–37] However, the relative importance of these additional signal transduction pathways, and the manner and timing by which their signals are integrated together with those from the canonical DDR pathways to control the outcome of DNA-damaged cells, is not well understood. Therapeutic rewiring of these pathways could lead to the engineering of cellular outcomes and improving the clinical response of tumors to canonical genotoxic therapies.[38–42]

To investigate cell-fate determination after DNA damage in a systematic manner, we undertook a quantitative time-resolved cell signaling and phenotypic response study in the U2OS osteosarcoma cell line exposed to different levels of doxorubicin-induced DNA damage with the intention of using data-driven models to suggest novel relationships between signaling activity and cellular outcomes. We were particularly interested in identifying signaling events that denoted different temporal stages on the paths to senescence and apoptosis. A senescing cell actively re-wires its molecular signaling networks to permanently arrest its cell cycle, become insensitive to serum stimulation, change its morphology, and produce the associated secretory phenotype. We sought to identify the signaling pathways and their activity dynamics that control the transition from a proliferating cancer cell to a senescent cell.

Here, we report that the transcription factor AP-1 and its upstream activators, the stress- and mitogen-activated protein kinases JNK and Erk, play important roles in the cell-fate decision to senesce at arrest-inducing (but non-lethal) doses of DNA damage at early times and contribute to the DNA damage-induced SASP at later times. Our findings derive from a structured, multidimensional dataset (tensor) of signaling and DNA damaged-induced responses collected in U2OS cells treated with various doses of doxorubicin at multiple times. The data were modeled by tensor- and matrix-factorization approaches to yield predictions about critical time-dependent signals, which were verified by independent experimental tests. Taken together, this systems analysis points to a fundamental role for SAPK/MAPK signaling in the regulation of DDIS and the SASP along separable distinct timescales and reveals similarities between the signaling events responsible for both OIS and DDIS.

RESULTS

A cue-signal-response framework for interrogating cell-fate choice after DNA damage

DNA-damaging agents induce cells to undergo cell-cycle arrest, followed by either DNA repair and cell-cycle re-entry, DDIS, or apoptotic cell death. To quantitatively map the DNA damage cue-signal-response landscape,[43] we systematically profiled human U2OS osteosarcoma cells treated with a range of doxorubicin doses (Figure 1A). Doxorubicin—a commonly used chemotherapeutic agent used to treat a variety of human malignancies including osteosarcoma—not only induces DNA double-strand breaks (DSBs) primarily by inhibiting topoisomerase II but also generates reactive oxygen species[44] and acts as an intercalating agent.[45] U2OS cells were selected for study because they are widely used in studies of DNA damage signaling,[37,40,46] express wild-type p53, and undergo a full range of DNA damage-induced cellular responses, including p53-dependent cell-cycle arrest and apoptosis. U2OS cells do not express the CDKI p16 because their *INK4* locus has been silenced by methylation; nonetheless, this cell line is fully capable of undergoing senescence.[5,47]

U2OS cells were treated with 0.5, 2, or 10 μM doxorubicin or carrier for 4 h, followed by media replacement. Individual cells were assayed for signaling events and phenotypic outcomes at 6, 12, 24, 48, 72, and 96 h after the start of treatment (Figure 1B). In addition, cell morphology was examined by Whole Cell Blue (WCB) staining, and cell proliferation was assessed by bromodeoxyuridine (BrdU) labeling and immunohistochemical detection at 96 h after treatment. Mock-treated U2OS cells actively proliferated during the 4 days after treatment as shown by increased cell density and BrdU incorporation (Figure 1C). By

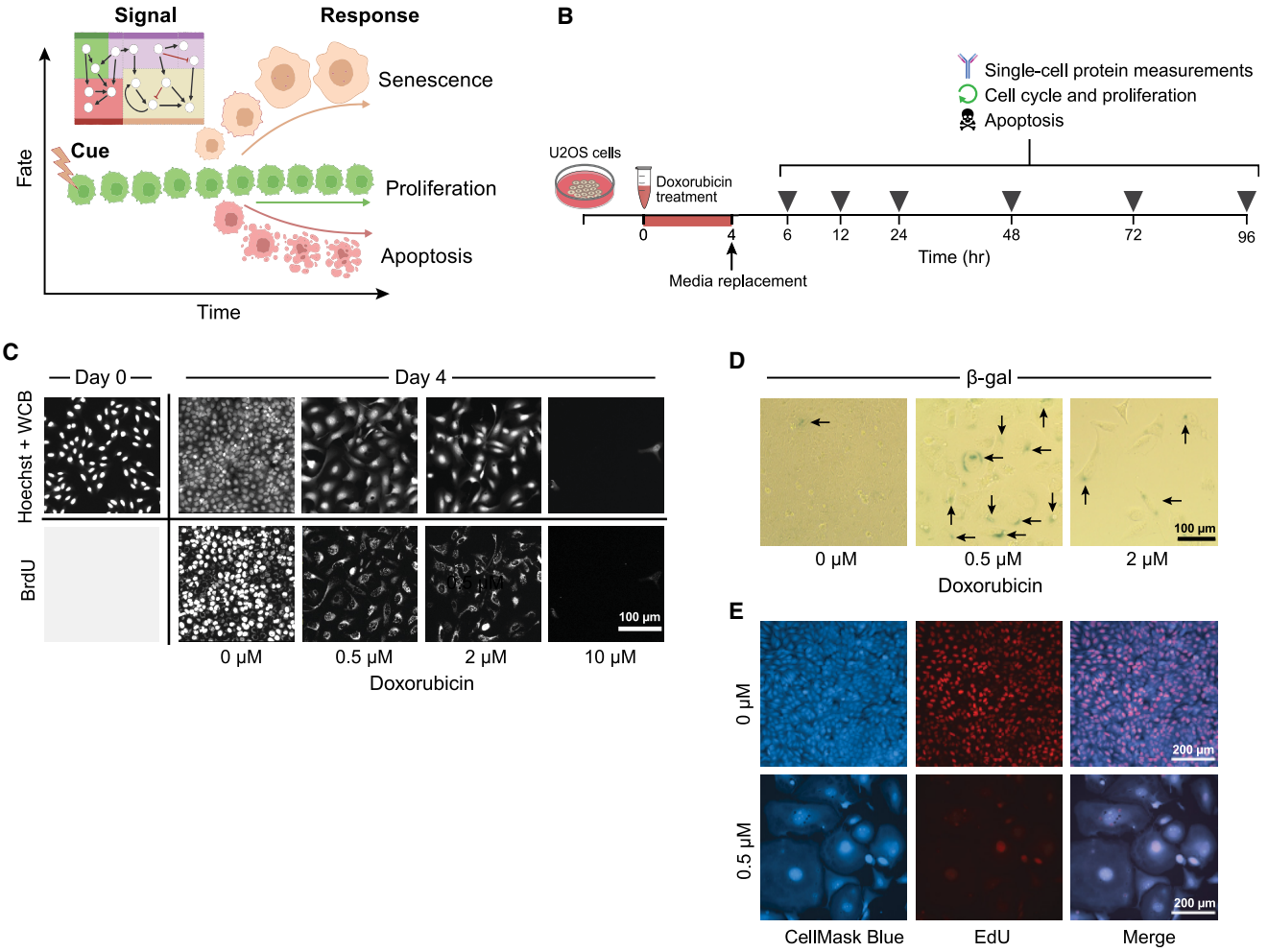

Figure 1. A cue-signal-response framework for cell-fate decisions after DNA damage

(A) Cartoon of cell fates of interest vs. time after DNA damage, created with BioRender.com.

(B) A schematic of how the signaling and response data were collected, using icons created in BioRender.com. For details, see text.

(C) U2OS cells were treated with a 4-h pulse of either with DMSO (0 μM) or 0.5, 2, or 10 μM doxorubicin and fixed 4 days after treatment. Hoechst and Whole Cell Blue (WCB) dye were used to visualize cell morphology, whereas immunofluorescence for BrdU DNA incorporation was used to label proliferating cells. Images are representative of 20–400 individual cells, depending on the doxorubicin dose.

(D) β-galactosidase activity was measured by colorimetric staining in fixed U2OS cells 4 days after doxorubicin treatment. Black arrows denote positively stained cells. Images are representative of 100–500 individual cells, depending on the doxorubicin dose.

(E) Cells were either treated with DMSO (0 μM) or with 0.5 μM doxorubicin and then fixed 6 days later. Cell morphology was visualized with HCS CellMask Blue and proliferation with EdU DNA incorporation. CellMask Blue channel was processed with a gamma of 0.5 to better visualize the cytoplasmic compartment. Images are representative of 100 (0.5 μM) and 1,000 (0 μM) individual cells.

contrast, both the 0.5 and 2 μM doxorubicin treatments arrested proliferation, as shown by the absence of nuclear BrdU incorporation. These doses of doxorubicin induced a change in morphology that is consistent with cellular senescence—cell size and nuclear size increased over the 4-day time course, and the cells assumed a "fried egg" appearance.[48] Interestingly, non-proliferating cells showed perinuclear BrdU staining after 24 h of exposure to BrdU, likely resulting from BrdU incorporation into RNA[49] that suggests metabolically activity is retained, although the cells are not proliferating. Further evidence indicating the induction of cell senescence following treatment with these lower doses of doxorubicin was obtained by combined EdU labeling and CellMask Blue staining and by staining the cells for β-galactosidase (Figures 1D and 1E). By contrast, treatment with 10 μM doxorubicin resulted in profound cell death, with nearly all cells eliminated by day 4 of the time course (Figure 1C).

To further quantify the cellular responses to varying doses of doxorubicin in a manner appropriate for distinguishing the behavior of distinct sub-populations of cells, we used quantitative live cell imaging (Incucyte) to measure cell proliferation, flow cytometry to monitor apoptotic, and cell-cycle responses at the single-cell level. Flow cytometry measurements of apoptosis were performed by immunostaining the cells for simultaneous activation of the executioner caspase, caspase-3, and cleavage of PARP, a caspase-3 substrate[50] (Figure 2A). DMSO

and 0.5 μM doxorubicin treatments did not induce apoptotic cell death, whereas 2 μM doxorubicin induced a small fraction of U2OS cells to undergo apoptosis at early times after treatment, but this early burst of apoptosis subsided by 72 h after treatment (Figures 2Bi and S1). By contrast, 10 μM doxorubicin treatment induced a significant fraction of cells to apoptose over the entire 4-day time course with a biphasic response, resulting in the complete absence of proliferation and the death of nearly all cells by the conclusion of the experiment (Figures 2Bi and 2Bii). The cell number of DMSO-treated cells continued to increase over the 4-day time course, consistent with ongoing proliferation, which was eliminated by treatment with as little as 0.5 μM doxorubicin (Figure 2Bii).

Flow cytometry of propidium iodide (PI)-stained cells was used to monitor the progression of U2OS cells through the cell cycle following treatment with doxorubicin (Figure 2C). DNA replication activity was independently measured by analyzing the fraction of cells that incorporate BrdU in a 4-h pulse (Figure 2D). Mock-treated cells continue to proliferate, with cells distributed through all phases of the cell cycle. Cells treated with 0.5 and 2 μM doxorubicin proceeded through S phase and arrested with ~80% or more of the cells in G2/M and the remaining cells in G1 (Figures 2C and 2D), which developed over the course of 24–48 h (Figures 2Biii–2Bv and S1). By contrast, under these treatment conditions, cells treated with 10 μM doxorubicin did not develop a pronounced G2 arrest but instead entered and remained arrested in S phase, where they incorporated only low levels of BrdU and did not progress to G2 (Figures 2Biv, 2Bv, and 2D). This finding is consistent with our previous work indicating that this type of pulse doxorubicin treatment induced U2OS cells to undergo apoptosis in early S phase.[35] Cells were then stained for the presence or absence of cyclin B and the CDKI $p21^{Waf1}$ (Figures 2Bvi–2Bix, 2E, and 2F). Consistent with the observed G2 arrest, 0.5 and 2 μM dox treatments caused a marked upregulation of the $p21^{Waf1}$, whereas the apoptosis-inducing 10 μM dose did not (Figures 2Bix and 2E). Cells arrested in G2 initially possessed high levels of cyclin B as would be expected; however, concomitant with the increase in p21, the level of cyclin B in these cells decreased to that of G1 cells (Figures 2Bvi, 2Bvii, 2Bix, 2F, and S1), indicating that low and intermediate doses of doxorubicin caused the cells to gradually lose the ability to transition from G2 to M phases. Taken together, these data indicate that 0.5 and 2 μM doxorubicin treatments arrest proliferation by inducing a G2 arrest that prevents cells from progressing into mitosis. Similar to other cancer cell lines in which p16 has been silenced by methylation,[51,52] a fraction of U2OS cells endoreduplicated in response to DNA damage as indicated by uptake of BrdU in cells containing >4N DNA (Figure 2Bx).

To quantify the cell signaling response to different levels of DNA damage, 26 total measurements including the relative protein levels, protein phosphorylation, sub-cellular localization within the nuclear and cytoplasmic compartments, and heterogeneity between cellular sub-populations, for 19 signaling proteins representing key regulatory network nodes for cell-cycle control, apoptosis, DDR, and stress response signaling events (Figure 3A) were quantified in 96-well plates using singleplex immunofluorescence (IF) microscopy at 6 time points: 6, 12, 24, 48, 72, and 96 h after doxorubicin treatments. Representative signaling data at the 48-h time point are shown in Figure 3B, with the complete quantified time courses shown in Figures 3C, S2, and S3. As expected, treatment of U2OS cells with doxorubicin strongly activated the DDR, including the upregulation of γH2AX, stabilization of p53, and phosphorylation of the effector kinase Chk2 (Figures 3B, 3C, and S3). Interestingly, the DDIS-inducing doses of doxorubicin (0.5 and 2 μM) increased the level of p53 more than the apoptosis-inducing dose (10 μM). In addition, these DDIS-inducing doses induced a large increase in the level of the CDKI $p21^{Waf1}$, which likely contributes to the U2OS cell-cycle arrest, given the silencing by methylation of the p16 gene in this cell line (Figures 3B and 3C).[47]

Cell-cycle arrest is a fundamental component of the DDR. Consequently, we monitored the levels and localization of cyclins A, B, D, and E, as well as phosphorylation of the retinoblastoma (Rb) protein (Figures 3B, 3C, and S3). In DMSO-treated cells, the levels of these cell-cycle-regulating proteins remained largely unchanged for the 4-day duration of the experiment. The G2 arrest of the cells treated with 0.5 and 2 μM doxorubicin was reflected in the accumulation of cyclins A and B. Interestingly, U2OS cells undergoing DDIS accumulate cyclin E, indicating that they may be primed for another round of DNA replication. This is consistent with our previous data that HCT116 cells, which like U2OS cells have wild-type p53 and lack p16, also arrest in G2 after DNA damage and accumulate cyclin E, putting them in a 4N pseudo-G1 state that likely contributes to their propensity for endoreduplication.[52] A small percentage (3%–4%) of U2OS cells also endoreduplicated after DNA damage as shown by a population of 8N cells after the 0.5 and 2 μM doxorubicin treatments (Figure S1).

Since signal transduction pathways other than the canonical DDR signaling network also contribute to cell-fate determination, we measured the post-translational modifications and protein levels reflective of Akt, Erk, JNK, p38, and NF-κB activity (Figures 3B, 3C, and S2). These pathways exhibit complicated, time- and doxorubicin-dose dependent behaviors that required data-driven modeling to integrate with the canonical DDR signaling network and downstream cell-fate responses.[53]

A t-PLSR model distinguishes alternative cell fates after DNA damage

To relate these complex time- and dose-dependent changes in cellular signaling to the observed phenotypic responses, we used tensor partial least square regression (t-PLSR) to identify signals, responses, and time points that correlate with specific cell fates. Traditional "unfolded" PLSR is a widely used dimensional reduction modeling method in which the relationship between measured signaling events and phenotypic responses is inferred from maximizing the covariance between the two.[50,54] Independent signals, dependent cellular responses, and time points are weighed separately in the PLSR matrix formulation. By contrast, t-PLSR specifically preserves the natural structure of the data, regressing the stimulus-time point-response/cell-fate tensor on the stimulus-time point-signaling tensor, linking these tensors via regression coefficients.[55,56] In addition to providing insights into how particular aspects of temporally evolving signaling activities are important for making predictions, t-PLSR models use fewer parameters than unfolded

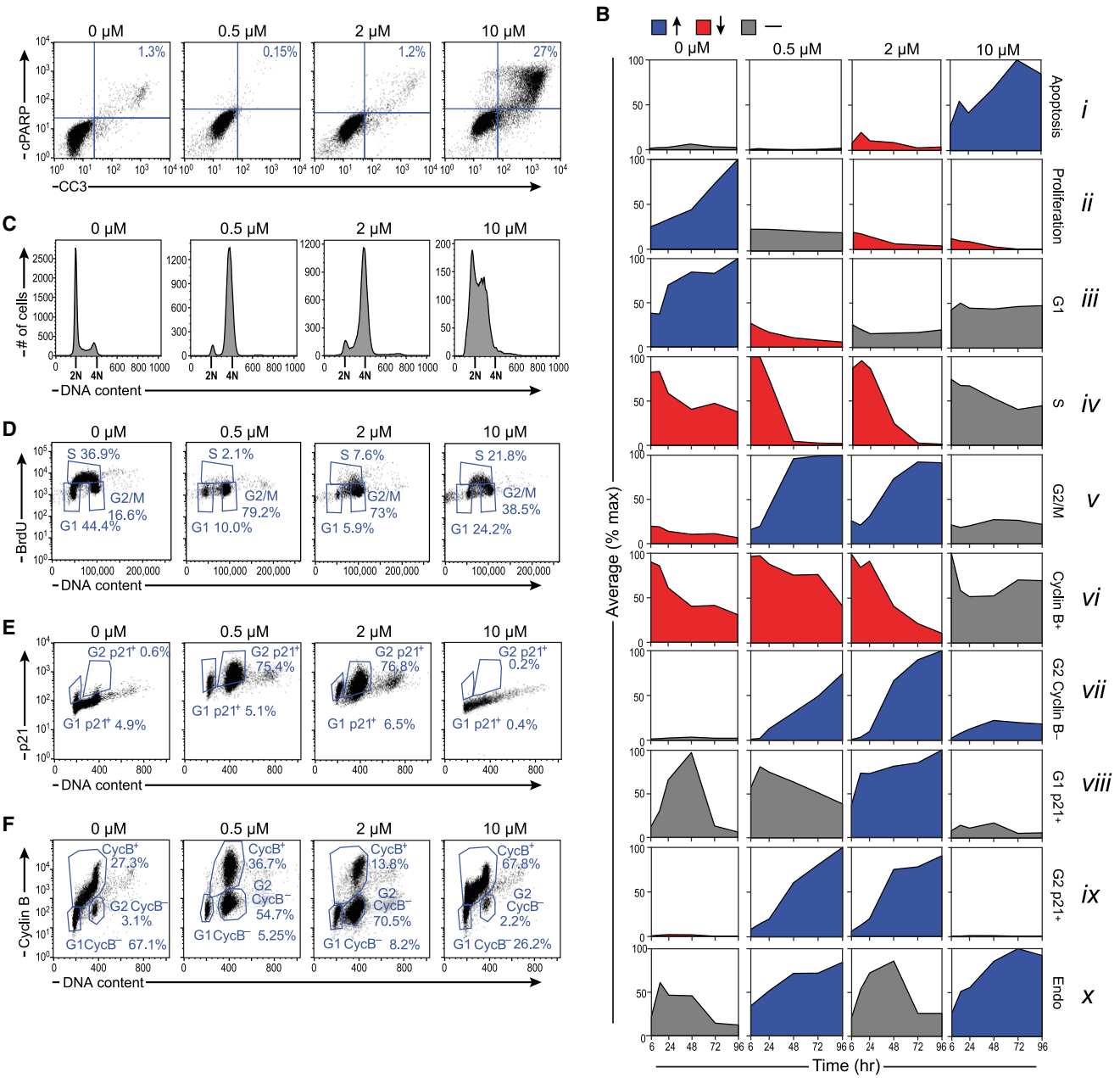

Figure 2. DNA damage induces G2/M arrest with dose-dependent differences between senescent p21^{hi}/cyclin B^{lo} cells and apoptotic p21^{lo} cells

(A) Representative flow cytometry scatter plot measuring apoptotic cells with cleaved caspase-3 (CC3) and cleaved PARP (cPARP) double positivity in U2OS cells 48 h after doxorubicin treatment.

(B) Summary plots of mean phenotypic values (normalized to the maximum value across time and drug treatments) vs. time. Blue indicates a measurement that increases over time, red indicates a measurement that decreases, and gray indicates a measurement that remains the same. Tick marks represent 6, 24, 48, 72, and 96 h after doxorubicin treatment. For boxplots of raw response data overlaid with replicate values, see Figure S1.

(C) Histograms of DNA content in U2OS cells stained with propidium iodide (PI) 48 h after doxorubicin treatment. 2N and 4N DNA content are annotated on the x axis of the histogram plots.

(D) Representative flow cytometry scatter plots of BrdU antibody staining vs. PI staining in U2OS cells 48 h after doxorubicin treatment.

(E) Representative flow cytometry scatter plot of p21 antibody staining vs. PI staining in U2OS cells 96 h after doxorubicin treatment.

(F) Representative flow cytometry scatter plot of cyclin B antibody staining vs. PI staining in U2OS cells 96 h after doxorubicin treatment.

PLSR, resulting in less overfitting, which is of particular importance when modeling a small number of treatments, as in our case.

In t-PLSR, the signal (X) and response (Y) tensors are simultaneously decomposed into three distinct individual matrices for each tensor: treatment scores (s_x or s_y), signal (w_{sx}) or response

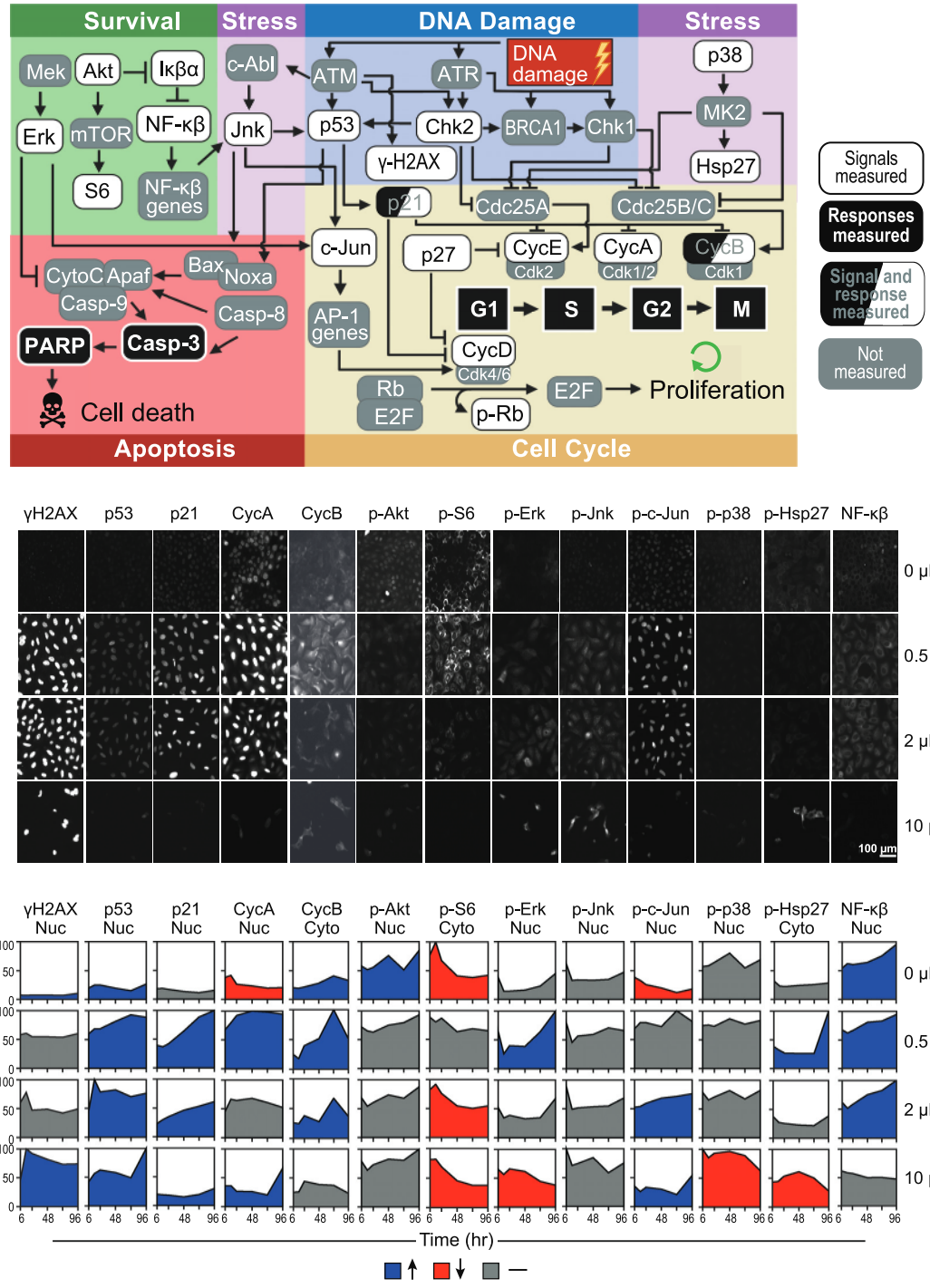

Figure 3. Quantitative single-cell measurements define the DNA damage signaling landscape

(A) A wiring diagram of the signaling network that modulates cell-cycle progression and apoptosis after DNA damage, created with BioRender.com.

(B) Representative immunofluorescence images of a subset of signaling proteins measured 48 h after doxorubicin treatment. Each field of view represents a distinct well on a 96-well plate that was immunostained for 1 total or phosphoprotein. Images representative of 250–6,000 individual cells per biological replicate, depending on the dose of doxorubicin.

(C) Quantification of the mean fluorescence intensity (normalized to the maximum value across time and drug treatments) over time in either the nuclear or cytoplasmic compartment, depending on the given protein measured. Blue indicates a measurement that increases over time, red indicates a decreasing measurement, and gray indicates a measurement that has remained the same. Tick marks on the x axis represent 6, 24, 48, 72, and 96 h. For boxplots of raw signal data overlaid with replicate values, see Figure S2.

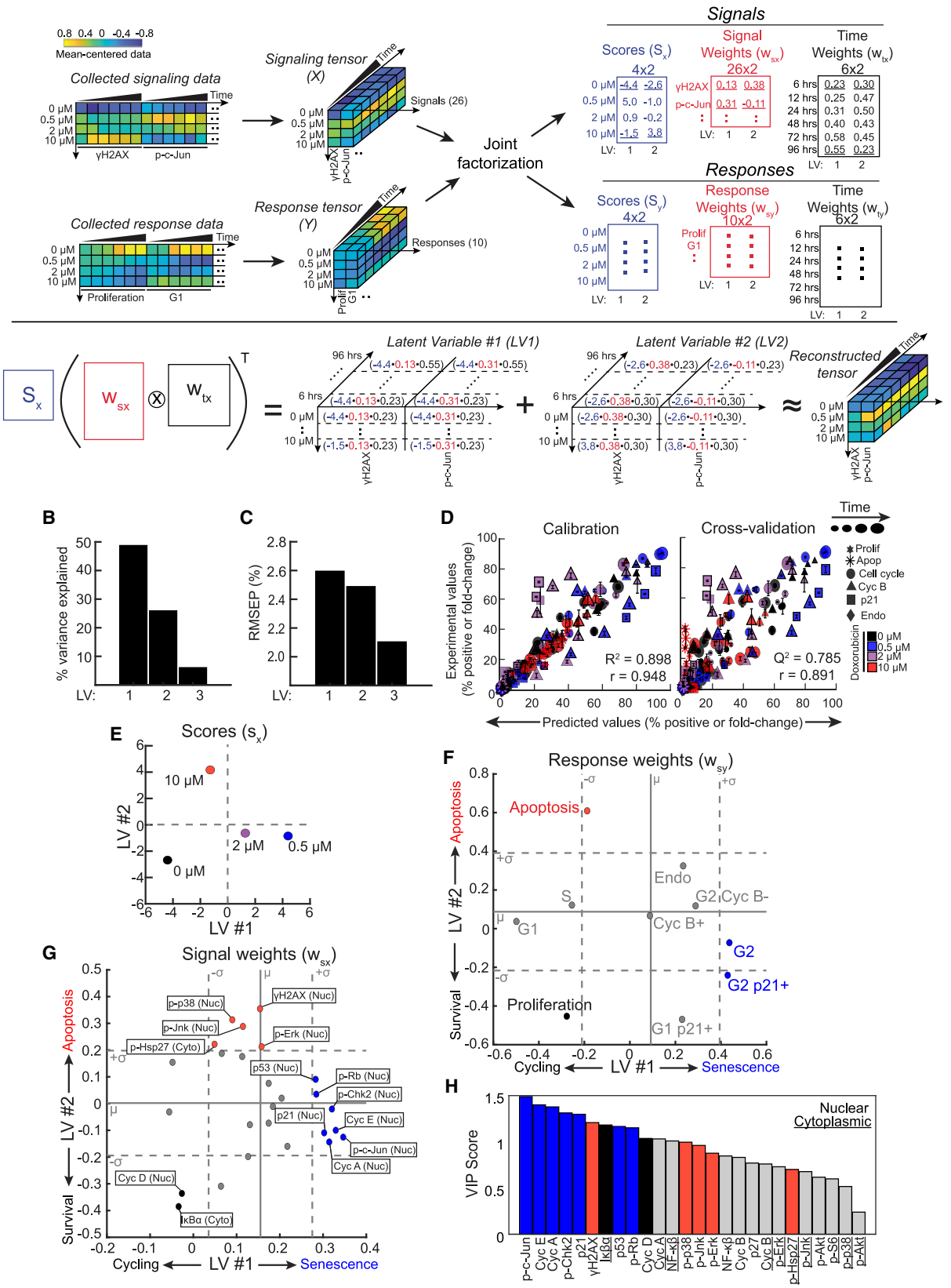

legend on next page)

(w_{sy}) weights, and time weights (w_{tx} or w_{ty}) (Figure 4A). To generate these matrices, the signaling tensor X and the cellular response tensor Y are jointly factored using a linear relationship between s_x and s_y in which the regression coefficients matrix is the slope within this relation, and this factorization occurs iteratively until the covariance between X and Y has been maximized. Upon convergence, these values are considered the score and weight values for latent variable 1 (LV1), which is conceptually analogous to principal component 1 (PC1) in traditional unfolded PLSR. The residuals are then subtracted from X and Y to compose the tensors used for the next round of factorization, which will be used to compute latent variable 2 (LV2), and so on, until a majority of the variance in the data has been explained. Treatment scores describe where certain treatments fall in the LV space, whereas signal and response weights describe the contribution of each individual signal or response to a specific LV. Time weights offer additional insights into which time points are weighted more heavily across all signals and responses in constructing a specific LV, information that is difficult to parse in traditional unfolded PLSR. As shown in Figure 4A, the appropriate product of these scores and weights, when added over all LVs, recapitulates the original signaling or response tensor.

A t-PLSR model containing three LVs captured greater than 80% of the variance in the response data while also minimizing the root-mean-square error of prediction (Figures 4B and 4C), with over 75% of the variance explained by LVs 1 (LV1) and 2 (LV2). There was good concordance between the predicted and experimentally observed phenotypic responses during both model calibration and cross-validation (Figure 4D). The largest discrepancies between the experimental and predicted values were observed at the 2 μM doxorubicin dose, likely due in part to the heterogeneity of cell-fate responses observed at this particular dose (~25% cumulative apoptosis and ~75% senescence) (Figure S4A). When examining different phenotypic responses, rather than specific drug doses, the model performed best at predicting the percentage of cells in G1, S, and G2/M in both the calibration and cross-validation data with Q^2 values greater than 0.64 (Figure S4B).

To gain insights into how these LVs correlated with cell fates, the treatment scores and the response weights from the model were explored. Plotting the treatment scores on LV1 vs. LV2 revealed that DMSO treatment fell in LV1 and LV2 negative quadrant, whereas the treatment scores of both doses of doxorubicin that induced senescence (0.5 and 2 μM) were LV1 positive and LV2 negative. Treatment with the 2 μM dose, which induces a more heterogeneous mix of senescent and apoptotic cells, projected less positively on LV1 than did the 0.5 μM dose. By contrast, the treatment score of the apoptotic dose of doxorubicin (10 μM) projected negatively on the LV1 axis but was strongly LV2 positive (Figure 4E). Thus, treatments involving senescent doses of this genotoxic agent are distributed along LV1 while LV2 distinguished the apoptotic dose treatment from the rest.

To further refine the biological meaning of LV1 and LV2, the cellular response weights were plotted, and the significance of their projections on these axes was evaluated using statistical bootstrapping (Figure 4F).[57] 500 separate null models were constructed from randomly shuffled data, and the observed response weights corresponding to the real data then compared with those obtained from the null models. Responses whose weights were greater than one standard deviation from the mean of the null models were considered significant. Using this cutoff, proliferation emerged as significant within the negative LV1 and LV2 quadrants, whereas the G2 and G2 p21+ states emerged as the only significant responses that were LV1 positive (Figure 4F). This observation indicates that G2 arrested/senescent cells are separated from cycling proliferative cells by progression along the LV1 axis, in excellent agreement with the distribution of senescence-inducing treatment scores along this axis (2 and 0.5 μM doxorubicin; Figure 4E). By contrast, apoptosis emerged as the only response that was significantly positive along the LV2 axis, in excellent agreement with the observation that the treatment score for the apoptotic dose of doxorubicin projected strongly in the positive LV2 direction. Measurements of the G1 and S phase cell populations were not significantly distributed along the LV2 axis, they were significant on the negative LV1 axis (Figure 4F), consistent with the location of actively cycling cells. The apoptosis response was narrowly below the cutoff for significance on the LV1 axes, which is consistent with the observation that cells treated with the apoptotic dose of doxorubicin maintained steady levels of cells in G1 and S that were not dissimilar from cells treated with the DMSO vehicle control (Figures 2Biii and 2Biv). Taken together, these observations, paired with the treatment scores, indicate that LV1 reflects a cycling vs. senescence axis, whereas LV2 reflects survival vs. apoptosis.

t-PLSR and PCA identify signaling pathways that dictate cell fate

Interrogation of where specific molecular signals fall on the LV1 and LV2 axes of the model can infer potential causal

Figure 4. A tensor PLSR model identifies latent variables that define a survival-apoptosis axis and a cycling-senescence axis

(A) A schematic of the "tensor" PLSR (t-PLSR) algorithm. The transpose of Khatri-Rao product of the computed w_{sx} and w_{tx} multiplied by the computed s_x should be able to fairly recapitulate the original tensor, as illustrated.

(B) Barplots of the percent variance explained by each latent variables (LVs).

(C) The root mean square of the prediction (RMSEP) of when adding each LV to the model.

(D) Experimental vs. predicted scatter plots for the values used for calibration (left) and those used for leave-one-out cross-validation (right). Error bars represent standard error of the mean (SEM). Computed R^2, Q^2, and Pearson correlation are also shown.

(E) Treatment scores from the signal tensor visualized on a scatter plot of latent variable 2 vs. latent variable 1.

(F) Response weights from the model plotted on a scatter plot of latent variable 2 vs. latent variable 1. Solid gray line indicates the mean (μ) of 500 null models, whereas dotted gray lines indicate ±1 standard deviation (σ) from the average of null models (see text for details).

(G) Signal weights from the model plotted on a scatter plot of latent variable 2 vs. latent variable 1. Solid gray lines indicate the mean (μ) of signal weights in the model. Dotted lines indicate one standard deviation (σ) from the mean.

(H) Barplot of variable importance in projection (VIP) scores of signals. Underlining of the signal name indicates a cytoplasmic signal, whereas the absence of underlining indicates a nuclear signal. Blue bars indicate significant senescent signals, red bars indicate significant apoptotic signals, black bars indicate significant proliferation signals, and gray bars indicate non-significant signals as seen in t-PLSR.

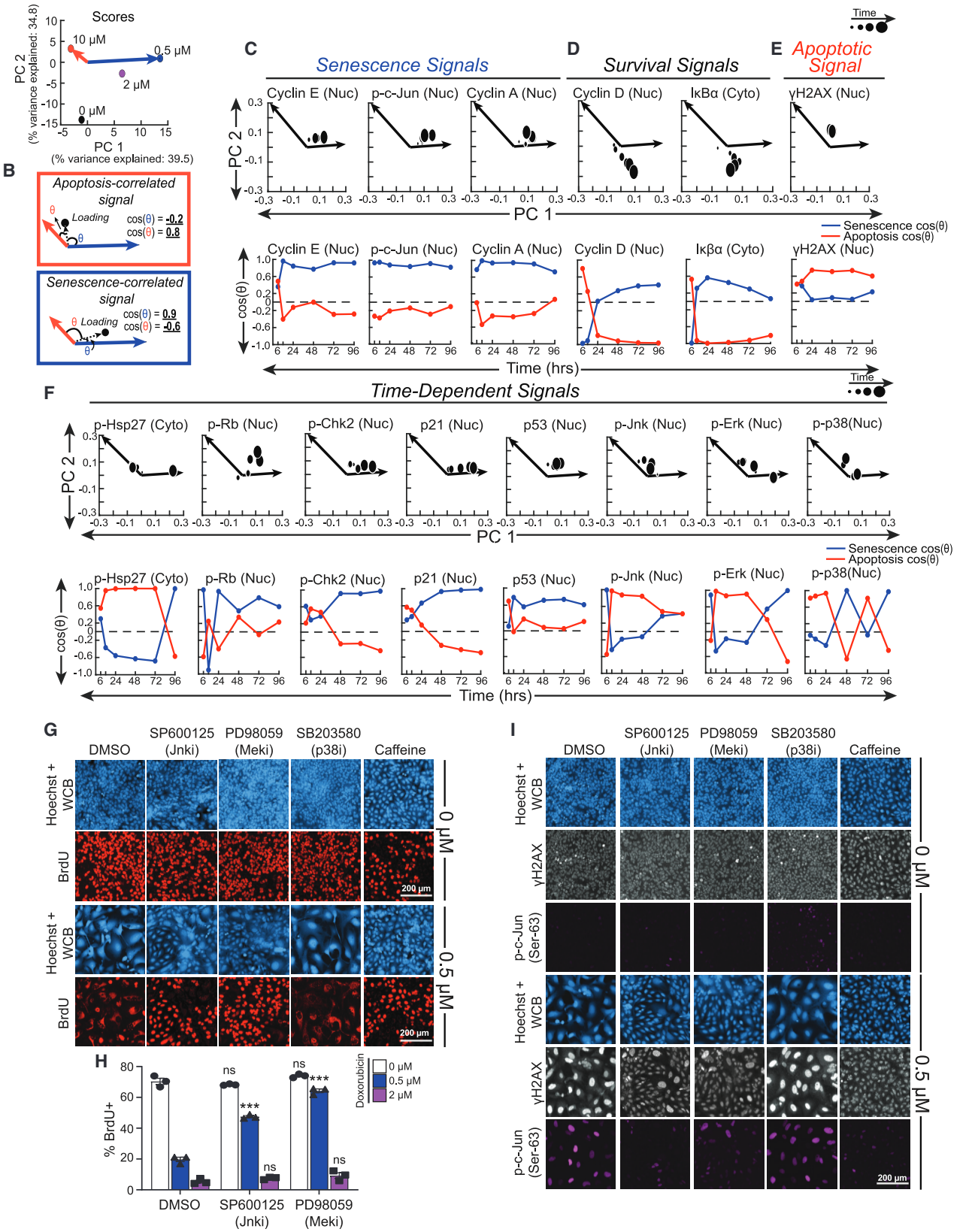

legend on next page)

relationships between signaling pathways and cell fates. Signals contributing strongly to the model were identified by weightings on LV1 or LV2 that were one or more standard deviations above the mean signal cutoff (Figure 4G) and the significance of contributing signals was further assessed using variable importance in projection (VIP) scores (Figure 4H).[58] Both nuclear cyclin D and cytoplasmic IκB levels were strongly negatively weighted on LV1 with high VIP scores, thus significantly correlating with cell proliferation (Figure 4G). These two elements in the t-PLSR model are in strong agreement with our interpretation of the LV1 axis, since the G1 cyclin, cyclin D, is well-established as a key regulator of cell proliferation,[59,60] although activation and nuclear translocation of NF-κB, which is inhibited by IκB , have been shown to be elevated in senescent cells.[61–63]

Nuclear γH2AX and phospho-Hsp27, together with the levels of activated p38MAPK, JNK, and Erk in the nucleus, projected positively along LV2, correlating with apoptosis (Figure 4G). These findings further support our biological interpretation of the LV2 axes, since γH2AX intensity reflects the extent of DNA damage, and we and others have shown previously that p38MAPK (along with its downstream targets MK2 and Hsp27), Erk, and JNK have complex, context-dependent roles in cellular stress and DDRs,[34,35,37,64–66] with JNK commonly associated with certain types of stress-associated cell death.[67–70] Furthermore, Hsp27 is a molecular chaperone that is a direct substrate of the p38MAPK-MK2 signaling axis activated downstream of DNA damage, which we and others have previously shown to be phosphorylated after DNA damage.[37,71,72] Thus, the projection of phospho-Hsp27 along LV2 further confirms the strong correlation between the p38MAPK pathway and apoptosis in our system.

Finally, nuclear levels of phospho-Chk2, phospho-Rb, cyclin E, cyclin A, p53, and $p21^{Waf1}$ projected strongly along LV1 (Figure 4G), had some of the highest VIP scores among the positive LV1 signal weights (Figure 4H), and closely correlated with cell senescence. Chk2 has been previously associated as a driver of RS.[73,74] p53, a critical regulator of senescence,[75–77] transcriptionally upregulates expression of $p21^{Waf1}$,[78] which is both a canonical marker of senescence and the CDKI likely contributing to cell-cycle arrest in this system.[79–81] This rationalizes the observed high levels of cyclins E and A, in these 4N G2-arrested p21+ cells (Figures 4F and 4G). Phosphorylation of Rb releases E2F transcription factors to facilitate the progression of 2N G1 cells through S phase,[82–85] consistent with the observed accumulation of senescent cells in a 4N G2-arrested state. The most unanticipated finding, however, was the very strong contribution of nuclear phospho-c-Jun to LV1, where it emerged as the strongest correlate with cell senescence based on the projection of its weight on LV1 and its VIP score, ranking as a more important contributor than $p21^{Waf1}$ (Figures 4G and 4H). c-Jun is a major component of the AP-1 transcription factor family and has been well-characterized as a modulator of cell proliferation, cell-cycle progression, and cell death in a context-dependent manner.[86–89] However, its potential role in modulating DNA damage-induced cell senescence has not been explored.

Phosphorylation and nuclear translocation of c-Jun are known to be mediated by JNK, Erk, and p38MAPK,[90–93] suggesting that the time-dependent activity of one or more of these kinases might be involved in regulating DDIS. Because time weights in t-PLSR reflect the aggregate measurements contributed by all signals or responses at one particular point in time and are not amenable for dissecting the specific time-dependent contributions of any individual molecular signal, we instead applied principal component analysis (PCA) to the signaling data to parse how individual signals co-varied and separated by time point. Two PCs captured greater than 70% of the variance in the signaling data. When each of the doxorubicin treatments was scored along these signal-generated PCs, the senescence-inducing doses (0.5 and 2 μM) mainly segregated positively along PC1 with respect to the origin in PC space (Figure 5A, blue vector), whereas the apoptotic dose (10 μM) separated negatively along PC1 and positively along PC2 (Figure 5A, red vector).

PCA loadings of each of the molecular signals previously determined to be statistically significant contributors to LV1 and 2 by t-PLSR were then examined for their contributions to PC1 and PC2. In order to quantitatively evaluate the extent of correlation of each PCA loading with either senescence or apoptosis, we defined senescence and apoptosis axes in PC space using the 0.5 and 10 μM treatment scores, respectively, since these were the most homogenous senescence and apoptosis-inducing doses (Figure 5A). We then vectorized each PCA loading with respect to the PC1 and PC2 origins and calculated the projection of this loading vector with these senescence or apoptosis axes (Figure 5B).

Senescence and apoptosis projections were calculated for each PCA loading and plotted over time to gain insight into time-dependent associations. This revealed that several signals

Figure 5. Kinases upstream of c-Jun JNK and Erk regulate senescence after DNA damage

(A) PCA scores of doxorubicin treatments plotted on a scatterplot of principal component 2 (PC2) vs. principal component 1 (PC1).

(B) Schematic of PCA loading vector (dotted arrow) in relation to apoptosis axis (red arrow) and senescence axis (blue arrow), the angles between the loading vector and senescence axis (blue theta), and the loading vector and apoptosis axis (red theta). The cosine of the blue theta is the projection along the senescence axis, and the cosine of red theta is the projection along the apoptosis axis.

(C–F) PCA loadings and projections of significant (C) senescent signals, (D) survival signals, (E) apoptotic signals, and (F) time-dependent signals. Larger PCA loadings correspond to later time points. Apoptosis projections (red curves) and senescence projections (blue curves) were plotted over time for each signal.

(G) Representative immunofluorescence of cells treated with doxorubicin and either DMSO, 10 μM SP600125, 10 μM PD98059, 10 μM SB203580, or 5 mM caffeine. Doxorubicin was left on for 4 h and then washed off, while inhibitors were left on the entire duration of the 6-day experiment. Cell morphology was visualized with Hoechst staining and Whole Cell Blue (WCB) dye, and proliferative cells were visualized with nuclear BrdU antibody staining. Images representative of 150–5,000 individual cells per biological replicate, depending on the condition.

(H) Quantification of the percent of cells with that are positive for nuclear BrdU in the DMSO, 10 μM SP600125, and 10 μM PD98059 co-treatment conditions 6 days after doxorubicin treatment. Bars represent mean of three biological replicates, error bars represent SEM. ***$p < 0.001$, ns: $p > 0.05$ with a two-way ANOVA and post hoc Dunnett's test vs. DMSO inhibitor control at the same dose of doxorubicin.

(I) Representative immunofluorescence for p-c-Jun (Ser63) and γH2AX of cells treated in the same conditions as in (E). Images representative of 150–5,000 individual cells per biological replicate, depending on the condition.

identified by t-PLSR as significantly correlated with senescence or apoptotic cell fates mapped onto the corresponding PCA senescence and apoptosis axes across the majority of sampled time points. Levels of phospho-c-Jun, and cyclins A and E, for example, projected strongly along the PCA senescence axis at nearly all time points (Figure 5C, lower), further confirming their correlation with senescence as revealed in the t-PLSR analysis (Figure 4G). Cyclin D and IκB , which were correlated with survival in the t-PLSR analysis, had the most negative projections along the apoptosis axis of any other signal at intermediate and late time points, further suggesting that these signals are highly anti-correlated with apoptosis (Figure 5D, lower). By contrast, γH2AX had larger projections along the apoptosis axis than projections along the senescence axis at most time points, consistent with its correlation with apoptosis as seen in t-PLSR (Figure 5E, lower).

The remaining signals that were significantly weighted on LV1 and LV2 in t-PLSR exhibited complex, time-dependent correlations with senescence and apoptosis. Signals such as phospho-Chk2 and p21 had positive projections along the apoptosis axis at early times but negative projections along the apoptosis axis and strong positive projections along the senescence axis at the middle and late time points, whereas phospho-Hsp27 and phospho-Rb had one and two time points, respectively, where the senescence or apoptosis projections dramatically crossed over. p53 projected positively along both the apoptosis and senescence axes in PC space, with a stronger apparent projection toward senescence (Figure 5F). This fits with the trends seen in the IF data, which show that although there is lesser p53 accumulation with the 10 μM dose in comparison to the 0.5 and 2 μM doses, the p53 levels at this dose are still ~2-fold greater than the vehicle condition (Figures 3C and S2). This correlation with both senescence and apoptosis is consistent with the known role of p53 in both senescence and apoptosis.[94–96]

Both JNK and Erk MAPKs showed strong projections along the senescence axis at very early times. This was subsequently followed by strong projections for both MAPKs along the apoptosis axis at intermediate times and increased projection along the senescence axis again at late times (Figure 5F, lower). By contrast, p38MAPK exhibited highly oscillatory apoptosis and senescence axis projections that continued to cross over at the middle and late time points. Taken together, these results suggest nuanced, time-dependent roles for the majority of signals significantly weighted on LV1 and LV2 in t-PLSR, particularly the p38MAPK, JNK, and Erk MAPKs in DDIS.

Early but not late JNK and Erk signaling controls senescence after low-dose doxorubicin treatment

The strong correlation of phospho-c-Jun levels with cell senescence observed after doxorubicin treatment (Figures 4G and 5C), together with the potential time-dependent roles of JNK, Erk, and p38MAPK in senescence, as revealed by the PCA analysis led us to experimentally investigate whether p38MAPK, Erk, and JNK directly contribute to regulating DDIS through phosphorylation of c-Jun. U2OS cells were treated with doxorubicin, and the kinase activities of p38, Mek1, and JNK were blocked with the specific small molecule inhibitors SB203580, PD98059, and SP600125, respectively, with kinase inhibition validated by western blotting (Figures S5A–S5G). In these experiments, U2OS cells were treated with a 4-h doxorubicin pulse and given fresh media on days 1 and 3 post-damage. Kinase inhibitors were applied simultaneously with doxorubicin and maintained throughout the 6-day duration of the experiment. Proliferation and senescence were evaluated by measuring the extent of BrdU incorporation over 24 h starting 5 days after doxorubicin treatment. As observed previously, DMSO-treated U2OS cells showed strong BrdU uptake in spite of reaching high cell densities, whereas 0.5 μM doxorubicin treatment alone drives DDIS as indicated by morphological changes and the lack of BrdU incorporation into nuclear DNA (Figure 5G). Inhibition of JNK using SP600125 markedly abrogated this DDIS response. By contrast, following treatment with 2 μM doxorubicin, the DDIS could not be reversed by SP600125 (Figures 5G and 5H). Blocking Erk signaling by inhibiting Mek1 similarly abrogated the senescence response to 0.5 μM doxorubicin, but, as was the case for JNK inhibition, PD98059 did not abrogate 2 μM doxorubicin-induced senescence (Figures 5G and 5H). These pharmacologic perturbations suggested a role for Erk and JNK in DDIS triggered by low-dose doxorubicin.

To simultaneously visualize DNA damage signaling and signaling through c-Jun on a cell-by-cell basis, cells were co-stained for the γH2AX and p-c-Jun (Ser-63) (Figure 5I). DMSO-treated cells exhibited a uniform, small size, and low levels of γH2AX and phospho-c-Jun, whereas treatment with 0.5 μM doxorubicin induces a population of large, flat senescent cells that stained positively for γH2AX and phospho-c-Jun (Figure 5I). Although some heterogeneity in the extent of phospho-c-Jun staining was noted in the senescent cells, treatment with either SP600125 or PD98059, which abrogated DDIS, markedly reduced γH2AX staining and nearly completely eliminated nuclear phospho-c-Jun staining.

It should be noted that the abrogation of 0.5 μM doxorubicin-induced senescence by either SP600125 or PD98059 was not complete. The sub-population of cells that escaped senescence and proliferated after exposure to 0.5 μM doxorubicin upon treatment with either SP600125 or PD98059 were characterized by "normal" U2OS morphology, incorporation of BrdU, and low levels of both γH2AX and phospho-c-Jun (Figures 5G and 5I). By contrast, the residual sub-population of senescent cells that persisted demonstrated an enlarged fried egg cellular morphology, lack of nuclear BrdU incorporation, and increased levels of both γH2AX and phospho-c-Jun, further supporting the correlation of phospho-c-Jun with the induction of DDIS. Inhibition of p38MAPK with SB203580 failed to suppress DDIS, nuclear γH2AX intensity, or phospho-c-Jun staining, whereas the addition of 5 mM caffeine, which served as a positive control, abrogated all three, as would be expected from its ability to simultaneously inhibit all three of the DDR kinases ATM (ataxia telangiectasia mutated), ATR, and DNA-PK (Figures 5G and 5I). Taken together, we interpret these data as evidence that signaling through JNK and Erk, but not p38MAPK, plays a causal role in the induction of DDIS, likely through the phosphorylation of c-Jun (see below).

The DNA damage-induced senescent state, which is characterized by morphological changes, elevated cyclins E and A, stable G2 arrest, and high levels of p21 emerges 3–4 days after DNA damage (Figures 1, 2, and 3). This multi-day time course

between DNA damage and the emergence of the senescence state suggests a series of dynamic temporally regulated signaling events and regulatory transitions that coordinate progression to senescence. Notably, in our PCA analysis, both JNK and Erk had strong senescence-associated signals 6 h after doxorubicin treatment, suggesting possible early pro-senescence roles for JNK and Erk activity (Figure 5F). To experimentally investigate at what point after DNA damage JNK and Erk signaling control the senescence cell-fate decision, small molecule inhibitors were added either during the first 12 h after the onset of doxorubicin-induced DNA damage or added 12 h after doxorubicin treatment and removed at 24 h (Figure 6A). As shown in Figures 6B and 6C, addition of the JNK inhibitor SP600125, the Mek1 inhibitor PD98059, or caffeine, during the first 12 h after DNA damage significantly reduced the fraction of cells that underwent DDIS in response to the 0.5 μM doxorubicin treatment, with a smaller but still significant inhibition of DDIS in response to the 2 μM treatment as well. The p38MAPK inhibitor SB203580 did not reverse the DDIS phenotype, consistent with the prior results (Figure 5G). By contrast, if added 12 h after genotoxic stress, the JNK and Mek inhibitors and caffeine were unable to abrogate the DDIS in U2OS cells (Figures 6D and 6E). Taken together, these observations suggest that JNK, Erk, and DNA damage signaling—but not p38 signaling—and are required within the first 12 h after DNA damage to initiate DDIS after low-dose doxorubicin treatment.

To examine whether the roles of JNK and Erk signaling in driving DDIS were unique to U2OS cells, similar studies were performed in NCI-H1299 non-small-cell lung cancer cells, a tumor type that is commonly treated with doxorubicin in combination with other cytotoxic drugs.[97–99] Treatment with 2 μM of doxorubicin resulted in cells with enlarged nuclei and cytoplasm (i.e., fried egg appearance) that failed to incorporate nuclear BrdU (Figures 6F and 6G) and exhibit high levels of the CDKIs p21 and p27 (Figure S6A). Addition of SP600125, PD98059, or caffeine during the first 12 h after doxorubicin treatment resulted in a decrease in cells that underwent DDIS, indicating that JNK, Erk, and DDR inhibition early after damage can reverse the DDIS in this cell type (Figures 6F and 6G), recapitulating the results obtained in U2OS cells. Similar to what was observed in U2OS cells, addition of JNK or Mek1 inhibitors, or treatment with caffeine, was unable to abrogate DDIS in NCI-H1299 cells if these were added later than 12 h after doxorubicin treatment (Figures 6H and 6I). Similar results were seen in OVCAR-8 high-grade serous ovarian cancer cells and HUVEC cells, which are non-cancerous primary endothelial cells (Figures S6B–S6J). Together, these data indicate that in multiple cell lines cells, JNK and Erk signaling contribute to the early information processing that results in DDIS, and this commitment is made within 12 h after doxorubicin treatment.

Late JNK and Erk activity contributes to the SASP

Phospho-JNK and phospho-Erk levels are elevated at early time points, and the activity of these kinases influences the senescence/proliferation fate decision (Figures 5 and 6A–6I). However, as noted previously, the projections for JNK and Erk along the senescence axis also become positive at late time points in our PCA analysis (Figure 5F), raising the question of whether there may be another senescence-associated function for these signaling pathways at late times. Since senescent cells are known to secrete pro-inflammatory cytokines, particularly IL-6 and IL-8, in response to oncogenic stress or DNA damage,[28,30,31,100] and the JNK and Erk pathways are known to regulate cytokine secretion and mediate cytokine signaling in response to other non-DNA damage stimuli,[101,102] we hypothesized that the late phase JNK and Erk signaling after genotoxic stress might contribute to regulating the DDIS SASP.

To examine this, U2OS cells were treated with senescence-inducing doses of doxorubicin, and the levels of IL-6 and IL-8 were assayed in the media at 2, 4, and 6 days after treatment. As shown in Figures 6J and 6K, both 0.5 and 2 μM doxorubicin treatment induced IL-6 and IL-8 secretion that became significantly elevated by 6 days after treatment. Cells treated with 0.5 μM doxorubicin secreted more IL-6 and IL-8 than cells treated with 2 μM doxorubicin, and the kinetics of cytokine release came after the senescence-associated morphology change. Addition of JNK or Mek1 inhibitors was therefore performed 72 h after DNA damage to allow for the initiation of senescence, but prior to the detection of SASP-associated cytokines (Figure 6L). As shown in Figures 6M and 6N, addition of either the JNK inhibitor SP600125 or the Mek1 inhibitor PD98059 reduced the senescence-associated secretion of IL-6 and IL-8. Together with the data in panels 6A–I, these data indicate that JNK and Erk signaling regulate two different properties of cells undergoing DDIS on two distinct timescales, with early signaling implicated in the senescence decision and late signaling involved in the senescence-associated cytokine secretory response.

JNK and Erk signal through AP-1 to drive cellular senescence after doxorubicin-induced DNA damage

Based on the findings in U2OS cells using t-PLSR and PCA analyses, we initially hypothesized that JNK, Erk, and p38MAPK acted through the phosphorylation of c-Jun to drive DDIS and subsequently demonstrated through inhibition experiments that JNK and Erk activities, but not p38MAPK, were critical for the decision between senescence and proliferation within the first 12 h after low-dose doxorubicin treatment. To demonstrate that c-Jun phosphorylation was directly regulated by these kinases during this early time frame, western blotting and IF assays for phospho-c-Jun were performed at 6 and 12 h following treatment of U2OS cells with 0.5 μM doxorubicin in the presence or absence of JNK or Mek1 inhibitors (Figures S5A, S5B, and S7). SP600125 caused a marked decrease in the levels of phospho-c-Jun after DNA damage in both assays, whereas PD98059 not only caused a more moderate but also statistically significant reduction in c-Jun phosphorylation.

Next, to examine whether inhibition of JNK or Mek1 activity in the presence of DNA damage controls the downstream transcriptional activity of c-Jun, we used an AP-1 mCherry-based transcriptional reporter containing three canonical AP-1 motifs within a minimal promoter upstream of mCherry. U2OS cells stably transfected with the AP-1 reporter were treated with DMSO or 0.5 μM doxorubicin for 4 h, in the presence or absence of SP600125 or PD98059, and mCherry expression quantified by flow cytometry. As shown in Figure 7A, doxorubicin treatment induced a ~3-fold-increase in mCherry expression, similar to that observed in the phorbol 12-myristate 13-acetate (PMA)-treated positive control. Both the JNK inhibitor SP600125 and the Mek1 inhibitor PD98059

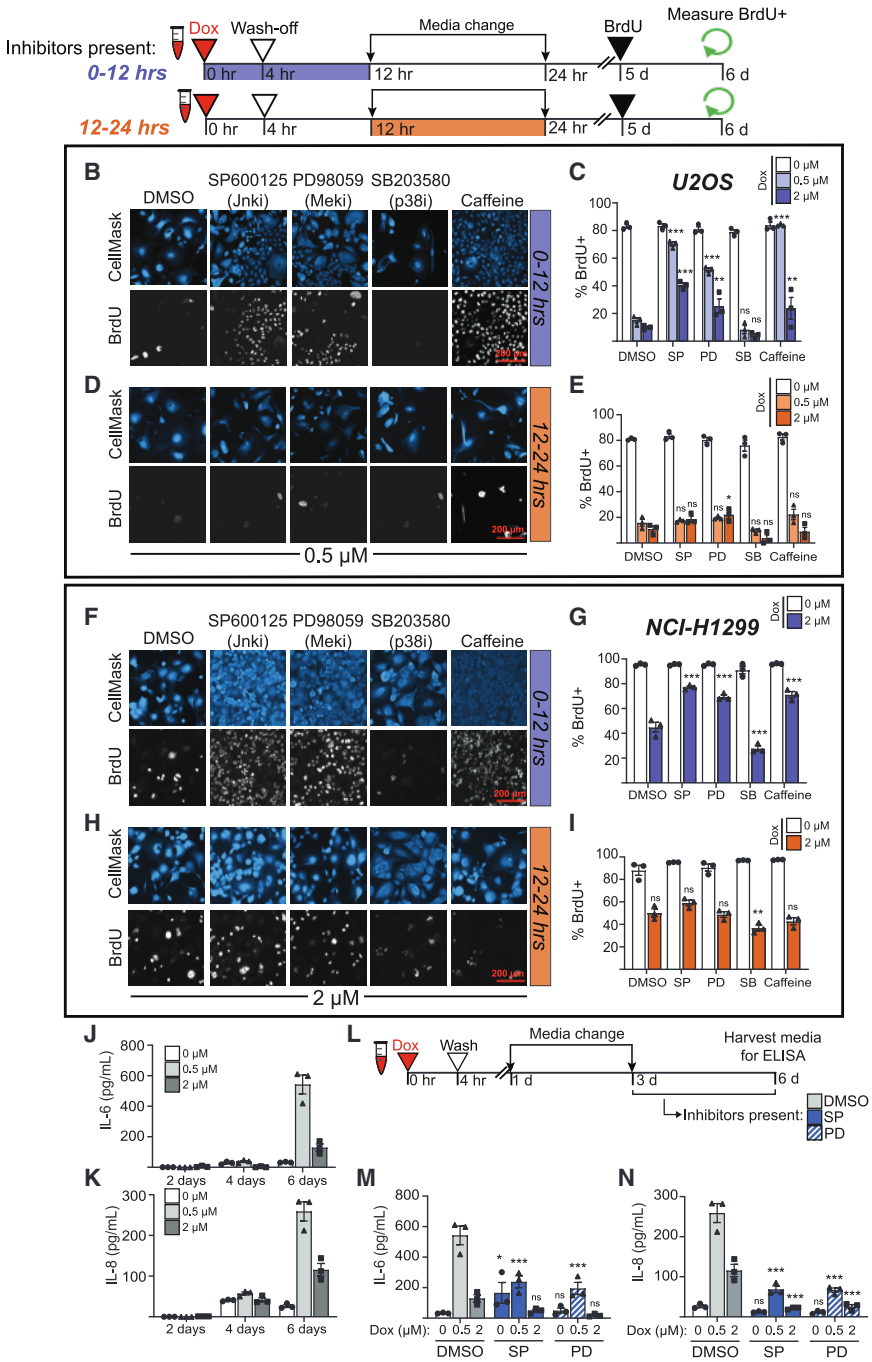

Figure 6. JNK and Erk signaling in the first 12 h after DNA damage controls the senescence-proliferation decision whereas late JNK and Erk signaling controls the SASP

(A) Schematic of experimental workflow for U2OS and NCI-H1299 cells. (Icons created with BioRender.com).

(B) Representative immunofluorescence (IF) of BrdU incorporation into DNA in U2OS cells treated with inhibitors (10 μM for SP600125, PD98059, and SB203580 drugs, and 5 mM of caffeine) for 0–12 h and co-stained with HCS CellMask Blue. Images representative of 650–30,000 individual cells per biological replicate, depending on the condition.

(C) Quantification of the percent of nuclear BrdU+ in U2OS cells after the 0–12 h inhibitor condition.

(D) Representative IF of BrdU incorporation into DNA in U2OS cells treated with inhibitors for 12–24 h and co-stained with HCS CellMask Blue. Images representative of 650–30,000 individual cells per biological replicate, depending on the condition.

(E) Quantification of the percent of nuclear BrdU+ in U2OS cells after the 12–24 h inhibitor condition.

(F) Representative IF of BrdU incorporation into DNA in NCI-H1299 cells treated with inhibitors (10 μM for SP600125, PD98059, and SB203580 drugs, and 1 mM of caffeine) for 0–12 h and co-stained with HCS CellMask Blue. Images representative of 1,500–15,000 individual cells per biological replicate, depending on the condition.

(G) Quantification of the percent of nuclear BrdU+ in NCI-H1299 cells after the 0–12 h inhibitor condition.

(H) Representative IF of BrdU incorporation into DNA in NCI-H1299 cells treated with inhibitors for 12–24 h and co-stained with HCS CellMask Blue. Images representative of 1,500–15,000 individual cells per biological replicate, depending on the condition.

(I) Quantification of the percent of nuclear BrdU+ in NCI-H1299 cells after the 12–24 h inhibitor condition.

(J and K) (J) IL-6 and (K) IL-8 levels in culture media of U2OS cells 2, 4, and 6 days after doxorubicin treatment as measured by ELISA.

(L) Schematic of experimental workflow for ELISA-based co-inhibitor experiment.

(M and N) (M) IL-6 and (N) IL-8 levels as measured by ELISA in U2OS tissue culture media 6 days after doxorubicin addition. DMSO inhibitor control bars in (M) and (N) are the same values as seen in (J) and (K) 6 days after doxorubicin. For all bar graphs in this figure, bars represent mean ± SEM of three biological replicates. ***$p < 0.001$, **$p < 0.01$ *$p < 0.05$, ns: $p > 0.05$ with a two-way ANOVA and post hoc Dunnett's test for (C), (E), (G), (I), (M), and (N). All comparisons were vs. the DMSO treatment at the same dose of doxorubicin.

suppressed AP-1 transcriptional upregulation following DNA damage, mirroring the extent of suppression of c-Jun phosphorylation seen using these inhibitors by both immunoblotting and IF (Figures 7A, S5A, S5B, and S7). To further validate that c-Jun is the relevant AP-1 family member in U2OS cells, the cells were transfected using a dominant negative c-Jun construct lacking the transactivation domain and sites of JNK and Erk phosphorylation, hereafter referred to as JunDN.[103] Expression of JunDN reduced AP-1-driven transcription in both the absence and presence of doxorubicin treatment but notably reduced AP-1 transcription following doxorubicin treatment to the same level as that seen in untreated control cells (Figure 7A).

To directly test whether c-Jun controls the early cell-fate decision after DNA damage, U2OS cells were transfected with two independent siRNAs targeting c-Jun, resulting in a good knockdown of c-Jun at the protein level (Figure 7D). When

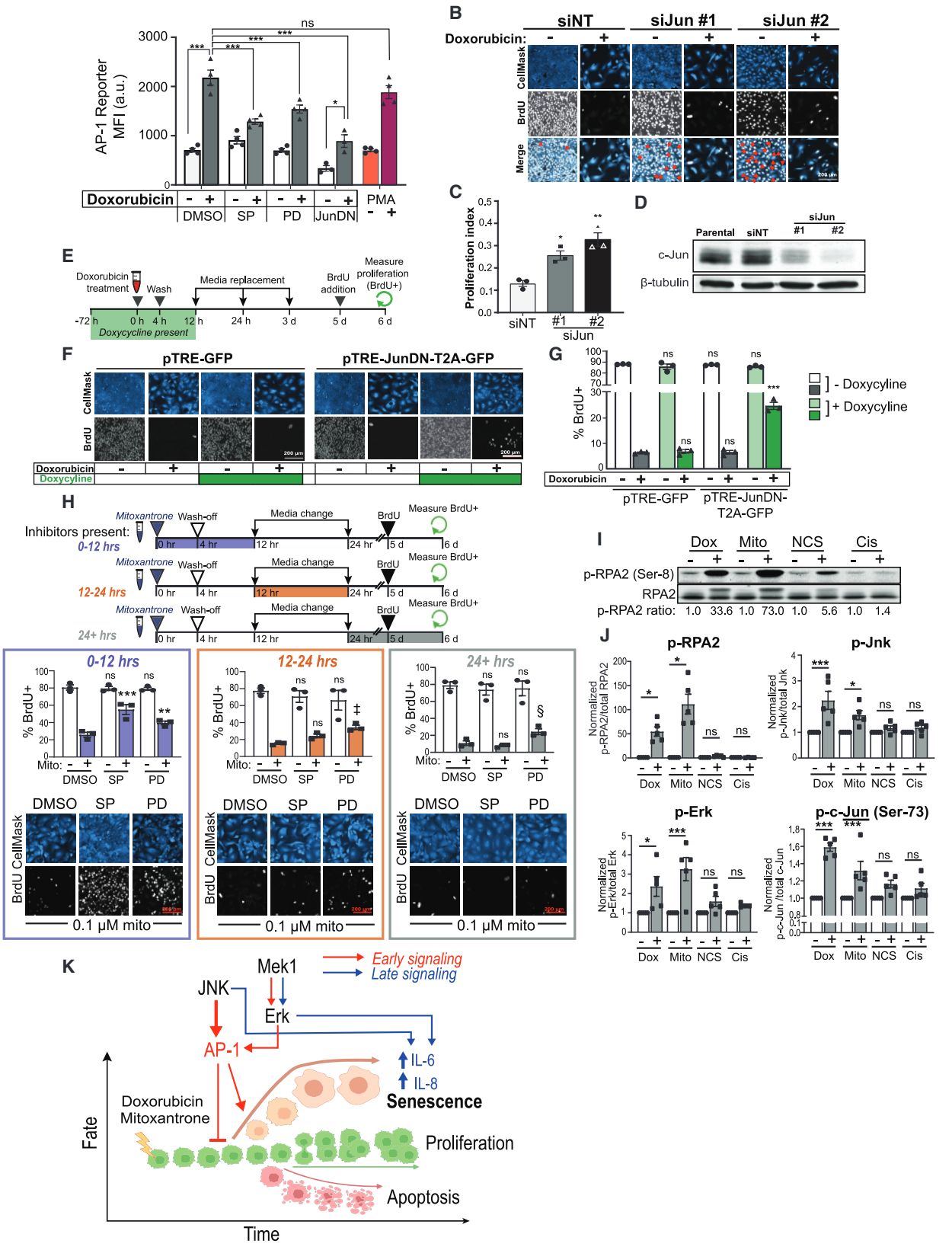

legend on next page)

proliferation was measured by BrdU incorporation 6 days after a 4-h pulse of either vehicle or 0.5 μM doxorubicin, a significant increase in the percentage of BrdU-positive cells was observed that correlated with the extent of knockdown (Figures 7B and C). However, even in the absence of doxorubicin treatment, c-Jun knockdown resulted in a sub-population of cells that were BrdU negative (Figure 7B, merge), likely as a consequence of prolonged doubling times that exceeded the 24-h BrdU pulse. To mitigate the impact of continual c-Jun suppression on basal cell proliferation, we next generated U2OS cells stably expressing a tetracycline-inducible (tet-on) construct containing JunDN linked with a T2A cleavable linker to GFP (JunDN-T2A-GFP). Expression of JunDN was induced by doxycycline for 3 days prior to a 4-h drug pulse of 0.5 μM doxorubicin, and the cells were then maintained in doxycycline for 12 h after doxorubicin treatment. The media was then changed to doxycycline-free media, which was replaced with fresh doxycycline-free media 1 and 3 days after doxorubicin treatment (Figure 7E). As shown in Figure 7F, control cells expressing a tet-on GFP-only construct exhibited no increase in BrdU-positive cells 6 days after DNA damage, regardless of doxycycline treatment. By contrast, cells expressing the JunDN-T2A-GFP construct demonstrated a significant increase in the percentage of BrdU-positive cells after DNA damage only in the presence of doxycycline (Figures 7F and 7G). These data, combined with the c-Jun knockdown results in panels 7B–D, confirm that AP-1 has a direct role in the senescence cell-fate decision after low-dose doxorubicin treatment, whereas the AP-1 reporter results, coupled with the phospho-c-Jun measurements in the presence or absence of inhibitors, indicate that JNK and Erk are the upstream kinases activating AP-1 in this context.

Curiously, the levels of phospho-JNK and Erk were also elevated in response to the 2 and 10 μM doxorubicin doses at all measured time points; however, the levels of phospho-c-Jun were moderately reduced at the 2 μM dose and strongly reduced at the 10 μM dose in comparison to the 0.5 μM dose (Figure 3C). At the suggestion of a reviewer, we therefore measured the levels of total c-Jun in U2OS cells by western blotting at early time points after treatment with each drug dose (Figures S5H and S5I). Relative to the 0.5 μM dose, the levels of total c-Jun progressively decreased at higher doxorubicin doses, becoming statistically significantly reduced by 6 h, which is well within the time frame of when c-Jun determines the senescence-fate decision (Figures 6, 7F, and 7G). These reduced levels of total c-Jun can at least partially rationalize why high JNK and Erk activity fails to induce the same extent of cell senescence at higher drug doses than that seen with the 0.5 μM dose.

JNK and Erk signaling drives cell senescence in response to a subset of DNA-damaging agents

To investigate whether JNK and Erk signaling in response to doxorubicin is a conserved general mechanism for initiating DDIS in response to all types of genotoxic stress, we next examined mitoxantrone, a topoisomerase II inhibitor that is structurally distinct from doxorubicin; neocarzinostatin (NCS), a radiomimetic enediyne agent that directly cleaves DNA to form double-strand breaks; and cisplatin, a common DNA crosslinking agent. Doses of each drug were selected that induced U2OS cell senescence based on cell morphology and lack of BrdU uptake

Figure 7. c-Jun together with JNK and Erk directly controls the senescence-proliferation switch after treatment with replication stress-inducing DNA-damaging agents

(A) Mean-fluorescence intensity (MFI) in the mCherry channel as measured by flow cytometry in U2OS cells expressing AP-1-mCherry reporter 24 h after doxorubicin addition or continuous treatment with 100 nM (PMA). Bars represent mean ± SEM of biological replicates n = 4 (DMSO, SP, PD, and PMA) or n = 3 (JunDN). ***p < 0.001, *p < 0.05, ns: p > 0.05 with a two-way ANOVA and post hoc Bonferroni's multiple comparisons test.

(B) Representative immunofluorescence images of U2OS stained with anti-BrdU and HCS CellMask Blue 6 days after either 0.5 μM doxorubicin treatment (+) or DMSO (−). Red arrows indicate BrdU negative cells.

(C) Quantified proliferation index, calculated as the percentage of BrdU-positive cells after treatment with 0.5 μM doxorubicin divided by the percentage of BrdU-positive cells after vehicle treatment (DMSO) for each respective siRNA. Bars represent the mean ± SEM of three biological replicates. *: p < 0.05, **: p < 0.01 with a one-way ANOVA and post-hoc Dunnett's test vs. siNT.

(D) Representative immunoblot for c-Jun and β-tubulin 48 h post-transfection. Images are representative of 1,800–33,000 individual cells per biological replicate, depending on the condition.

(E) Schematic of experimental workflow for inducible JunDN over-expression experiment. (Icons created in BioRender.com.)

(F) Representative immunofluorescence images of U2OS stably transfected with either the TRE-GFP or the TRE-JunDN-T2A-GFP stained with anti-BrdU and HCS CellMask Blue 6 days after doxorubicin treatment. Images are representative of 3,300–33,000 individual cells per biological replicate, depending on the condition.

(G) Quantification of nuclear BrdU incorporation in TRE-GFP and TRE-JunDN-T2A-GFP cells 6 days after doxorubicin treatment. Bars represent the mean ± SEM of biological replicates (n = 3). ***p < 0.001, ns: p > 0.05 with a two-way ANOVA and post hoc Dunnett's test vs. the TRE-GFP condition with no doxycycline at the same dose of doxorubicin.

(H) Workflow of timed JNK and Mek1 inhibitor experiments, similar to Figures 6A–6I. U2OS cells were treated with 0.1 μM mitoxantrone or vehicle control, in the presence or absence of SP600125, PD98059, or DMSO for the indicated times. Cells were stained with anti-BrdU and HCS CellMask Blue 6 days after mitoxantrone treatment, and nuclear BrdU positivity quantified. Bars represent the mean ± SEM of three biological replicates. ***p < 0.001, **p < 0.01, ‡: ns, p = 0.073, §: ns, p = 0.141, ns: p > 0.05 using two-way ANOVA and post hoc Dunnett's test vs. DMSO treatment at the same dose of mitoxantrone. CellMask blue was visualized with gamma = 0.6 to better visualize the cytoplasmic compartment. Images are representative of 3,500–25,000 individual cells per biological replicate, depending on the condition.

(I) Western blot of phospho-RPA2 (Ser-8) and total RPA2 in U2OS 6 h after addition of doxorubicin (0.5 μM), mitoxantrone (0.1 μM), neocarzinostatin (NCS, 0.25 μg/mL), or cisplatin (20 μM) and their respective vehicle controls (−).

(J) Quantification of western blots for phospho- and total RPA2, JNK, Erk, and phospho-c-Jun (Ser-73) 6 h after the addition of doxorubicin (0.5 μM), mitoxantrone (0.1 μM), NCS (0.25 μg/mL), or cisplatin (20 μM) and their respective vehicle controls (−). Bars represent the mean ± SEM of biological replicates (n = 3 or 4). ***p < 0.001, **p < 0.01, *p < 0.05 using an unpaired, two-way t test vs. vehicle with Bonferroni correction. See Figure S8B for representative western blots.

(K) Proposed mechanism for JNK and Erk signaling in DDIS after doxorubicin or mitoxantrone treatment. (Created with BioRender.com.)

(Figures 7H and S8A). Cell senescence induced by mitoxantrone was reversed upon treatment with JNK and Mek1 inhibitors, particularly if added within the first 12 h, similar to that observed with doxorubicin (Figure 7H). By contrast, neither the senescence induced by NCS nor cisplatin could be reversed by inhibiting JNK or Erk activity (Figure S8A).

We noted that topoisomerase II inhibitors, such as doxorubicin and mitoxantrone, are particularly strong inducers of replication stress.[104–107] We therefore examined whether the amount of replication stress that occurred at early times after treatment differed between drugs that responded to JNK and Mek1 inhibitors relative to those that did not. Levels of replication stress were analyzed using phospho-RPA2, a marker of single-stranded DNA exposed at stalled replication forks,[108–110] by western blotting after each of these four drug treatments. At 6 h after the addition of doxorubicin and mitoxantrone, we observed a 50- and 100-fold increase in phospho-RPA2, respectively, compared with vehicle controls, whereas NCS and cisplatin exhibited much smaller average fold-changes of 3.5 and 1.4, respectively (Figures 7I and 7J). To further delineate features that distinguished drugs whose senescence was reduced by JNK and Mek1 inhibition compared with drugs whose senescence did not, the levels of total and phospho-JNK, Erk, and c-Jun were measured by western blot 6 h after treatment. As seen in Figure 7J, both doxorubicin and mitoxantrone treatment significantly increased phospho-JNK, Erk, and c-Jun levels relative to vehicle controls, whereas NCS and cisplatin did not (Figures 7J and S8B). Taken together, these results suggest that the induction of senescence after DNA damage is heavily influenced by signaling through the JNK and Erk pathways particularly in response to treatment with genotoxic drugs that induce early replication stress.

DISCUSSION

In this manuscript, we interrogated canonical and non-canonical DNA damage signaling pathways for their influence on cell-fate decisions in response to different levels of DNA damage. Since activation of a common set of DDR-activated signaling molecules, including among others ATM, Chk2, H2AX, Nbs1, 53BP1, p53, and p21[2,111–114] results in diverse phenotypic outcomes, we hypothesized that crosstalk from additional signaling pathways likely influenced the cell-fate decision process. We were particularly interested in examining the signaling responses at the single-cell level under conditions where sub-populations of cells underwent different cell fates using quantitative microscopy, IF, and flow cytometry, combined with computational modeling. The resulting compendium of data was used to construct a t-PLSR model, using fewer parameters to predict the responses that are required for a conventional unfolded PLSR models.[39,50] Our results demonstrate that a relatively small number of treatments was sufficient to construct a model that was robust and provided biological insights. Using t-PLSR modeling and PCA analysis paired with subsequent experimental validation, we identified unexpected roles for the MAPKs JNK and Erk in modulating the early fate decision between DDIS and proliferation in the setting of low-dose DNA damage through the common downstream target of c-Jun, as well as a later role for these kinases in controlling the SASP cytokines IL-6 and IL-8 in committed senescent cells.

Our finding of a central role for JNK in enhancing the cell-fate choice of senescence after modest DNA damage was unexpected since JNK is best known to function as a stress-responsive regulator of apoptotic and non-apoptotic cell death. JNK promotes intrinsic apoptotic cell death, both *in vitro* and *in vivo*[68,115,116] through a variety of mechanisms, including direct phosphorylation and activation of pro-apoptotic BH3 proteins,[117,118] inactivation of the central scaffolding molecule 14-3-3,[119,120] and phosphorylation and activation of p53 and/or p73 to increase the transcription of the pro-apoptotic BH3 family member PUMA.[121,122] In addition, novel roles for JNK in promoting necroptosis, pyroptosis, ferroptosis, and autophagic cell death have recently been observed.[123] JNK activity even prevents p53-mediated cell senescence in unperturbed MEFs in culture.[124] Our findings of a specific role for JNK in inducing senescence, rather than preventing senescence or promoting cell death, following modest levels of doxorubicin- or mitoxantrone-induced DNA damage, suggest a very specific context-dependence in which JNK signaling controls the fate choice between senescence, proliferation, and death.

Conversely, the Erk MAPK pathway has typically been associated with the enhancement of cell proliferation and differentiation, rather than senescence induction, through the direct Erk-dependent phosphorylation of a large number of transcription factors, including members of the TCF, ERG, ERF, PEA3, AP-1, and EGR families as well as Runx2 and c-Myc themselves,[125] resulting in their nuclear translocation, enhanced DNA binding, and transcription of immediate early genes and G1 cyclins. In addition, Erk phosphorylation of the stem cell transcription factors Oct4, Klf4, and Klf2 has been shown to decrease their stability and thus lead to loss of pluripotency.[126–128] In the setting of DNA damage, our lab and others have shown previously that Erk contributes to both G1/S arrest and subsequent apoptotic cell death after DNA damage using high doses of doxorubicin or cisplatin.[35,64,129] To our knowledge, a clear role for Erk in contributing to cell senescence following extrinsic DNA damage induced by low-dose cytotoxic chemotherapy has not been reported. Erk activity has, however, been shown to contribute to the induction of senescence in p53 wild-type cells in response to expression of oncogenic Ras and/or Raf.[130–132] Interpretation of our findings in light of the findings from Bartek, Lucas, and colleagues, who showed that oncogene activation results in replication stress and intrinsic DNA damage, suggests that a similar Erk-dependent senescence pathway as that observed following oncogene activation is being activated by genotoxic drugs that induce large amounts of replication stress.[5]

Unexpectedly, we did not detect a quantitatively significant role for the p38MAPK pathway in controlling the senescence decision at early times following low-dose DNA damage, despite the fact that this pathway is known to be activated by many different types of stress, including DNA damage.[133] In response to more extensive DNA damage induced by higher doses of doxorubicin (or cisplatin), p38MAPK, acting through MK2, is known to be required for sustained cell-cycle arrest and cell survival, but this effect results from signaling at late times greater than 12 h and is important only in cells in which p53 activity is at least partially defective.[40,134–136] This delayed temporal activation of the p38MAPK-MK2 pathway following DNA damage[134] rationalizes the lack of effect of p38MAPK inhibition on low dose DDIS onset

and instead indicates roles for this pathway primarily at later times. Consistent with this, a major role for p38MAPK in regulating the SASP has been reported by Campisi and colleagues.[32]

The AP-1 transcription factor in general, and c-Jun, in particular, emerged as key determinants of senescence in our experiments. The AP-1 transcription factor is a hetero- or homo-dimeric complex comprised of members of the Jun, Fos, ATF, and MAF protein families, which plays an important role in oncogenesis and tumor proliferation and is known to be regulated by JNK, Erk, and p38MAPK in a context-specific manner.[137] The major AP-1 family member that emerged from our experimental findings and computational t-PLSR and PC analyses of low-dose DNA damage in U2OS cells was c-Jun, whose phosphorylation and nuclear accumulation correlated with the early cell-fate decision toward senescence. Suppression of c-Jun using siRNA partially reversed the senescence phenotype after DNA damage, and this partial bypass of senescence was further confirmed using inducible expression of a non-phosphorylatable dominant negative form of c-Jun, which suppressed AP-1 activity in the cells.

Two recent papers have implicated the role of AP-1 in OIS. Martinez-Zamudio et al.[138] used a combination of transcriptomic, ATAC-seq, and chromatin immunoprecipitation sequencing (ChIP-seq) data to nominate AP-1 as a pioneering transcription factor that altered chromatin structure and allowed the establishment of a senescence-inducing enhancer landscape following the inducible expression of a Ras^{G12V} mutant oncogene in WI-38 human fibroblasts. siRNA knockdown of c-Jun had a larger effect on the Ras-induced senescence transcriptional program than did knockdown of the non-pioneering transcription factors ETS1 and RelA, not only primarily suppressing transcription of SASP-related genes but also partially re-activating proliferation-associated genes. Those authors did not examine upstream regulatory kinases or demonstrate reversion of a senescence cellular phenotype. Nonetheless, their extensive and comprehensive epigenetic and transcriptional analysis of OIS is in good potential agreement with our findings of an important role for c-Jun in doxorubicin-induced senescence in U2OS cells.

In a separate study, Han et al. used inducible expression of a mutant Ras^{G12V} oncogene in hTERT-immortalized BJ fibroblasts and observed an upregulation of enhancer RNAs that were enriched for the binding motif of AP-1,[139] suggesting an important role for AP-1-driven gene transcription in response to oncogenic stress. They then identified a specific AP-1-driven enhancer region controlling the expression of FOXF1as critical for the onset of OIS. Taken together, these two studies support our findings that JNK and Erk modulate an AP-1-driven program of senescence and suggest strong parallels between OIS and senescence induced by extrinsic DNA-damaging drugs that cause extensive replication stress. Interestingly, Davis and colleagues have shown, using a PTEN inactivation-dependent model of prostate cancer, that genetic elimination of JNK, or its upstream activators MKK4 and 7, results in a marked enhancement of prostate tumor growth by suppressing the senescence response of prostate cells upon PTEN loss.[140] Those findings are in excellent agreement with our proposed model for an important role of JNK signaling in promoting senescence (Figure 7K), caused either by oncogenic replication stress or by low doses of replication stress-inducing genotoxic drugs. Future work should focus on elucidating the molecular links between replication stress and activation of the JNK and Erk pathways, especially in the context of OIS and DDIS.

Heterogeneity in the behavior and response of cancer cells is now well-established,[141,142] and recent work indicates that a similar heterogeneity is present within senescent cells.[143] In this regard, it is interesting that we observed heterogeneity in the proliferative response of U2OS, NCI-H1299, OVCAR-8, and HUVEC cells following JNK and Mek inhibition in response to treatment with doxorubicin, with only a fraction of the inhibitor-treated cells escaping from senescence onset. The molecular basis for this heterogeneous response is unclear, and future work will be required to better define the underlying mechanisms, which represent a general challenge for predicting the clinically relevant biology of complex tumors during both their development and their response to treatment.[144–149]

Nonetheless, our finding of distinct early and late roles for JNK and Erk in senescence progression is of clear clinical utility, given the recent interest in the use of senolytics and SASP inhibitors for the treatment of cancer.[150–152] For example, administering a JNK or Mek inhibitor days or weeks after chemotherapy could favorably lower IL-6 and IL-8 levels secreted by treatment-induced senescent cells and thus decrease the IL-6/IL-8-mediated signaling events in the tumor microenvironment that favor cancer progression[31,153–155]; conversely, administering these inhibitors at the same time as chemotherapy could drive cells toward proliferation rather than senescence due to the early cell-fate decision-making role of JNK and Erk, resulting in tumor resistance to cytotoxic agents and hindering the efficacy of senolytic therapies later on. These findings of distinct temporal and context-dependent roles for JNK and Erk MAPKs in the setting of extrinsic genotoxic stress, however, further illustrate the extraordinary complexity and plethora of cellular responses mediated by these highly conserved signaling cascades in controlling the DDR.

STAR METHODS

Detailed methods are provided in the online version of this paper and include the following:

- Tensor PLSR and VIP score calculation
- Principal component analysis
- Inhibitor co-treatment experiments
- ELISA for IL-6 and IL-8
- Western blotting
- siRNA transfection
- Cloning and Tol2-mediated stable transfection
- c-Jun dominant negative experiments
- Retrovirus production and transduction
- AP-1-mCherry experiments
- Software

QUANTIFICATION AND STATISTICAL ANALYSIS

SUPPLEMENTAL INFORMATION

Supplemental information can be found online at https://doi.org/10.1016/j.cels.2023.06.005.

ACKNOWLEDGMENTS

We gratefully acknowledge Bjorn Millard for assistance with microscopy, Leslie Gaffney for assistance with figure design, and all members of the Yaffe lab for support and suggestions. We would also specifically like to acknowledge the reviewers for their invaluable input, which greatly improved this work. We thank the Koch Institute's Robert A. Swanson (1969) Biotechnology Center for technical support, specifically the Flow Cytometry Facility, High Throughput Sciences Facility, and Microscopy Facility, which are supported in part by the Koch Institute Support grant P30-CA14051 from the National Cancer Institute. This work was supported by NIH grants R35-ES028374 and R01-GM104047 to M.B.Y., U54-CA112967 to M.B.Y. and D.A.L., P50-GM68762 to P.K.S. and D.A.L., an NSF Graduate Research Fellowship 1122374 to T.S.N., a Ludwig Center Graduate Fellowship to T.S.N., the Ovarian Cancer Research Fund, the Charles and Marjorie Holloway Foundation, and the MIT Center for Precision Cancer Medicine.

AUTHOR CONTRIBUTIONS

T.S.N., G.J.O., and M.B.Y. designed the experiments, analyzed the data, performed computational studies, and wrote and revised the paper. T.S.N., G.J.O., A.M.D., and C.D.S. performed the experiments. A.R.T., B.A.J., K.A.J., and D.A.L. contributed to the computational analysis of the data and wrote the paper, and P.K.S. designed the experiments and analyzed the data.

DECLARATION OF INTERESTS

K.A.J., P.K.S., and D.A.L. are on the Advisory Board of *Cell Systems*.

INCLUSION AND DIVERSITY

We support inclusive, diverse, and equitable conduct of research.

Received: June 14, 2022
Revised: March 24, 2023
Accepted: June 13, 2023
Published: July 19, 2023

REFERENCES

1. Hoeijmakers, J.H.J. (2001). Genome maintenance mechanisms for preventing cancer. Nature *411*, 366–374.
2. Jackson, S.P., and Bartek, J. (2009). The DNA-damage response in human biology and disease. Nature *461*, 1071–1078. https://doi.org/10.1038/nature08467.
3. Harper, J.W., and Elledge, S.J. (2007). The DNA damage response: ten years after. Mol. Cell *28*, 739–745. https://doi.org/10.1016/j.molcel.2007.11.015.
4. Matt, S., and Hofmann, T.G. (2016). The DNA damage-induced cell death response: a roadmap to kill cancer cells. Cell. Mol. Life Sci. *73*, 2829–2850. https://doi.org/10.1007/s00018-016-2130-4.
5. Bartkova, J., Rezaei, N., Liontos, M., Karakaidos, P., Kletsas, D., Issaeva, N., Vassiliou, L.V.F., Kolettas, E., Niforou, K., Zoumpourlis, V.C., et al. (2006). Oncogene-induced senescence is part of the tumorigenesis barrier imposed by DNA damage checkpoints. Nature *444*, 633–637. https://doi.org/10.1038/nature05268.
6. D'Adda Di Fagagna, F. (2008). Living on a break: cellular senescence as a DNA-damage response. Nat. Rev. Cancer *8*, 512–522. https://doi.org/10.1038/nrc2440.
7. Gorgoulis, V.G., Vassiliou, L.V.F., Karakaidos, P., Zacharatos, P., Kotsinas, A., Liloglou, T., Venere, M., DiTullio, R.A., Kastrinakis, N.G., Levy, B., et al. (2005). Activation of the DNA damage checkpoint and genomic instability in human precancerous lesions. Nature *434*, 907–913. https://doi.org/10.1038/nature03485.
8. Van Nguyen, T., Puebla-Osorio, N., Pang, H., Dujka, M.E., and Zhu, C. (2007). DNA damage-induced cellular senescence is sufficient to suppress tumorigenesis: A mouse model. J. Exp. Med. *204*, 1453–1461. https://doi.org/10.1084/jem.20062453.
9. Halazonetis, T.D., Gorgoulis, V.G., and Bartek, J. (2008). An oncogene-induced DNA damage model for cancer development. Science *319*, 1352–1355. https://doi.org/10.1126/science.1140735.
10. Kastan, M.B., and Bartek, J. (2004). Cell-cycle checkpoints and cancer. Nature *432*, 316–323. https://doi.org/10.1038/nature03097.
11. Ciccia, A., and Elledge, S.J. (2010). The DNA damage response: making it safe to play with knives. Mol. Cell *40*, 179–204. https://doi.org/10.1016/j.molcel.2010.09.019.
12. Furuta, T., Takemura, H., Liao, Z.Y., Aune, G.J., Redon, C., Sedelnikova, O.A., Pilch, D.R., Rogakou, E.P., Celeste, A., Chen, H.T., et al. (2003). Phosphorylation of histone H2AX and activation of Mre11, Rad50, and Nbs1 in response to replication-dependent DNA double-strand breaks induced by mammalian DNA topoisomerase I cleavage complexes. J. Biol. Chem. *278*, 20303–20312. https://doi.org/10.1074/jbc.M300198200.
13. Reinhardt, H.C., and Yaffe, M.B. (2009). Kinases that control the cell cycle in response to DNA damage: Chk1, Chk2, and MK2. Curr. Opin. Cell Biol. *21*, 245–255. https://doi.org/10.1016/j.ceb.2009.01.018.
14. Levine, A.J., and Oren, M. (2009). The first 30 years of p53: growing ever more complex. Nat. Rev. Cancer *9*, 749–758. https://doi.org/10.1038/nrc2723.
15. Childs, B.G., Baker, D.J., Kirkland, J.L., Campisi, J., and van Deursen, J.M. (2014). Senescence and apoptosis: dueling or complementary cell fates? EMBO Rep. *15*, 1139–1153. https://doi.org/10.15252/embr.201439245.
16. He, G., Siddik, Z.H., Huang, Z., Wang, R., Koomen, J., Kobayashi, R., Khokhar, A.R., and Kuang, J. (2005). Induction of p21 by p53 following DNA damage inhibits both Cdk4 and Cdk2 activities. Oncogene *24*, 2929–2943. https://doi.org/10.1038/sj.onc.1208474.
17. Toshiyuki, M., and Reed, J.C. (1995). Tumor suppressor p53 is a direct transcriptional activator of the human bax gene. Cell *80*, 293–299. https://doi.org/10.1016/0092-8674(95)90412-3.
18. Helleday, T. (2008). Amplifying tumour-specific replication lesions by DNA repair inhibitors - A new era in targeted cancer therapy. Eur. J. Cancer *44*, 921–927. https://doi.org/10.1016/j.ejca.2008.02.044.
19. Helleday, T., Petermann, E., Lundin, C., Hodgson, B., and Sharma, R.A. (2008). DNA repair pathways as targets for cancer therapy. Nat. Rev. Cancer *8*, 193–204. https://doi.org/10.1038/nrc2342.
20. Kennedy, R.D., and D'Andrea, A.D. (2006). DNA repair pathways in clinical practice: lessons from pediatric cancer susceptibility syndromes. J. Clin. Oncol. *24*, 3799–3808. https://doi.org/10.1200/JCO.2005.05.4171.
21. Powell, S.N., and Bindra, R.S. (2009). Targeting the DNA damage response for cancer therapy. DNA Repair *8*, 1153–1165. https://doi.org/10.1016/j.dnarep.2009.04.011.

22. Campisi, J., and D'Adda Di Fagagna, F. (2007). Cellular senescence: when bad things happen to good cells. Nat. Rev. Mol. Cell Biol. *8*, 729–740. https://doi.org/10.1038/nrm2233.

23. D'Adda Di Fagagna, F., Reaper, P.M., Clay-Farrace, L., Fiegler, H., Carr, P., Von Zglinicki, T., Saretzki, G., Carter, N.P., and Jackson, S.P. (2003). A DNA damage checkpoint response in telomere-initiated senescence. Nature *426*, 194–198. https://doi.org/10.1038/nature02118.

24. Herbig, U., Jobling, W.A., Chen, B.P.C., Chen, D.J., and Sedivy, J.M. (2004). Telomere shortening triggers senescence of human cells through a pathway involving ATM, p53, and p21Cip1, but not p16INK4a. Mol. Cell *14*, 501–513. https://doi.org/10.1016/S1097-2765(04)00256-4.

25. Shay, J.W., and Wright, W.E. (2004). Telomeres are double-strand DNA breaks hidden from DNA damage responses. Mol. Cell *14*, 420–421. https://doi.org/10.1016/S1097-2765(04)00269-2.

26. Rodier, F., and Campisi, J. (2011). Four faces of cellular senescence. J. Cell Biol. *192*, 547–556. https://doi.org/10.1083/jcb.201009094.

27. Basisty, N., Kale, A., Jeon, O., Kuehnemann, C., Payne, T., Rao, C., Holtz, A., Shah, S., Ferrucci, L., Campisi, J., et al. (2020). A proteomic atlas of senescence-associated secretomes for aging biomarker development. PLoS Biol. *18*, 1–26. e3000599. https://doi.org/10.2139/ssrn.3380253.

28. Rodier, F., Coppé, J.P., Patil, C.K., Hoeijmakers, W.A.M., Muñoz, D.P., Raza, S.R., Freund, A., Campeau, E., Davalos, A.R., and Campisi, J. (2009). Persistent DNA damage signalling triggers senescence-associated inflammatory cytokine secretion. Nat. Cell Biol. *11*, 973–979. https://doi.org/10.1038/ncb1909.

29. Davalos, A.R., Coppe, J.P., Campisi, J., and Desprez, P.Y. (2010). Senescent cells as a source of inflammatory factors for tumor progression. Cancer Metastasis Rev. *29*, 273–283. https://doi.org/10.1007/s10555-010-9220-9.

30. Coppé, J.P., Desprez, P.Y., Krtolica, A., and Campisi, J. (2010). The senescence-associated secretory phenotype: the dark side of tumor suppression. Annu. Rev. Pathol. *5*, 99–118. https://doi.org/10.1146/annurev-pathol-121808-102144.

31. Coppé, J.P., Patil, C.K., Rodier, F., Sun, Y., Muñoz, D.P., Goldstein, J., Nelson, P.S., Desprez, P.Y., and Campisi, J. (2008). Senescence-associated secretory phenotypes reveal cell-nonautonomous functions of oncogenic RAS and the p53 tumor suppressor. PLoS Biol. *6*, 2853–2868. https://doi.org/10.1371/journal.pbio.0060301.

32. Freund, A., Patil, C.K., and Campisi, J. (2011). P38MAPK is a novel DNA damage response-independent regulator of the senescence-associated secretory phenotype. EMBO J. *30*, 1536–1548. https://doi.org/10.1038/emboj.2011.69.

33. Kim, M.J., Choi, S.Y., Park, I.C., Hwang, S.G., Kim, C., Choi, Y.H., Kim, H., Lee, K.H., and Lee, S.J. (2008). Opposing roles of c-Jun NH2-terminal kinase and p38 mitogen-activated protein kinase in the cellular response to ionizing radiation in human cervical cancer cells. Mol. Cancer Res. *6*, 1718–1731. https://doi.org/10.1158/1541-7786.MCR-08-0032.

34. Spallarossa, P., Altieri, P., Barisione, C., Passalacqua, M., Aloi, C., Fugazza, G., Frassoni, F., Podestá, M., Canepa, M., Ghigliotti, G., et al. (2010). P38 MAPK and JNK antagonistically control senescence and cytoplasmic p16ink4a expression in doxorubicin-treated endothelial progenitor cells. PLoS One *5*, e15583. https://doi.org/10.1371/journal.pone.0015583.

35. Tentner, A.R., Lee, M.J., Ostheimer, G.J., Samson, L.D., Lauffenburger, D.A., and Yaffe, M.B. (2012). Combined experimental and computational analysis of DNA damage signaling reveals context-dependent roles for Erk in apoptosis and G1 / S arrest after genotoxic stress. Mol. Syst. Biol. *8*, 568. https://doi.org/10.1038/msb.2012.1.

36. Janes, K.A., Gaudet, S., Albeck, J.G., Nielsen, U.B., Lauffenburger, D.A., and Sorger, P.K. (2006). The response of human epithelial cells to TNF involves an inducible autocrine cascade. Cell *124*, 1225–1239. https://doi.org/10.1016/j.cell.2006.01.041.

37. Manke, I.A., Nguyen, A., Lim, D., Stewart, M.Q., Elia, A.E.H., and Yaffe, M.B. (2005). MAPKAP kinase-2 is a cell cycle checkpoint kinase that regulates the G 2/M transition and S phase progression in response to UV irradiation. Mol. Cell *17*, 37–48. https://doi.org/10.1016/j.molcel.2004.11.021.

38. Ahmed, K.M., and Li, J.J. (2007). ATM-NF-κB connection as a target for tumor radiosensitization. Curr. Cancer Drug Targets *7*, 335–342. https://doi.org/10.2174/156800907780809769.

39. Lee, M.J., Ye, A.S., Gardino, A.K., Heijink, A.M., Sorger, P.K., MacBeath, G., and Yaffe, M.B. (2012). Sequential application of anticancer drugs enhances cell death by rewiring apoptotic signaling networks. Cell *149*, 780–794. https://doi.org/10.1016/j.cell.2012.03.031.

40. Reinhardt, H.C., Aslanian, A.S., Lees, J.A., and Yaffe, M.B. (2007). p53-deficient cells rely on ATM- and ATR-mediated checkpoint signaling through the p38MAPK/MK2 pathway for survival after DNA damage. Cancer Cell *11*, 175–189. https://doi.org/10.1016/j.ccr.2006.11.024.

41. Roberts, P.J., and Der, C.J. (2007). Targeting the Raf-MEK-ERK mitogen-activated protein kinase cascade for the treatment of cancer. Oncogene *26*, 3291–3310. https://doi.org/10.1038/sj.onc.1210422.

42. Kong, Y.W., Dreaden, E.C., Morandell, S., Zhou, W., Dhara, S.S., Sriram, G., Lam, F.C., Patterson, J.C., Quadir, M., Dinh, A., et al. (2020). Enhancing chemotherapy response through augmented synthetic lethality by co-targeting nucleotide excision repair and cell-cycle checkpoints. Nat. Commun. *11*, 4124. https://doi.org/10.1038/s41467-020-17958-z.

43. Janes, K.A., Kelly, J.R., Gaudet, S., Albeck, J.G., Sorger, P.K., and Lauffenburger, D.A. (2004). Cue-signal-response analysis of TNF-induced apoptosis by partial least squares regression of dynamic multivariate data. J. Comput. Biol. *11*, 544–561.

44. Gewirtz, D.A. (1999). A critical evaluation of the mechanisms of action proposed for the antitumor effects of the anthracycline antibiotics adriamycin and daunorubicin. Biochem. Pharmacol. *57*, 727–741.

45. Bodley, A., Liu, L.F., Israel, M., Seshadri, R., Koseki, Y., Giuliani, F.C., Kirschenbaum, S., Silber, R., and Potmesil, M. (1989). DNA topoisomerase II-mediated interaction of doxorubicin and daunorubicin congeners with DNA. Cancer Res. *49*, 5969–5978.

46. Maki, C.G., and Howley, P.M. (1997). Ubiquitination of p53 and p21 is differentially affected by ionizing and UV radiation. Mol. Cell. Biol. *17*, 355–363. https://doi.org/10.1128/MCB.17.1.355.

47. Park, Y.B., Park, M.J., Kimura, K., Shimizu, K., Lee, S.H., and Yokota, J. (2002). Alterations in the INK4a/ARF locus and their effects on the growth of human osteosarcoma cell lines. Cancer Genet. Cytogenet. *133*, 105–111. https://doi.org/10.1016/S0165-4608(01)00575-1.

48. Amtmann, E., Eddé, E., Sauer, G., and Westphal, O. (1990). Restoration of the responsiveness to growth factors in senescent cells by an embryonic cell extract. Exp. Cell Res. *189*, 202–207. https://doi.org/10.1016/0014-4827(90)90236-4.

49. Wansink, D.G., Schul, W., Van der Kraan, I., Van Steensel, B., Van Driel, R., and De Jong, L. (1993). Fluorescent labeling of nascent RNA reveals transcription by RNA polymerase II in domains scattered throughout the nucleus. J. Cell Biol. *122*, 283–293. https://doi.org/10.1083/jcb.122.2.283.

50. Janes, K.A., Albeck, J.G., Gaudet, S., Sorger, P.K., Lauffenburger, D.A., and Yaffe, M.B. (2005). A systems model of signaling identifies a molecular basis set for cytokine-induced apoptosis. Science *310*, 1646–1653. https://doi.org/10.1126/science.1116598.

51. Stewart, Z.A., Leach, S.D., and Pietenpol, J.A. (1999). p21 Waf1/Cip1 inhibition of cyclin E/Cdk2 activity prevents endoreduplication after mitotic spindle disruption. Mol. Cell. Biol. *19*, 205–215. https://doi.org/10.1128/MCB.19.1.205.

52. Toettcher, J.E., Loewer, A., Ostheimer, G.J., Yaffe, M.B., Tidor, B., and Lahav, G. (2009). Distinct mechanisms act in concert to mediate cell cycle arrest. Proc. Natl. Acad. Sci. USA *106*, 785–790. https://doi.org/10.1073/pnas.0806196106.

53. Janes, K.A., and Yaffe, M.B. (2006). Data-driven modelling of signal-transduction networks. Nat. Rev. Mol. Cell Biol. *7*, 820–828. https://doi.org/10.1038/nrm2041.

54. Geladi, P., and Kowalski, B.R. (1986). Partial least-squares regression: A tutorial. Anal. Chim. Acta *185*, 1–17.

55. Chitforoushzadeh, Z., Ye, Z., Sheng, Z., LaRue, S., Fry, R.C., Lauffenburger, D.A., and Janes, K.A. (2016). TNF-insulin crosstalk at the transcription factor GATA6 is revealed by a model that links signaling and transcriptomic data tensors. Sci. Signal. *9*, ra59. https://doi.org/10.1126/scisignal.aad3373.

56. Bro, R. (1996). Multiway calibration. Multilinear PLS. J. Chemom. *10*, 47–61. https://doi.org/10.1002/(SICI)1099-128X(199601)10:1<47::AID-CEM400>3.0.CO;2-C.

57. Caulk, A.W., and Janes, K.A. (2019). Robust latent-variable interpretation of in vivo regression models by nested resampling. Sci. Rep. *9*, 19671. https://doi.org/10.1038/s41598-019-55796-2.

58. Favilla, S., Durante, C., Vigni, M.L., and Cocchi, M. (2013). Assessing feature relevance in NPLS models by VIP. Chemom. Intellig Lab. Syst. *129*, 76–86. https://doi.org/10.1016/j.chemolab.2004.07.001.

59. Baldin, V., Lukas, J., Marcote, M.J., Pagano, M., and Draetta, G. (1993). Cyclin D1 is a nuclear protein required for cell cycle progression in G1. Genes Dev. *7*, 812–821. https://doi.org/10.1101/gad.7.5.812.

60. Yang, K., Hitomi, M., and Stacey, D.W. (2006). Variations in cyclin D1 levels through the cell cycle determine the proliferative fate of a cell. Cell Div. *1*, 32. https://doi.org/10.1186/1747-1028-1-32.

61. Rovillain, E., Mansfield, L., Caetano, C., Alvarez-Fernandez, M., Caballero, O.L., Medema, R.H., Hummerich, H., and Jat, P.S. (2011). Activation of nuclear factor-kappa B signalling promotes cellular senescence. Oncogene *30*, 2356–2366. https://doi.org/10.1038/onc.2010.611.

62. Tilstra, J.S., Robinson, A.R., Wang, J., Gregg, S.Q., Clauson, C.L., Reay, D.P., Nasto, L.A., St Croix, C.M., Usas, A., Vo, N., et al. (2012). NF-κB inhibition delays DNA damage-induced senescence and aging in mice. J. Clin. Invest. *122*, 2601–2612. https://doi.org/10.1172/JCI45785.

63. Chien, Y., Scuoppo, C., Wang, X., Fang, X., Balgley, B., Bolden, J.E., Premsrirut, P., Luo, W., Chicas, A., Lee, C.S., et al. (2011). Control of the senescence-associated secretory phenotype by NF-κB promotes senescence and enhances chemosensitivity. Genes Dev. *25*, 2125–2136. https://doi.org/10.1101/gad.17276711.

64. Wang, X., Martindale, J.L., and Holbrook, N.J. (2000). Requirement for ERK activation in cisplatin-induced apoptosis. J. Biol. Chem. *275*, 39435–39443. https://doi.org/10.1074/jbc.M004583200.

65. Wada, T., Stepniak, E., Hui, L., Leibbrandt, A., Katada, T., Nishina, H., Wagner, E.F., and Penninger, J.M. (2008). Antagonistic control of cell fates by JNK and p38-MAPK signaling. Cell Death Differ. *15*, 89–93. https://doi.org/10.1038/sj.cdd.4402222.

66. Xia, Z., Dickens, M., Raingeaud, J., Davis, R.J., and Greenberg, M.E. (1995). Opposing effects of ERK and JNK-p38 MAP kinases on apoptosis. Science *270*, 1326–1331. https://doi.org/10.1126/science.270.5240.1326.

67. Chen, Y.R., Meyer, C.F., and Tan, T.H. (1996). Persistent activation of c-Jun N-terminal kinase 1 (JNK1) in γ radiation-induced apoptosis. J. Biol. Chem. *271*, 631–634. https://doi.org/10.1074/jbc.271.2.631.

68. Tournier, C., Hess, P., Yang, D.D., Xu, J., Turner, T.K., Nimnual, A., Bar-Sagi, D., Jones, S.N., Flavell, R.A., and Davis, R.J. (2000). Requirement of JNK for stress-induced activation of the cytochrome c- mediated death pathway. Science *288*, 870–874. https://doi.org/10.1126/science.288.5467.870.

69. Verheij, M., Bose, R., Lin, X.H., Yao, B., Jarvis, W.D., Grant, S., Birrer, M.J., Szabo, E., Zon, L.I., Kyriakis, J.M., et al. (1996). Requirement for ceramide-initiated SAPK/JNK signalling in stress-induced apoptosis. Nature *380*, 75–79. https://doi.org/10.1038/380075a0.

70. Zanke, B.W., Boudreau, K., Rubie, E., Winnett, E., Tibbles, L.A., Zon, L., Kyriakis, J., Liu, F.F., and Woodgett, J.R. (1996). The stress-activated protein kinase pathway mediates cell death following injury induced by cis-platinum, UV irradiation or heat. Curr. Biol. *6*, 606–613. https://doi.org/10.1016/S0960-9822(02)00547-X.

71. Venkatakrishnan, C.D., Tewari, A.K., Moldovan, L., Cardounel, A.J., Zweier, J.L., Kuppusamy, P., and Ilangovan, G. (2006). Heat shock protects cardiac cells from doxorubicin-induced toxicity by activating p38 MAPK and phosphorylation of small heat shock protein 27. Am. J. Physiol. Heart Circ. Physiol. *291*, H2680–H2691. https://doi.org/10.1152/ajpheart.00395.2006.

72. Stokoe, D., Engel, K., Campbell, D.G., Cohen, P., and Gaestel, M. (1992). Identification of MAPKAP kinase 2 as a major enzyme responsible for the phosphorylation of the small mammalian heat shock proteins. FEBS Lett. *313*, 307–313. https://doi.org/10.1016/0014-5793(92)81216-9.

73. Gire, V., Roux, P., Wynford-Thomas, D., Brondello, J.M., and Dulic, V. (2004). DNA damage checkpoint kinase Chk2 triggers replicative senescence. EMBO J. *23*, 2554–2563. https://doi.org/10.1038/sj.emboj.7600259.

74. Nayak, D., Kumar, A., Chakraborty, S., Rasool, R.U., Amin, H., Katoch, A., Gopinath, V., Mahajan, V., Zilla, M.K., Rah, B., et al. (2017). Inhibition of Twist1-mediated invasion by Chk2 promotes premature senescence in p53-defective cancer cells. Cell Death Differ. *24*, 1275–1287. https://doi.org/10.1038/cdd.2017.70.

75. Lane, D.P. (1992). p53, Guardian of the Genome (Nature Publishing Group). https://doi.org/10.1038/358015a0.

76. Kumari, R., and Jat, P. (2021). Mechanisms of cellular senescence: cell cycle arrest and senescence associated secretory phenotype. Front. Cell Dev. Biol. *9*, 645593. https://doi.org/10.3389/fcell.2021.645593.

77. Serrano, M., Lin, A.W., McCurrach, M.E., Beach, D., and Lowe, S.W. (1997). Oncogenic ras provokes premature cell senescence associated with accumulation of p53 and p16(INK4a). Cell *88*, 593–602. https://doi.org/10.1016/S0092-8674(00)81902-9.

78. el-Deiry, W.S., Tokino, T., Velculescu, V.E., Levy, D.B., Parsons, R., Trent, J.M., Lin, D., Mercer, W.E., Kinzler, K.W., and Vogelstein, B. (1993). WAF1, a potential mediator of p53 tumor suppression. Cell *75*, 817–825. https://doi.org/10.1016/0092-8674(93)90500-p.

79. Brown, J.P., Wei, W., and Sedivy, J.M. (1997). Bypass of senescenoe after disruption of p21(CIP1)/(WAF1) gene in normal diploid human fibroblasts. Science *277*, 831–834. https://doi.org/10.1126/science.277.5327.831.

80. Noda, A., Ning, Y., Venable, S.F., Pereira-Smith, O.M., and Smith, J.R. (1994). Cloning of senescent cell-derived inhibitors of DNA synthesis using an expression screen. Exp. Cell Res. *211*, 90–98.

81. Wang, Y., Blandino, G., and Givol, D. (1999). Induced p21(waf) expression in H1299 cell line promotes cell senescence and protects against cytotoxic effect of radiation and doxorubicin. Oncogene *18*, 2643–2649. https://doi.org/10.1038/sj.onc.1202632.

82. Chen, P.L., Scully, P., Shew, J.Y., Wang, J.Y., and Lee, W.H. (1989). Phosphorylation of the retinoblastoma gene product is modulated during the cell cycle and cellular differentiation. Cell *58*, 1193–1198. https://doi.org/10.1016/0092-8674(89)90517-5.

83. Sellers, W.R., Rodgers, J.W., and Kaelin, W.G., Jr. (1995). A potent transrepression domain in the retinoblastoma protein induces a cell cycle arrest when bound to E2F sites. Proc. Natl. Acad. Sci. USA *92*, 11544–11548. https://doi.org/10.1073/pnas.92.25.11544.

84. Wu, C.L., Classon, M., Dyson, N., and Harlow, E. (1996). Expression of dominant-negative mutant DP-1 blocks cell cycle progression in G1. Mol. Cell. Biol. *16*, 3698–3706. https://doi.org/10.1128/MCB.16.7.3698.

85. Qin, X.Q., Livingston, D.M., Ewen, M., Sellers, W.R., Arany, Z., and Kaelin, W.G., Jr. (1995). The transcription factor E2F-1 is a downstream target of RB action. Mol. Cell. Biol. *15*, 742–755. https://doi.org/10.1128/MCB.15.2.742.

86. Kovary, K., and Bravo, R. (1991). The jun and fos protein families are both required for cell cycle progression in fibroblasts. Mol. Cell. Biol. *11*, 4466–4472. https://doi.org/10.1128/mcb.11.9.4466-4472.1991.

87. Johnson, R.S., Van Lingen, B., Papaioannou, V.E., and Spiegelman, B.M. (1993). A null mutation at the c-Jun locus causes embryonic lethality and retarded cell growth in culture. Genes Dev. *7*, 1309–1317. https://doi.org/10.1101/gad.7.7b.1309.

88. Le-Niculescu, H., Bonfoco, E., Kasuya, Y., Claret, F.-X., Green, D.R., and Karin, M. (1999). Withdrawal of survival factors results in activation of the JNK pathway in neuronal cells leading to Fas ligand induction and cell death. Mol. Cell. Biol. *19*, 751–763. https://doi.org/10.1128/MCB.19.1.751.

89. Shaulian, E., Schreiber, M., Piu, F., Beeche, M., Wagner, E.F., and Karin, M. (2000). The mammalian UV response: c-Jun induction is required for exit from p53-imposed growth arrest. Cell *103*, 897–907. https://doi.org/10.1016/s0092-8674(00)00193-8.

90. Humar, M., Loop, T., Schmidt, R., Hoetzel, A., Roesslein, M., Andriopoulos, N., Pahl, H.L., Geiger, K.K., and Pannen, B.H.J. (2007). The mitogen-activated protein kinase p38 regulates activator protein 1 by direct phosphorylation of c-Jun. Int. J. Biochem. Cell Biol. *39*, 2278–2288. https://doi.org/10.1016/j.biocel.2007.06.013.

91. Dérijard, B., Hibi, M., Wu, I.H., Barrett, T., Su, B., Deng, T., Karin, M., and Davis, R.J. (1994). JNK1: A protein kinase stimulated by UV light and Ha-Ras that binds and phosphorylates the c-Jun activation domain. Cell *76*, 1025–1037. https://doi.org/10.1016/0092-8674(94)90380-8.

92. Leppa, S., Saffrich, R., Ansorge, W., and Bohmann, D. (1998). Differential regulation of c-Jun by ERK and JNK during PC12 cell differentiation. EMBO J. *17*, 4404–4413. https://doi.org/10.1093/emboj/17.15.4404.

93. Pulverer, B.J., Kyriakis, J.M., Avruch, J., Nikolakaki, E., and Woodgett, J.R. (1991). Phosphorylation of c-Jun mediated by MAP kinases. Nature *353*, 670–674.

94. Chen, Q.M., Liu, J., and Merrett, J.B. (2000). Apoptosis or senescence-like growth arrest: influence of cell-cycle position, p53, p21 and bax in H2O2 response of normal human fibroblasts. Biochem. J. *347*, 543–551. https://doi.org/10.1042/0264-6021:3470543.

95. Fridman, J.S., and Lowe, S.W. (2003). Control of apoptosis by p53. Oncogene *22*, 9030–9040. https://doi.org/10.1038/sj.onc.1207116.

96. Vousden, K.H., and Prives, C. (2009). Blinded by the light: the growing complexity of p53. Cell *137*, 413–431. https://doi.org/10.1016/j.cell.2009.04.037.

97. Feld, R., Rubinstein, L., and Thomas, P.A. (1993). Adjuvant chemotherapy with cyclophosphamide, doxorubicin, and cisplatin in patients with completely resected stage I non-small-cell lung cancer. The lung cancer study group. J. Natl. Cancer Inst. *85*, 299–306. https://doi.org/10.1093/jnci/85.4.299.

98. Otterson, G.A., Villalona-Calero, M.A., Hicks, W., Pan, X., Ellerton, J.A., Gettinger, S.N., and Murren, J.R. (2010). Phase I/II study of inhaled doxorubicin combined with platinum-based therapy for advanced non-small cell lung cancer. Clin. Cancer Res. *16*, 2466–2473. https://doi.org/10.1158/1078-0432.CCR-09-3015.

99. Joss, R.A., Alberto, P., Obrecht, J.P., Barrelet, L., Holdener, E.E., Siegenthaler, P., Goldhirsch, A., Mermillod, B., and Cavalli, F. (1984). Combination chemotherapy for non-small cell lung cancer with doxorubicin and mitomycin or cisplatin and etoposide. Cancer Treat. Rep. *68*, 1079–1084.

100. Kuilman, T., Michaloglou, C., Vredeveld, L.C.W., Douma, S., van Doorn, R., Desmet, C.J., Aarden, L.A., Mooi, W.J., and Peeper, D.S. (2008). Oncogene-induced senescence relayed by an interleukin-dependent inflammatory network. Cell *133*, 1019–1031. https://doi.org/10.1016/j.cell.2008.03.039.

101. Hoffmann, E., Thiefes, A., Buhrow, D., Dittrich-Breiholz, O., Schneider, H., Resch, K., and Kracht, M. (2005). MEK1-dependent delayed expression of fos-related antigen-1 counteracts c-Fos and p65 NF-κB-mediated interleukin-8 transcription in response to cytokines or growth factors. J. Biol. Chem. *280*, 9706–9718. https://doi.org/10.1074/jbc.M407071200.

102. Krause, A., Holtmann, H., Eickemeier, S., Winzen, R., Szamel, M., Resch, K., Saklatvala, J., and Kracht, M. (1998). Stress-activated protein kinase/Jun N-terminal kinase is required for interleukin (IL)-1-induced IL-6 and IL-8 gene expression in the human epidermal carcinoma cell line KB. J. Biol. Chem. *273*, 23681–23689. https://doi.org/10.1074/jbc.273.37.23681.

103. Thompson, E.J., Gupta, A., Stratton, M.S., and Bowden, G.T. (2002). Mechanism of action of a dominant negative c-Jun mutant in inhibiting activator protein-1 activation. Mol. Carcinog. *35*, 157–162. https://doi.org/10.1002/mc.10090.

104. Tewey, K.M., Rowe, T.C., Yang, L., Halligan, B.D., and Liu, L.F. (1984). Adriamycin-induced DNA damage mediated by mammalian DNA topoisomerase II. Science *226*, 466–468. https://doi.org/10.1126/science.6093249.

105. Zellweger, R., Dalcher, D., Mutreja, K., Berti, M., Schmid, J.A., Herrador, R., Vindigni, A., and Lopes, M. (2015). Rad51-mediated replication fork reversal is a global response to genotoxic treatments in human cells. J. Cell Biol. *208*, 563–579. https://doi.org/10.1083/jcb.201406099.

106. Durr, F.E., Wallace, R.E., and Citarella, R.V. (1983). Molecular and biochemical pharmacology of mitoxantrone. Cancer Treat. Rev. *10*, 3–11. https://doi.org/10.1016/0305-7372(83)90016-6.

107. Zhao, H., Rybak, P., Dobrucki, J., Traganos, F., and Darzynkiewicz, Z. (2012). Relationship of DNA damage signaling to DNA replication following treatment with DNA topoisomerase inhibitors camptothecin/topotecan, mitoxantrone, or etoposide. Cytometry A *81*, 45–51. https://doi.org/10.1002/cyto.a.21172.

108. Olson, E., Nievera, C.J., Klimovich, V., Fanning, E., and Wu, X. (2006). RPA2 is a direct downstream target for ATR to regulate the S-phase checkpoint. J. Biol. Chem. *281*, 39517–39533. https://doi.org/10.1074/jbc.M605121200.

109. Vassin, V.M., Anantha, R.W., Sokolova, E., Kanner, S., and Borowiec, J.A. (2009). Human RPA phosphorylation by ATR stimulates DNA synthesis and prevents ssDNA accumulation during DNA-replication stress. J. Cell Sci. *122*, 4070–4080. https://doi.org/10.1242/jcs.053702.

110. Zuazua-Villar, P., Ganesh, A., Phear, G., Gagou, M.E., and Meuth, M. (2015). Extensive RPA2 hyperphosphorylation promotes apoptosis in response to DNA replication stress in CHK1 inhibited cells. Nucleic Acids Res. *43*, 9776–9787. https://doi.org/10.1093/nar/gkv835.

111. Cuella-Martin, R., Oliveira, C., Lockstone, H.E., Snellenberg, S., Grolmusova, N., and Chapman, J.R. (2016). 53BP1 integrates DNA repair and p53-dependent cell fate decisions via distinct mechanisms. Mol. Cell *64*, 51–64. https://doi.org/10.1016/j.molcel.2016.08.002.

112. Fernando, R.N., Eleuteri, B., Abdelhady, S., Nussenzweig, A., Andang, M., and Ernfors, P. (2011). Cell cycle restriction by histone H2AX limits proliferation of adult neural stem cells. Proc. Natl. Acad. Sci. USA *108*, 5837–5842. https://doi.org/10.1073/pnas.1014993108.

113. Reyes, J., Chen, J.Y., Stewart-Ornstein, J., Karhohs, K.W., Mock, C.S., and Lahav, G. (2018). Fluctuations in p53 signaling allow escape from cell-cycle arrest. Mol. Cell *71*, 581–591.e5. https://doi.org/10.1016/j.molcel.2018.06.031.

114. Hsu, C.H., Altschuler, S.J., and Wu, L.F. (2019). Patterns of early p21 dynamics determine proliferation-senescence cell fate after chemotherapy. Cell *178*, 361–373.e12. https://doi.org/10.1016/j.cell.2019.05.041.

115. Hubner, A., Barrett, T., Flavell, R.A., and Davis, R.J. (2008). Multisite phosphorylation regulates Bim stability and apoptotic activity. Mol. Cell *30*, 415–425. https://doi.org/10.1016/j.molcel.2008.03.025.

116. Kennedy, N.J., Sluss, H.K., Jones, S.N., Bar-Sagi, D., Flavell, R.A., and Davis, R.J. (2003). Suppression of Ras-stimulated transformation by the JNK signal transduction pathway. Genes Dev. *17*, 629–637. https://doi.org/10.1101/gad.1062903.

117. Lei, K., and Davis, R.J. (2003). JNK phosphorylation of Bim-related members of the Bcl2 family induces Bax-dependent apoptosis. Proc. Natl. Acad. Sci. USA *100*, 2432–2437. https://doi.org/10.1073/pnas.0438011100.

118. Donovan, N., Becker, E.B.E., Konishi, Y., and Bonni, A. (2002). JNK phosphorylation and activation of BAD couples the stress-activated signaling pathway to the cell death machinery. J. Biol. Chem. *277*, 40944–40949. https://doi.org/10.1074/jbc.M206113200.

119. Tsuruta, F., Sunayama, J., Mori, Y., Hattori, S., Shimizu, S., Tsujimoto, Y., Yoshioka, K., Masuyama, N., and Gotoh, Y. (2004). JNK promotes Bax translocation to mitochondria through phosphorylation of 14–3-3 proteins. EMBO J. *23*, 1889–1899. https://doi.org/10.1038/sj.emboj.7600194.

120. Sunayama, J., Tsuruta, F., Masuyama, N., and Gotoh, Y. (2005). JNK antagonizes Akt-mediated survival signals by phosphorylating 14-3-3. J. Cell Biol. *170*, 295–304. https://doi.org/10.1083/jcb.200409117.

121. Oleinik, N.V., Krupenko, N.I., and Krupenko, S.A. (2007). Cooperation between JNK1 and JNK2 in activation of p53 apoptotic pathway. Oncogene *26*, 7222–7230. https://doi.org/10.1038/sj.onc.1210526.

122. Jones, E.V., Dickman, M.J., and Whitmarsh, A.J. (2007). Regulation of p73-mediated apoptosis by c-Jun N-terminal kinase. Biochem. J. *405*, 617–623. https://doi.org/10.1042/BJ20061778.

123. Dhanasekaran, D.N., and Reddy, E.P. (2017). JNK-signaling: A multiplexing hub in programmed cell death. Genes Cancer *8*, 682–694. https://doi.org/10.18632/genesandcancer.155.

124. Das, M., Jiang, F., Sluss, H.K., Zhang, C., Shokat, K.M., Flavell, R.A., and Davis, R.J. (2007). Suppression of p53-dependent senescence by the JNK signal transduction pathway. Proc. Natl. Acad. Sci. USA *104*, 15759–15764. https://doi.org/10.1073/pnas.0707782104.

125. Lavoie, H., Gagnon, J., and Therrien, M. (2020). ERK signalling: a master regulator of cell behaviour, life and fate. Nat. Rev. Mol. Cell Biol. *21*, 607–632. https://doi.org/10.1038/s41580-020-0255-7.

126. Spelat, R., Ferro, F., and Curcio, F. (2012). Serine 111 phosphorylation regulates OCT4A protein subcellular distribution and degradation. J. Biol. Chem. *287*, 38279–38288. https://doi.org/10.1074/jbc.M112.386755.

127. Kim, M.O., Kim, S.H., Cho, Y.Y., Nadas, J., Jeong, C.H., Yao, K., Kim, D.J., Yu, D.H., Keum, Y.S., Lee, K.Y., et al. (2012). ERK1 and ERK2 regulate embryonic stem cell self-renewal through phosphorylation of Klf4. Nat. Struct. Mol. Biol. *19*, 283–290. https://doi.org/10.1038/nsmb.2217.

128. Yeo, J.C., Jiang, J., Tan, Z.Y., Yim, G.R., Ng, J.H., Göke, J., Kraus, P., Liang, H., Gonzales, K.A.U., Chong, H.C., et al. (2014). Klf2 is an essential factor that sustains ground state pluripotency. Cell Stem Cell *14*, 864–872. https://doi.org/10.1016/j.stem.2014.04.015.

129. Yeh, P.Y., Chuang, S.E., Yeh, K.H., Song, Y.C., Chang, L.L.Y., and Cheng, A.L. (2004). Phosphorylation of p53 on Thr55 by ERK2 is necessary for doxorubicin-induced p53 activation and cell death. Oncogene *23*, 3580–3588. https://doi.org/10.1038/sj.onc.1207426.

130. Lin, A.W., Barradas, M., Stone, J.C., Van Aelst, L., Serrano, M., and Lowe, S.W. (1998). Premature senescence involving p53 and p16 is activated in response to constitutive MEK/MAPK mitogenic signaling. Genes Dev. *12*, 3008–3019. https://doi.org/10.1101/gad.12.19.3008.

131. Wang, W., Chen, J.X., Liao, R., Deng, Q., Zhou, J.J., Huang, S., and Sun, P. (2002). Sequential Activation of the MEK-extracellular signal-regulated kinase and MKK3/6-p38 mitogen-activated protein kinase Pathways Mediates Oncogenic ras -Induced Premature Senescence. Mol. Cell. Biol. *22*, 3389–3403. https://doi.org/10.1128/MCB.22.10.3389-3403.2002.

132. Zhu, J., Woods, D., McMahon, M., and Bishop, J.M. (1998). Senescence of human fibroblasts induced by oncogenic Raf. Genes Dev. *12*, 2997–3007. https://doi.org/10.1101/gad.12.19.2997.

133. Roux, P.P., and Blenis, J. (2004). ERK and p38 MAPK-activated protein kinases: a family of protein kinases with diverse biological functions. Microbiol. Mol. Biol. Rev. *68*, 320–344. https://doi.org/10.1128/MMBR.68.2.320-344.2004.

134. Reinhardt, H.C., Hasskamp, P., Schmedding, I., Morandell, S., van Vugt, M.A.T.M., Wang, X.Z., Linding, R., Ong, S.E., Weaver, D., Carr, S.A., et al. (2010). DNA damage activates a spatially distinct late cytoplasmic cell-cycle checkpoint network controlled by MK2-mediated RNA stabilization. Mol. Cell *40*, 34–49. https://doi.org/10.1016/j.molcel.2010.09.018.

135. Cannell, I.G., Merrick, K.A., Morandell, S., Zhu, C.Q., Braun, C.J., Grant, R.A., Cameron, E.R., Tsao, M.S., Hemann, M.T., and Yaffe, M.B. (2015). A pleiotropic RNA-binding protein controls distinct cell cycle checkpoints to drive resistance of p53-defective tumors to chemotherapy. Cancer Cell *28*, 623–637. https://doi.org/10.1016/j.ccell.2015.09.009.

136. Morandell, S., Reinhardt, H.C., Cannell, I.G., Kim, J.S., Ruf, D.M., Mitra, T., Couvillon, A.D., Jacks, T., and Yaffe, M.B. (2013). A reversible gene-targeting strategy identifies synthetic lethal interactions between MK2 and p53 in the DNA damage response invivo. Cell Rep. *5*, 868–877. https://doi.org/10.1016/j.celrep.2013.10.025.

137. Eferl, R., and Wagner, E.F. (2003). AP-1: A double-edged sword in tumorigenesis. Nat. Rev. Cancer *3*, 859–868. https://doi.org/10.1038/nrc1209.

138. Martínez-Zamudio, R.I., Roux, P.F., de Freitas, J.A.N.L.F., Robinson, L., Doré, G., Sun, B., Belenki, D., Milanovic, M., Herbig, U., Schmitt, C.A., et al. (2020). AP-1 imprints a reversible transcriptional programme of senescent cells. Nat. Cell Biol. *22*, 842–855. https://doi.org/10.1038/s41556-020-0529-5.

139. Han, R., Li, L., Ugalde, A.P., Tal, A., Manber, Z., Barbera, E.P., Chiara, V.D., Elkon, R., and Agami, R. (2018). Functional CRISPR screen identifies AP1-associated enhancer regulating FOXF1 to modulate oncogene-induced senescence. Genome Biol. *19*, 1–13. https://doi.org/10.1186/s13059-018-1494-1.

140. Hubner, A., Mulholland, D.J., Standen, C.L., Karasarides, M., Cavanagh-Kyros, J., Barrett, T., Chi, H., Greiner, D.L., Tournier, C., Sawyers, C.L., et al. (2012). JNK and PTEN cooperatively control the development of invasive adenocarcinoma of the prostate. Proc. Natl. Acad. Sci. USA *109*, 12046–12051. https://doi.org/10.1073/pnas.1209660109.

141. Dagogo-Jack, I., and Shaw, A.T. (2018). Tumour heterogeneity and resistance to cancer therapies. Nat. Rev. Clin. Oncol. *15*, 81–94. https://doi.org/10.1038/nrclinonc.2017.166.

142. De Sousa E Melo, F.D.S.E., Vermeulen, L., Fessler, E., and Medema, J.P. (2013). Cancer heterogeneity - A multifaceted view. EMBO Rep. *14*, 686–695. https://doi.org/10.1038/embor.2013.92.

143. Cohn, R.L., Gasek, N.S., Kuchel, G.A., and Xu, M. (2022). The heterogeneity of cellular senescence: insights at the single-cell level. Trends Cell Biol. 1–9. https://doi.org/10.1016/j.tcb.2022.04.011.

144. Quintana, E., Shackleton, M., Foster, H.R., Fullen, D.R., Sabel, M.S., Johnson, T.M., and Morrison, S.J. (2010). Phenotypic heterogeneity among tumorigenic melanoma cells from patients that is reversible and not hierarchically organized. Cancer Cell *18*, 510–523. https://doi.org/10.1016/j.ccr.2010.10.012.

145. Kemper, K., Krijgsman, O., Cornelissen Steijger, P., Shahrabi, A., Weeber, F., Song, J.Y., Kuilman, T., Vis, D.J., Wessels, L.F., Voest, E.E., et al. (2015). Intra and inter tumor heterogeneity in a vemurafenib resistant melanoma patient and derived xenografts. EMBO Mol. Med. *7*, 1104–1118. https://doi.org/10.15252/emmm.201404914.

146. Morrissy, A.S., Garzia, L., Shih, D.J.H., Zuyderduyn, S., Huang, X., Skowron, P., Remke, M., Cavalli, F.M.G., Ramaswamy, V., Lindsay, P.E., et al. (2016). Divergent clonal selection dominates medulloblastoma at recurrence. Nature *529*, 351–357. https://doi.org/10.1038/nature16478.

147. Zhao, B., Hemann, M.T., and Lauffenburger, D.A. (2014). Intratumor heterogeneity alters most effective drugs in designed combinations. Proc. Natl. Acad. Sci. USA *111*, 10773–10778. https://doi.org/10.1073/pnas.1323934111.

148. Marusyk, A., Tabassum, D.P., Altrock, P.M., Almendro, V., Michor, F., and Polyak, K. (2014). Non-cell-autonomous driving of tumour growth supports sub-clonal heterogeneity. Nature *514*, 54–58. https://doi.org/10.1038/nature13556.

149. Chapman, A., Fernandez del Ama, L.F., Ferguson, J., Kamarashev, J., Wellbrock, C., and Hurlstone, A. (2014). Heterogeneous tumor subpopulations cooperate to drive invasion. Cell Rep. *8*, 688–695. https://doi.org/10.1016/j.celrep.2014.06.045.

150. Wang, L., Lankhorst, L., and Bernards, R. (2022). Exploiting senescence for the treatment of cancer. Nat. Rev. Cancer *22*, 340–355. https://doi.org/10.1038/s41568-022-00450-9.

151. Fielder, E., Wan, T., Alimohammadiha, G., Ishaq, A., Low, E., Weigand, B.M., Kelly, G., Parker, C., Griffin, B., Jurk, D., et al. (2022). Short senolytic or senostatic interventions rescue progression of radiation-induced frailty and premature ageing in mice. eLife *11*, 1–29. https://doi.org/10.7554/eLife.75492.

152. Short, S., Fielder, E., Miwa, S., and von Zglinicki, T. (2019). Senolytics and senostatics as adjuvant tumour therapy. EBiomedicine *41*, 683–692. https://doi.org/10.1016/j.ebiom.2019.01.056.

153. Ruhland, M.K., Loza, A.J., Capietto, A.H., Luo, X., Knolhoff, B.L., Flanagan, K.C., Belt, B.A., Alspach, E., Leahy, K., Luo, J., et al. (2016). Stromal senescence establishes an immunosuppressive microenvironment that drives tumorigenesis. Nat. Commun. *7*, 11762. https://doi.org/10.1038/ncomms11762.

154. Wu, J., Gao, F.X., Wang, C., Qin, M., Han, F., Xu, T., Hu, Z., Long, Y., He, X.M., Deng, X., et al. (2019). IL-6 and IL-8 secreted by tumour cells impair the function of NK cells via the STAT3 pathway in oesophageal squamous cell carcinoma. J. Exp. Clin. Cancer Res. *38*, 321. https://doi.org/10.1186/s13046-019-1310-0.

155. Goulet, C.R., Champagne, A., Bernard, G., Vandal, D., Chabaud, S., Pouliot, F., and Bolduc, S. (2019). Cancer-associated fibroblasts induce epithelial-mesenchymal transition of bladder cancer cells through paracrine IL-6 signalling. BMC Cancer *19*, 137. https://doi.org/10.1186/s12885-019-5353-6.

156. Wang, Z.-Y., Sato, H., Kusam, S., Sehra, S., Toney, L.M., and Dent, A.L. (2005). Regulation of IL-10 gene expression in Th2 cells by jun proteins. J. Immunol. *174*, 2098–2105. https://doi.org/10.4049/jimmunol.174.4.2098.

157. Balciunas, D., Wangensteen, K.J., Wilber, A., Bell, J., Geurts, A., Sivasubbu, S., Wang, X., Hackett, P.B., Largaespada, D.A., McIvor, R.S., et al. (2006). Harnessing a high cargo-capacity transposon for genetic applications in vertebrates. PLoS Genet. *2*, e169. https://doi.org/10.1371/journal.pgen.0020169.

158. Jutz, S., Leitner, J., Schmetterer, K., Doel-Perez, I., Majdic, O., Grabmeier-Pfistershammer, K., Paster, W., Huppa, J.B., and Steinberger, P. (2016). Assessment of costimulation and coinhibition in a triple parameter T cell reporter line: simultaneous measurement of NF-κB, NFAT and AP-1. J. Immunol. Methods *430*, 10–20. https://doi.org/10.1016/j.jim.2016.01.007.

159. Stewart, S.A., Dykxhoorn, D.M., Palliser, D., Mizuno, H., Yu, E.Y., An, D.S., Sabatini, D.M., Chen, I.S.Y., Hahn, W.C., Sharp, P.A., et al. (2003). Lentivirus-delivered stable gene silencing by RNAi in primary cells. RNA *9*, 493–501. https://doi.org/10.1261/rna.2192803.

160. Schindelin, J., Arganda-Carreras, I., Frise, E., Kaynig, V., Longair, M., Pietzsch, T., Preibisch, S., Rueden, C., Saalfeld, S., Schmid, B., et al. (2012). Fiji: an open-source platform for biological-image analysis. Nat. Methods *9*, 676–682. https://doi.org/10.1038/nmeth.2019.

161. Stirling, D.R., Swain-Bowden, M.J., Lucas, A.M., Carpenter, A.E., Cimini, B.A., and Goodman, A. (2021). CellProfiler 4: improvements in speed, utility and usability. BMC Bioinform. *22*, 433. https://doi.org/10.1186/s12859-021-04344-9.

162. Berg, S., Kutra, D., Kroeger, T., Straehle, C.N., Kausler, B.X., Haubold, C., Schiegg, M., Ales, J., Beier, T., Rudy, M., et al. (2019). Ilastik: interactive machine learning for (bio)image analysis. Nat. Methods *16*, 1226–1232. https://doi.org/10.1038/s41592-019-0582-9.

163. Favilla, S., Huber, A., Pagnoni, G., Lui, F., Facchin, P., Cocchi, M., Baraldi, P., and Porro, C.A. (2014). Ranking brain areas encoding the perceived level of pain from fMRI data. Neuroimage *90*, 153–162. https://doi.org/10.1016/j.neuroimage.2014.01.001.

STAR METHODS

KEY RESOURCES TABLE

REAGENT or RESOURCE	SOURCE	IDENTIFIER
Antibodies		
Mouse monoclonal anti-γ-H2AX	Millipore	Cat 05-636; RRID:AB_309864
Rabbit monoclonal anti-phospho-Akt	Cell Signaling Technology	Cat 4058; RRID:AB_331168
Rabbit monoclonal anti-phospho-Erk	Cell Signaling Technology	Cat 4377; RRID:AB_331775
Rabbit monoclonal anti-phospho-Erk	Cell Signaling Technology	Cat 4370; RRID:AB_2315112
Mouse monoclonal anti-Erk	Cell Signaling Technology	Cat 4696; RRID:AB_390780
Rabbit polyclonal anti-phospho-JNK	Cell Signaling Technology	Cat 9251; RRID:AB_331659
Rabbit polyclonal anti-JNK	Cell Signaling Technology	Cat 9252; RRID:AB_2250373
Mouse monoclonal anti-NF-κB	Santa Cruz	Cat sc-8008; RRID:AB_628017
Rabbit monoclonal anti-phospho-p38	Cell Signaling Technology	Cat 4631; RRID:AB_331765
Rabbit polyclonal anti-p38	Cell Signaling Technology	Cat 9212; RRID:AB_330713
Rabbit monoclonal phospho-MK2	Cell Signaling Technology	Cat 3007; RRID:AB_490936
Rabbit anti-MK2	Cell Signaling Technology	Cat 3042; RRID:AB_10694238
Rabbit monoclonal anti-phospho-S6	Cell Signaling Technology	Cat 4856; RRID:AB_2181037
Mouse monoclonal anti-p27	Santa Cruz	Cat sc-1641; RRID:AB_628074
Rabbit monoclonal anti-p27	Cell Signaling Technology	Cat 3686; RRID:AB_2077850
Rabbit polyclonal anti-phospho-Hsp27	Cell Signaling Technology	Cat 2401; RRID:AB_331644
Mouse monoclonal anti-p53	Santa Cruz	Cat sc-263; RRID:AB_628084
Rabbit polyclonal anti-phospho-c-Jun(Ser 73)	Cell Signaling Technology	Cat 9164; RRID:AB_330892
Rabbit monoclonal anti-phospho-c-Jun(Ser 73)	Cell Signaling Technology	Cat 3270; RRID:AB_2129575
Rabbit polyclonal anti-phospho-c-Jun(Ser 63)	Cell Signaling Technology	Cat 9261; RRID:AB_2130162
Rabbit monoclonal anti-c-Jun	Cell Signaling Technology	Cat 9165; RRID:AB_2130165
Rabbit polyclonal anti-phospho-Chk2	Cell Signaling Technology	Cat 2661; RRID:AB_331479
Mouse monoclonal anti-IκB	BD Biosciences	Cat 610691; RRID:AB_398014
Mouse monoclonal anti-IκB	Cell Signaling Technology	Cat 4814; RRID:AB_390781
Mouse monoclonal anti-Cyclin D	Santa Cruz	Cat sc-20044; RRID:AB_627346
Rabbit polyclonal anti-phospho-Rb	Cell Signaling Technology	Cat 9308; RRID:AB_331472
Mouse monoclonal anti-Cyclin E	Santa Cruz	Cat sc-247; RRID:AB_627357
Rabbit polyclonal anti-Cyclin A	Santa Cruz	Cat sc-751; RRID:AB_631329
Mouse monoclonal anti-p21	Millipore	Cat 05-345; RRID:AB_309684
Rabbit monoclonal anti-p21	Cell Signaling Technology	Cat 2947; RRID:AB_823586
Rabbit monoclonal anti-p16	Cell Signaling Technology	Cat 18769; RRID:AB_2935679
Rabbit polyclonal anti-Cyclin B	Santa Cruz	Cat sc-752; RRID:AB_2072134
Rabbit monoclonal anti-Cyclin B	Cell Signaling Technology	Cat 12231; RRID:AB_2783553
Mouse monoclonal anti-BrdU	BD Biosciences	Cat 555627; RRID:AB_395993
Mouse monoclonal anti-BrdU	Cell Signaling Technology	Cat 5292S; RRID:AB_10548898
Rabbit polyclonal anti-phospho-RPA2(Ser 8)	Cell Signaling Technology	Cat 83745; RRID:AB_2800029
Rabbit monoclonal anti-RPA2	Cell Signaling Technology	Cat 35869; RRID:AB_2799086
Mouse monoclonal anti-β-tubulin	Sigma-Aldrich	Cat T7816; RRID:AB_261770
Mouse monoclonal anti-GAPDH	Cell Signaling Technology	Cat 97166; RRID:AB_2756824

(*Continued on next page*)

ontinued

REAGENT or RESOURCE	SOURCE	IDENTIFIER
Rabbit monoclonal anti-cleaved caspase-3	BD Biosciences	Cat 559565; RRID:AB_397274
Mouse monoclonal anti-cleaved PARP	BD Biosciences	Cat 558710; RRID:AB_1645431
Rabbit polyclonal anti-Cyclin B	Santa Cruz	Cat sc-752; RRID:AB_2072134
Mouse monoclonal anti-p21	Millipore	Cat 05-345; RRID:AB_309684
Goat polyclonal anti-rabbit conjugated to Alexa Fluor 488	Invitrogen	Cat A-11008; RRID:AB_143165
Goat polyclonal anti-rabbit conjugated to Alexa Fluor 647	Invitrogen	Cat A-21245; RRID:AB_141775
Goat polyclonal anti-mouse conjugated to Alexa Fluor 647	Invitrogen	Cat A-21236; RRID:AB_2535805
IRDye® 680RD Goat anti-Mouse IgG Secondary Antibody	LI-COR Biosciences	Cat 926-68070; RRID: RRID:AB_10956588
IRDye® 800CW Goat anti-Rabbit IgG Secondary Antibody	LI-COR Biosciences	Cat 926-32211; RRID:AB_621843
IRDye® 680RD Goat anti-Rabbit IgG Secondary Antibody	LI-COR Biosciences	Cat 926-68071; RRID:AB_10956166
IRDye® 800CW Goat anti-Mouse IgG Secondary Antibody	LI-COR Biosciences	Cat 926-32210; RRID:AB_621842
Bacterial and virus strains		
Competent DH5 *E. coli*	This paper	NA
Chemicals, peptides, and recombinant proteins		
DMEM	Corning	10-013-CV
Fetal bovine serum (FBS)	VWR	97068-085
Penicillin-streptomycin	Gibco	15070063
RPMI	Gibco	11875093
EBM-2 endothelial cell growth medium	Lonza	CC-3162
Doxorubicin hydrochloride	Sigma-Aldrich	PHR1789; CAS: 25316-40-9
SP600125	Sigma-Aldrich	S5567; CAS: 129-56-6
Neocarzinostatin	Sigma-Aldrich	N9162; CAS: 9014-02-2
Cisplatin	Sigma-Aldrich	P4394; CAS: 15663-27-1
Caffeine	Sigma-Aldrich	C0750; CAS: 58-08-2
Phorbol 12-myristate 13-acetate (PMA)	Sigma-Aldrich	P1585; CAS: 16561-29-8
Anisomycin	Sigma-Aldrich	A9789; CAS: 22862-76-6
PD98059	Cell Signaling Technology	9900; CAS: 167869-21-8
SB203580	Tocris	1202; CAS: 152121-47-6
Mitoxantrone	Tocris	4250; CAS: 70476-82-3
Doxycycline	Clontech	631311; CAS: 564-25-0
DMSO	Sigma-Aldrich	D8418; CAS: 67-68-5
5-bromo-2'-deoxyuridine (BrdU)	ThermoFisher	B23151; CAS: 59-14-3
16% Paraformaldehyde	Electron Microscopy Science	15710; CAS: 30525-89-4
PBS	GenClone	25-507B
Triton-X 100	Sigma-Aldrich	T9284; CAS: 9036-19-5
HCS CellMask Blue	ThermoFisher	H32720
Hoechst 33342	Invitrogen	H3570
Whole Cell Blue	ThermoFisher	8403502
5-ethynyl-2'-deoxyuridine (EdU)	ThermoFisher	A10044

(*Continued on next page*)

continued

REAGENT or RESOURCE	SOURCE	IDENTIFIER
ProLong Gold Antifade Mount	ThermoFisher	P36980
Odyssey Blocking Buffer	LI-COR Biosciences	927-50000
Propidium iodide with RNase A	Cell Signaling Technology	4087
Tween 20	AmericanBio	AB02038; CAS: 9005-64-5
PhosSTOP™ tablets	Roche	4906837001
cOmplete™ ULTRA Tablets, Mini, EDTA-free, EASYpack Protease Inhibitor Cocktail	Roche	05892791001
Ponceau stain	Sigma-Aldrich	P7170
Intercept blocking buffer	Licor	927-70001
NewBlot nitrocellulose stripping buffer	Licor	928-40030
Lipofectamine RNAiMAX	ThermoFisher	13778150
Opti-MEM	ThermoFisher	11058021
Lipofectamine 2000	ThermoFisher	11668019
Puromycin	InvivoGen	ant-pr-1; CAS: 58-58-2
Hydrochloric acid	Sigma-Aldrich	258148; CAS: 7647-01-1
Citric acid	Sigma-Aldrich	C-4540; CAS: 77-92-9
Sodium phosphate monobasic	Sigma-Aldrich	S0751; CAS: 7558-80-7
Phusion® High-Fidelity PCR Master Mix with HF Buffer	NEB	M0531S
NheI-HF®	NEB	R3131L
EcoRI-HF®	NEB	R3101L
NEBuilder® HiFi DNA Assembly Master Mix	NEB	E2621S
Critical commercial assays		
Senescence β-Galactosidase Staining Kit	Cell Signaling Technology	9860
Click-iT Plus Alexa Fluor 555 Picolyl Azide Toolkit	ThermoFisher	C10642
IL-6 Human ELISA Kit	ThermoFisher	KHC0061
IL-8 Human ELISA Kit	ThermoFisher	KHC0081
BCA assay	ThermoFisher	23225
CalPhos™ Mammalian Transfection Kit	Clontech	631312
Experimental models: Cell lines		
Human: U-2 OS (U2OS)	HTS core at the Koch Institute	RRID:CVCL_T429
Human: OVCAR-8	Laboratory of Dr. Paula Hammond	RRID:CVCL_1629
Human: NCI-H1299	ATCC	RRID:CVCL_0060
Human: HUVEC	Lonza	RRID:CVCL_2959
Human: HEK293T	ATCC	RRID:CVCL_0063
Oligonucleotides		
Non-targeting siRNA	Invitrogen	AM4636
Jun 1 siRNA	Life Technologies	s7658
Jun 2 siRNA	Life Technologies	s7659
Recombinant DNA		
pAK-Tol2-TRE-JunDN-HA-T2A-GFP (pTRE-JunDN-HA-T2A-GFP)	This paper	N/A
pAK-Tol2-TRE-GFP (pTRE-GFP)	This paper	N/A
pMIEG3-JunDN	Addgene 40350	Wang et al.[156]
pCMV-Tol2	Addgene 31823	Balciunas et al.[157]
pAK-Tol2-TRE-Puro	Addgene 130259	N/A
pSIRV-AP-1-mCherry	Addgene 118095	Jutz et al.[158]
pUMVC	Addgene 8849	Stewart et al.[159]

(*Continued on next page*)

ontinued

REAGENT or RESOURCE	SOURCE	IDENTIFIER
pCMV-VSV-G	Addgene 8454	Stewart et al.[159]
Software and algorithms		
Fiji distribution of ImageJ	Schindelin et al.[160]	https://fiji.sc/
CellProfiler (version 4.0.6)	Stirling et al.[161]	https://cellprofiler.org/
MATLAB (2019b)	MathWorks	https://www.mathworks.com
FlowJo (version 10)	BD Biosciences	https://www.flowjo.com/
Python (version 3.7)	Python Software Foundation	https://www.python.org/
N-way Toolbox (version 1.8.0.0)	Bro[56]	https://www.mathworks.com/matlabcentral/fileexchange/1088-the-n-way-toolbox
Multi-way VIP	Favilla et al.[58]	Obtained from corresponding author upon request
Tensor PLSR and PCA code	This paper	https://doi.org/10.5281/zenodo.7927324
ilastik	Berg et al.[162]	https://www.ilastik.org/
GraphPad Prism (version 8.4.1)	Dotmatics	https://www.graphpad.com/
NIS Viewer	Nikon	https://www.microscope.healthcare.nikon.com/products/software/nis-elements/viewer
Image Studio Lite (version 5.2)	LI-COR Biosciences	https://www.licor.com/bio/image-studio-lite/
Other		
Corning™ BioCoat™ 12mm 1 German Glass Coverslips, Round	Fisher Scientific	08-774-383
96 Well Black/Clear Bottom Plate, TC Surface	ThermoFisher	165305

RESOURCE AVAILABILITY

Lead contact

Further information and requests for resources and reagents should be directed to and will be fulfilled by the lead contact, Michael Yaffe (myaffe@mit.edu).

Materials availability

Plasmids and cell lines generated in this study are available upon request.

Data and code availability

Source data statement: All data reported in this paper will be shared by the lead contact upon reasonable request.

Code statement: Raw quantified data and MATLAB scripts used to construct t-PLSR and PCA results can be found at: github.com/yaffelab/CellFate-TensorPLSR. The DOI is listed in the key resources table.

Any additional information required to reanalyze the data reported in this paper is available from the lead contact upon request.

EXPERIMENTAL MODEL AND SUBJECT DETAILS

U-2 OS (U2OS) and HEK293T cells were purchased from the American Type Culture Collection (ATCC), and cultured in complete media consisting of Dulbecco's Modified Eagle's Medium (DMEM, Corning) supplemented with 10% fetal bovine serum (FBS, VWR) and 1% penicillin-streptomycin (pen-strep, Gibco). NCI-H1299 cells were purchased from ATCC, and cultured in RPMI (Gibco) supplemented with 10% FBS and 1% pen-strep. HUVEC cells were purchased from Lonza and cultured in complete EBM-2 endothelial cell growth medium (Lonza). OVCAR-8 cells were a gift from Dr. Paula Hammond, identity-confirmed by STR profiling, and cultured in RPMI supplemented with 10% FBS and 1% pen-strep. Cell cultures were maintained in a humidified incubator at 37°C with 5% CO_2, and cells with less than 30 passages were used for experiments.

METHOD DETAILS

Antibodies and chemicals

Doxorubicin hydrochloride, SP600125, neocarzinostatin, cisplatin, caffeine, PMA, and anisomycin were purchased from Sigma-Aldrich. PD98059 was purchased from Cell Signaling Technology. SB203580 and mitoxantrone were purchased from Tocris. Doxycycline was purchased from Clontech. The following antibodies were used for immunofluorescence measurements:

Antibody	Vendor	Catalog	Dilution
γ-H2AX	Millipore	05-636	1:200
p-Akt	Cell Signaling Technology	4058	1:200
p-Erk	Cell Signaling Technology	4377	1:200
p-JNK	Cell Signaling Technology	9251	1:100
NF-κB	Santa Cruz	sc-8008	1:50
p-p38	Cell Signaling Technology	4631	1:200
p-S6	Cell Signaling Technology	4856	1:200
p27	Santa Cruz	sc-1641	1:50
p27	Cell Signaling Technology	3686	1:400
p-Hsp27	Cell Signaling Technology	2401	1:200
p53	Santa Cruz	sc-263	1:50
p-c-Jun(Ser 73)	Cell Signaling Technology	9164	1:200
p-c-Jun(Ser 63)	Cell Signaling Technology	9261	1:200
p-Chk2	Cell Signaling Technology	2661	1:200
IκB	BD Biosciences	610691	1:200
IκB	Cell Signaling Technology	4814	1:200
Cyclin D	Santa Cruz	sc-20044	1:50
p-Rb	Cell Signaling Technology	9308	1:200
Cyclin E	Santa Cruz	sc-247	1:50
Cyclin A	Santa Cruz	sc-751	1:50
p21	Millipore	05-345	1:200
p21	Cell Signaling Technology	2947	1:400
p16	Cell Signaling Technology	18769	1:800
Cyclin B	Santa Cruz	sc-752	1:50
Cyclin B	Cell Signaling Technology	12231	1:400
BrdU	BD Biosciences	555627	1:400
BrdU	Cell Signaling Technology	5292S	1:1000

For western blots, the following antibodies were used:

Antibody	Vendor	Catalog	Dilution
p-c-Jun(Ser 73)	Cell Signaling Technology	3270	1:1000
c-Jun	Cell Signaling Technology	9165	1:1000
p-Erk	Cell Signaling Technology	4370	1:2000
Erk	Cell Signaling Technology	4696	1:2000
p-JNK	Cell Signaling Technology	4668	1:1000
JNK	Cell Signaling Technology	9252	1:1000
p-MK2	Cell Signaling Technology	3007	1:1000
MK2	Cell Signaling Technology	3042	1:1000
p-p38	Cell Signaling Technology	4631	1:1000
p38	Cell Signaling Technology	9212	1:1000
p-RPA2(Ser 8)	Cell Signaling Technology	83745	1:1000
RPA2	Cell Signaling Technology	35869	1:1000
β-tubulin	Sigma-Aldrich	T7816	1:2000
GAPDH	Cell Signaling Technology	97166	1:1000

For flow cytometry, the following antibodies were used:

Antibody	Vendor	Catalog	Dilution
Cleaved Caspase-3	BD Biosciences	559565	1:200
Cleaved PARP	BD Biosciences	558710	1:200
Cyclin B	Santa Cruz	sc-752	1:50
p21	Millipore	05-345	1:200
BrdU	BD Biosciences	555627	1:200

The following secondary antibodies were used for both immunofluorescence and flow cytometry in this study:

Antibody	Vendor	Catalog	Dilution
Alexa Fluor 488 goat anti-rabbit	Invitrogen	A-11008	1:200 (CC3)-2000 (BrdU, CycB) for FC, 1:1000 for IF
Alexa Fluor 647 goat anti-rabbit	Invitrogen	A-21245	1:1000 for IF
Alexa Fluor 647 goat anti-mouse	Invitrogen	A-21236	1:2000 for FC, 1:1000 for IF

Doxorubicin treatment for signaling and response measurements

Cells were plated at least 24 hours before treatment in complete culture media. Doxorubicin or DMSO (Sigma-Aldrich) was directly added to culture media, and media was then removed 4 hours later and replaced with media containing 1% fetal bovine serum for the duration of the experiment for immunofluorescence, cell cycle, apoptosis, and proliferation assays.

-galactosidase activity assay

U2OS cells were plated in a 24-well plate 24 hours before doxorubicin treatment in complete media. Doxorubicin was directly added to the culture media, and 4 hours later the media was replaced with media containing 1% FBS for the duration of the experiment. The plate was harvested 4 days after doxorubicin, and the Senescence β-Galactosidase Staining Kit (Cell Signaling Technology) was used according to the manufacturer's protocol. Images were taken on an EVOS fluorescence microscope (ThermoFisher) in the brightfield channel.

Immunofluorescence for BrdU

In experiments where 5-bromo-2'-deoxyuridine (BrdU, ThermoFisher) incorporation into DNA was measured with immunofluorescence, cells were seeded in optical bottom 96-well plates (ThermoFisher) at the beginning of the experiment, and then were incubated in 10 μM BrdU for 24 hours before fixation. Cells were fixed with 4% paraformaldehyde (Electron Microscopy Sciences) for 15 minutes at room temperature, washed 3x with phosphate-buffered saline (PBS, GenClone), and then incubated with 1 N HCl on ice for 10 minutes. Afterwards, the HCl solution was removed, and cells were incubated with 2 N HCl for 10 minutes at room temperature. The HCl was then neutralized with equal amounts of neutralizing buffer [91% sodium phosphate monobasic, 9% citric acid in water], and incubated on cells for 10 minutes at room temperature. Buffer was then removed from the wells, and cells were washed with 1x PBS three times. Afterwards, cells were then permeabilized with PBS containing 0.1% Triton-X (Sigma-Aldrich) for 20 minutes at room temperature. Cells were then incubated with a primary antibody solution containing BrdU antibody diluted 1:400 or 1:1000 in PBS containing 5% goat serum (Abcam,) and 0.1% Triton-X for 1 hour at room temperature. Afterwards, cells were washed 3x with PBS and incubated with an anti-mouse antibody conjugated to Alexa Fluor 647 diluted 1:1000 in PBS for 1 hour at room temperature. Cells were then washed 3x with PBS, and incubated either in HCS CellMask Blue (ThermoFisher) or Hoechst 33342 (Invitrogen, catalog H3570) with Whole Cell Blue (ThermoFisher) according to the manufacturers' protocol. Cells were then washed 3x with PBS, and images were either taken in the DAPI and Cy5 channels using an cellWoRx automated imaging platform (Applied Precision) or in the DAPI and Cy5 channels of an Cellomics ArrayScan VTi (Thermo Fisher).

Detecting EdU incorporation with Click-iT chemistry

U2OS cells were seeded on sterile coverslips coated with poly-L-lysine (Fisher Scientific). The doxorubicin treatment protocol described above was followed, with the exception that media was replaced with 10% FBS media 24 and 72 hours after doxorubicin treatment. 10 μM of 5-ethynyl-2 deoxyuridine (EdU, ThermoFisher) was added to the media 5 days after doxorubicin, and cells were fixed with 4% formaldehyde (Sigma-Aldrich) for 15 minutes at room temperature. Cells were then permeabilized with ice-cold methanol for 10 minutes at -20°C. Cells were then washed with PBS 3x, and coverslips were then transferred to a new 24-well plate. Coverslips were stained with HCS CellMask Blue diluted 1:5000 in PBS for 30 minutes, and then washed 3x in PBS. During CellMask incubation, EdU labeling solution was prepared with Click-iT Plus Alexa Fluor 555 Picolyl Azide Toolkit (ThermoFisher) with the composition according to the manufacturer's instructions, with 2% $CuSO_4$ and 2.5 μM Alexa Fluor 555 picolyl azide. Coverslips

were incubated in EdU labeling solution for 30 minutes at room temperature, and then washed 3x in PBS. Coverslips were then mounted onto glass slides using ProLong Gold Antifade Mount. Slides were then imaged on a Nikon spinning-disk confocal microscope.

Flow cytometry for cell cycle and apoptosis measurements

For all flow cytometry samples, cells were seeded in 15 cm tissue culture dishes 24 hours before doxorubicin treatment. At the indicated time points after doxorubicin treatment, media from the dishes were transferred to 50 mL conical tubes on ice. Cells were then washed with PBS, and afterwards the PBS was added to the respective conical tube (1 tube per plate). Cells were then trypsinized until all cells were detached, and trypsin was subsequently quenched with complete media. Cell suspension was then transferred to the respective conical tube, which was then centrifuged at 1,500 RPM for 5 minutes. The supernatant was then aspirated off, and the cell pellet was resuspended in ice-cold PBS. The cell suspension was then transferred to 1.5 mL Eppendorf tubes, and then centrifuged at 5,000 RPM for 1 minute.

For samples stained for cleaved caspase-3, cleaved PARP, p21, and cyclin B antibody, the pellet supernatant was aspirated, and the cell pellet was resuspended in 4% formaldehyde in PBS and incubated at room temperature for 15 minutes. Formaldehyde solution was removed by centrifuging the cells at 5,000 RPM for 1 minute and removing the supernatant. The cell pellet was then resuspended in ice-cold PBS, and the cell suspension was centrifuged at 5,000 RPM for 1 minute. The supernatant was aspirated off, and cells were resuspended in 90% ice-cold methanol and stored at -20°C until staining. For cleaved caspase-3 and cleaved PARP double staining, cells were washed twice in PBS-T, and then incubated with both antibodies diluted in blocking buffer consisting of 1:1 Odyssey blocking buffer overnight at 4°C, while cells stained for p21 and cyclin B were blocked in blocking buffer for 1 hour at room temperature before proceeding to the overnight primary antibody incubation. For all samples, after the primary antibody step, cells were then washed once with PBS-T, and incubated in respective fluorophore-conjugated secondary antibody diluted in blocking buffer for 1 hour at room temperature for 1 hour. Cells were then washed with PBS-T, and then cleaved caspase-3 and cleaved-PARP stained cells were resuspended in PBS-T for flow cytometry. For the p21 and cyclin B samples, cells were incubated in propidium iodide and RNase A (Cell Signaling Technology) for 1 hour at room temperature before being resuspended in PBS-T for flow cytometry.

For samples stained with BrdU antibody, the pellet supernatant from the ice-cold PBS wash step was aspirated off, and the cell pellet were resuspended in 200 μL ice-cold PBS. 800 μL of ice-cold ethanol was then added drop-by-drop to the Eppendorf tube while vortexing, and samples were then stored at -20°C until staining. Cells were then washed with PBS-T (PBS + 0.5% Tween) and simultaneously permeabilized and denatured with 2 M HCl and 0.5% Triton-X-100 in water for 30 minutes. Cells were washed twice with PBS, and then blocked in blocking buffer consisting of 1:1 Odyssey blocking buffer and PBS-T for 1 hour at room temperature. Blocking buffer was then removed, and cells were then incubated with anti-BrdU antibody diluted in blocking buffer overnight at 4°C. Cells were then washed once in PBS-T, and then were incubated with Alexa Fluor 647 goat anti-mouse antibody diluted in blocking buffer for 1 hour at room temperature. Secondary antibody was removed, and cells were washed once in PBS-T. Cells were then stained with 100 μg/mL propidium iodide with RNase A for 1 hour to visualize DNA content.

All flow cytometry measurements were collected on a BD FacsCaliber flow cytometer (BD Biosciences) or a BD LSR II HTS (BD Biosciences).

Proliferation assay

Cells were seeded at 5,000 cells/well into a tissue culture-treated 96-well plate (ThermoFisher) 24 hours before doxorubicin treatment. Doxorubicin or DMSO was directly added to culture media, and media was changed to media containing 1% FBS media 4 hours after drug addition. The plate was placed back in the incubator, and then 6 hours after doxorubicin treatment was moved to an incubator connected to an Incucyte microscope (Sartorius). Brightfield images of wells were taken 6, 12, 24, 48, 72, and 96 hours after doxorubicin treatment, and cell number was calculated from these images using ilastik software.[162] Proliferation values were normalized across all treatments and time points to the 6 hour DMSO cell count values.

Immunofluorescence measurements for signaling proteins

U2OS cells were seeded into optical bottom 96-well plates (ThermoFisher) 24 hours before doxorubicin treatment. DMSO or doxorubicin were added directly to the media, and then 4 hours later the media was replaced with DMEM containing 1% FBS, which was maintained for the rest of the experiment. At each indicated timepoint, the media was removed and cells were fixed with 4% formaldehyde in PBS for 15 minutes. Cells were then washed with PBS-Tween (PBS-T) once, and then permeabilized with ice-cold methanol for 10 minutes. Afterwards, cells were again washed once with PBS-T, and then blocked in blocking buffer, which consisted of a 1:1 mix of Odyssey blocking buffer (LI-COR Biosciences) and PBS-T. Cells were blocked for 1 hour at room temperature.

Afterwards, the blocking buffer was removed and replaced with primary antibody solution consisting of antibody diluted in blocking buffer. Cells were incubated in primary antibody solution overnight at 4°C on a shaker. The primary antibody solution was then removed, and cells were washed once with PBS-T. Cells were then incubated with a secondary antibody solution containing both goat anti-mouse conjugated to Alexa Fluor 488 and goat anti-rabbit conjugated to Alexa Fluor 647 diluted in blocking buffer. Cells were incubated in secondary antibody solution overnight at 4°C on a shaker, and then washed once with PBS-T. To stain both the nuclear and the cytosolic compartments, cells were incubated with either 1:1000 Whole Cell Blue with 1:10,000 Hoechst 33342 in PBS or 1:5000 HCS CellMask Blue in PBS for 1 hour at 4°C. Cells were then washed with PBS, and wells were replaced

with PBS for imaging. Cells were imaged in the DAPI, GFP, and Cy5 channels on either a cellWoRx automated imaging platform (Applied Precision) or in the DAPI and Cy5 channels of a Cellomics ArrayScan VTi (Thermo Fisher).

Signal and response data processing

To generate the signaling dataset, raw immunofluorescence images were processed in Fiji[160] and subsequently run through a pipeline in CellProfiler for intensity quantification (version 4.0.6).[161] Mean intensity of the nuclear and cytoplasmic compartments (where applicable) of total and phospho-proteins at all time points were normalized to the 2 μM doxorubicin value at the 6 hour time point across a single experiment. The mean of all biological replicates across experiments for each signal was used for subsequent data visualization and modeling.

The response dataset consisted of normalized fold-change data for the proliferation measurements, and percent positive as gated in flow cytometry for the rest of the response measurements collected. The mean was calculated for each individual response and time point across all biological replicates and experiments. Then, percent positive measurements were divided by 100 to scale values between 0 and 1, and a logit transformation was applied to all data points. Values of 0 were converted to 0.00001 for the logit transformation.

For principal component analysis (PCA), the normalized signals data was shaped into a 4x156 matrix, with rows representing the 4 distinct treatments and columns representing individual signals (26) and time points (6). The z-score was taken of this 4x156 matrix, which was used for principal component analysis.

For tensor PLSR, the raw signal data (X) was shaped into a 4x6x26 tensor, with mode 1 representing treatments (n = 4), mode 2 representing time points (n = 6), and mode 3 representing each individual signal (n = 26). The response data (Y) was shaped into a 4x6x10 tensor, with the same modes 1 and 2, and mode 3 representing individual responses (n = 10).

Tensor PLSR and VIP score calculation

The X and Y tensors were mean-centered across mode 1 and variance scaled across modes 2 and 3. The tensor PLSR model was constructed in MATLAB 2019b using the N-way Toolbox (version 1.8.0.0) as described in Chitforoushzadeh et al.[55] All scripts and packages are available for download from the Github repository listed in the "data and code availability" statement.

The VIP scores were calculated as described in Favilla et al.[58,163] using the Multi-Way VIP package in MATLAB.[58]

Principal component analysis

The z-scored signaling matrix of 4 x 156 was run through the pca() function in MATLAB using three principal components and with no additional centering. Scores and loadings were plotted on principal components one and two, as these explained the majority of the variance in the signals (> 70%). All of the scores and loadings of PC 2 were multiplied by -1 to improve the interpretability in comparison to the t-PLSR results. To calculate the senescence and apoptosis projections of PCA loadings, the angle between the respective axis and the PCA loading vector was calculated, and then the cosine of this value was calculated. See the code on the Github repository for more details.

Inhibitor co-treatment experiments

Cells were seeded at 5,000 cells/well into an optical bottom 96-well plate (ThermoFisher, catalog 165305) 24 hours before doxorubicin treatment. For the 0-12 hour inhibitor pulse, cells were treated with either vehicle (DMSO) or doxorubicin in addition to 10 μM SP600125, 10 μM PD98059, 10 μM SB203580, caffeine (5 mM for U2OS cells and 1 mM for OVCAR-8 cells), or vehicle (DMSO). Cells were maintained in this media for 4 hours, and then media was replaced with 1% FBS media containing either the respective inhibitor or vehicle, media was replaced with 10% FBS media 1 and 3 days after doxorubicin treatment, and inhibitor was maintained for the entire experiment for the results seen in Figures 5G–5I. For Figures 6 and S6, 12 hours after the addition of doxorubicin, the media was replaced with 1% FBS media containing no inhibitors or vehicle. For the 12-24 hour inhibitor pulse, cells were treated with either vehicle (DMSO) or doxorubicin for 4 hours in the absence of inhibitors, and then the media was replaced with 1% FBS media. 12 hours after the addition of doxorubicin, the media was replaced with media containing the above inhibitors at the listed concentrations. Media was replaced with 10% FBS media 1 day and 3 days after the addition of doxorubicin for both the 0-12 and the 12-24 hour inhibitor condition. 5 days after the addition of doxorubicin, 10 μM BrdU was added to all wells, and 24 hours later plates were harvested for BrdU immunofluorescence, which was performed as described above.

ELISA for IL-6 and IL-8

U2OS cells were seeded at 5,000 cells/well into a 96-well plate 24 hours before doxorubicin treatment. Cells were treated with either vehicle or doxorubicin for 4 hours, and then media was replaced with drug-free, 1% FBS media. 24 hours after the addition of doxorubicin, media was replaced with 10% FBS media. Three days after doxorubicin addition, 10% FBS media containing either vehicle (DMSO), 10 μM SP600125, or 10 μM PD98059 was used to replace the growth media. Five days after doxorubicin treatment, the media was changed in wells to media without serum, and six days after doxorubicin treatment, media was transferred to a v-bottom 96-well plate, and stored at -80°C. ELISA assays for IL-6 (Invitrogen) and IL-8 (Invitrogen) levels in the media samples were conducted according to the manufacturer's protocol.

Western blotting

Cells were treated as indicated in 6-well plates. At the given time points, the culture media was aspirated and cells were immediately lysed on ice. For the siRNA knockdown blots, RIPA buffer [50 mM Tris-HCl (pH 8), 150 mM NaCl, 0.1% sodium dodecyl sulfate (SDS), 0.5% sodium deoxycholate, 1% Triton-X] was used, while for the rest of the shown blots high SDS (0.7%) lysis buffer [10 mM Tris (pH 7.5), 50 mM NaCl, 0.5% NP-40, 0.5% sodium deoxycholate, 0.7% SDS, 10 mM iodoacetamide] was used. Both types of lysis buffer were supplemented with phosSTOP (Roche, catalog 4906837001) and cOmplete (Roche, catalog 5892791001) tabs. 100 μL of lysis buffer was added to each well after aspiration, and afterwards was evenly distributed within the well. The plate was then incubated on ice for 5 minutes, and a cell scraper was used to scrape remaining cells while the plate was still on ice. The lysates were transferred to a cold Eppendorf tube and subsequently sonicated and centrifuged at 18,000 x g for 10 minutes at 4°C for the RIPA buffer lysates. For the high SDS lysates, lysates were vortexed for 15 seconds and then put back on ice for 10 minutes after the sonication step. This vortexing step was repeated twice for a total of 30 minutes, and then lysates were centrifuged at 18,000 x g for 10 minutes at 4°C. After centrifugation, the supernatants were transferred over to a new, pre-chilled Eppendorf tube and stored at -20°C.

The protein concentration of lysates was measured using a BCA assay (ThermoFisher), and the protein concentration was normalized across all samples. Samples were boiled for 5 minutes in 1x sample buffer [34 mM Tris, pH 6.8, 7% glycerol, 500 mM 2-mercaptoethanol, 1.6% SDS], and then loaded on a 10% SDS PAGE gel. After the samples ran through the gel at 100 V, a wet transfer step was run at 100 V for 1 hour at 4°C to transfer protein to a 0.22 μM nitrocellulose membrane. The quality of the transfer was checked with a Ponceau staining (Sigma-Aldrich), and after destaining the membranes were blocked in a blocking buffer consisting of a 1:1 mix of Intercept Blocking Buffer (LI-COR Biosciences) and PBS-T (PBS + 0.05% Tween) at room temperature for 1 hour on a shaker. Primary antibody was diluted in blocking buffer, and incubated with the membrane overnight at 4°C on a shaker. The membrane was then washed five times quickly with PBS-T, and then washed three times for 5 minutes each in PBS-T on a shaker at room temperature. Membranes were then incubated with secondary antibody (LI-COR Biosciences) diluted in blocking buffer for 1 hour at room temperature on a shaker, and afterwards the same wash steps as described above were performed, with the exception that the last wash step was conducted with PBS instead of PBS-T. Membranes were then kept in PBS, and then imaged in the 680 and 800 channel of an Odyssey CLx machine (LI-COR-Biosciences). The mean, background subtracted signal intensity of respective bands were quantified in Image Studio Lite (LI-COR Biosciences, version 5.2), and intensity values were used for described ratio calculations.

For blots of phospho and total c-Jun, JNK, and RPA2 the blot was probed first using the phospho antibody, and then the membrane was stripped with 1x NewBlot nitrocellulose stripping buffer (LI-COR Biosciences), washed 5x quickly in PBS, and then washed three times for 10 minutes each in PBS on a shaker at room temperature. The membrane was then blocked again in 1:1 Odyssey blocking buffer to PBS-T, and reprobed with the total antibody on a shaker overnight at 4°C. The total MK2 blots were stripped and reprobed for p38 as described above on the same membrane, which was also done for the p-MK2 blots with p-p38.

siRNA transfection

Non-targeting (catalog AM4636) was purchased from Invitrogen, and Jun 1 (catalog s7658),and Jun 2 (catalog s7659) siRNAs were purchased from Life Technologies. U2OS cells were plated in 6-well plates at a density of 150,000 cells/well 24 hours prior to transfection. Lipofectamine RNAiMAX was purchased from ThermoFisher Scientific, and used according to the manufacturer's protocol to dose cells with 10 nM of siRNA-Lipofectamine duplex. Cells were incubated in siRNA/Lipofectamine mixture for 24 hours, and then each well was seeded into a 96-well plate at a density of 5,000 cells/well in triplicate. A concurrent 6-well plate transfected with siRNAs had media changed 24 hours post-transfection, and cells were harvested for immunoblotting 48 hours after transfection.

Cells in the 96-well plate were treated with doxorubicin 24 hours after seeding, and media was changed to media containing 1% FBS 4 hours after doxorubicin treatment. 24 hours after doxorubicin treatment, media was changed to complete media containing 10% FBS. Immunofluorescence for BrdU was conducted six days after doxorubicin treatment, as described above.

Cloning and Tol2-mediated stable transfection

pAK-Tol2-TRE-JunDN-HA-T2A-GFP (pTRE-JunDN-HA-T2A-GFP) construct was assembled using Gibson assembly with NEBuilder HiFi DNA Assembly Master Mix (NEB) and inserted into a lentiviral pLVX-CMV empty backbone. pMIEG3-JunDN was a gift from Alexander Dent (Addgene plasmid 40350; http://n2t.net/addgene:40350; RRID:Addgene_40350),[156] and was used as a template to amplify JunDN-HA and GFP fragments used in the assembly. JunDN-HA-T2A-GFP was amplified from the pLVX-CMV backbone using Phusion Mastermix (NEB), and inserted into the empty backbone of pAK_Tol2_TRE_Puro (Addgene, plasmid 130259) with digestion and ligation cloning into the NheI (NEB) and EcoRI (NEB) sites. GFP amplified from pLVX-CMV-JunDN-HA-T2A-GFP was inserted as described above into the same backbone for the TRE-GFP control construct. Positive colonies for both plasmids were confirmed with Sanger sequencing.

U2OS cells were seeded at a density of 200,000 cells/well into a 6-well plate 24 hours before transfection. Cells were co-transfected with 1.25 μg pCMV-Tol2 and 1.25 μg of either pAK-Tol2-TRE-JunDN-HA-T2A-GFP or pAK-Tol2-TRE-GFP (pTRE-GFP) with Lipofectamine 2000 (ThermoFisher Scientific) according to the manufacturer's instructions at a 1:2 DNA (μg) to Lipofectamine 2000 reagent (μL) ratio. Media was replaced 24 hours later, and cells were selected with 2 μg/mL puromycin (Invivogen) 96 hours post-transfection for 3 days. Cells were then induced with 1 μg/mL doxycycline for 3 days, and GFP positive cells were harvested by FACS using a BD FACSAria III machine (BD Biosciences) for further experiments.

c-Jun dominant negative experiments

U2OS cells stably expressing either the pTRE-GFP or the pTRE-JunDN-HA-T2A-GFP construct and were FACS-sorted for GFP positivity as described above were seeded in a 96-well plate at 1,000 cells/well 96 hours before doxorubicin treatment. 72 hours before doxorubicin treatment, media was changed to complete media with or without 1 μg/mL doxycycline. 24 hours before doxorubicin treatment, media was changed again to complete media with or without 1 μg/mL doxycycline. Doxorubicin or DMSO was added directly to the wells, and media was changed to media containing 1% FBS with or without 1 μg/mL doxycycline. 12 hours after doxorubicin treatment, media was changed to media containing 1% FBS without doxycycline, and 24 and 72 hours after doxorubicin treatment, the media was changed to complete media containing 10% FBS. Immunofluorescence for BrdU was conducted as described above.

Retrovirus production and transduction

pSIRV-AP-1-mCherry was a gift from Peter Steinberger (Addgene plasmid 118095; http://n2t.net/addgene:118095; RRID:Addgene_118095),[158] and pUMVC was a gift from Bob Weinberg (Addgene plasmid 8449; http://n2t.net/addgene:8449; RRID:Addgene_8449).[159] HEK293T cells were co-transfected with 15 μg pSIRV-AP-1-mCherry, 10 μg pUMVC, and 2.5 μg pCMV-VSVG using the calcium phosphate transfection system (Clonetech), and media was changed 24 hours later. Media was harvested 24 hours after the media changed, and filtered through a 0.45 μm filter with a syringe. Filtered media was given to U2OS cells for 24 hours, and two weeks post-transduction, mCherry positive cells were harvested by FACS using a BD FACSAria III machine (BD Biosciences) for further experiments.

To generate U2OS cells containing both AP-1-mCherry and JunDN-IRES-eGFP, FACS-sorted AP-1-mCherry cells from above were infected with pMIEG3-JunDN construct packaged in retrovirus. pMIEG3-JunDN was packaged with HEK293Ts as described above, and filtered media containing virus was diluted 1:1 into complete media. U2OS cells were incubated with virus for 24 hours, and two weeks later, a GFP high population was harvested by FACS for further experiments using a BD FACSAria III machine (BD Biosciences).

AP-1-mCherry experiments

U2OS cells stably transfected with the AP-1 mCherry reporter were seeded into 6-well plates at a density of 150,000 cells/mL 24 hours before treatment. Cells were treated with either DMSO or doxorubicin for 4 hours, and then media was replaced with DMEM containing 1% FBS. For the entire experiment, cells were co-treated with either DMSO, 10 μM SP600125, or 10 μM PD98059. AP-1-mCherry cells co-expressing JunDN-IRES-GFP were also treated with either DMSO or doxorubicin. As a positive control, AP-1-mCherry cells were treated with 100 nM phorbol 12-myristate 13-actetate (PMA) for 24 hours and was administered at the same time as the doxorubicin. Cells were harvested 24 hours after treatment, and flow cytometry was performed using a BD LSR II HTS flow cytometer (BD Biosciences).

Software

For image processing, either Fiji or NIS Viewer were used. CellProfiler was used for downstream image quantification, and FlowJo v10 was used to process flow cytometry-based response data. For Incucyte-based proliferation data, ilastik was used to count the number of cells in brightfield images. MATLAB 2019b was used for modeling and PCA analysis, and Python 3.7 was used to analyze and compile CellProfiler outputs as well as generate boxplots. All cartoon illustrations were made directly in Adobe Illustrator, or by using BioRender under an academic license. Publication licenses are available upon request.

QUANTIFICATION AND STATISTICAL ANALYSIS

All statistical testing was performed in GraphPad Prism (version 8.4.1), which specific tests performed listed in the relevant figure caption. Data was quantified as described in in the respective method subsections and/or captions.

Cell Systems Volume *4*

Supplemental information

Biphasic JNK-Erk signaling separates the induction and maintenance of cell senescence after DNA damage induced by topoisomerase II inhibition

Tatiana S. Netter eld Gerard J. Ostheimer Andrea R. Tentner Brian A. Joughin Alexandra M. Dakoyannis Charvi D. Sharma Peter K. Sorger Kevin A. Janes Douglas A. Lauffenburger and Michael B. Yaffe

Netterfield et al., Figure S1

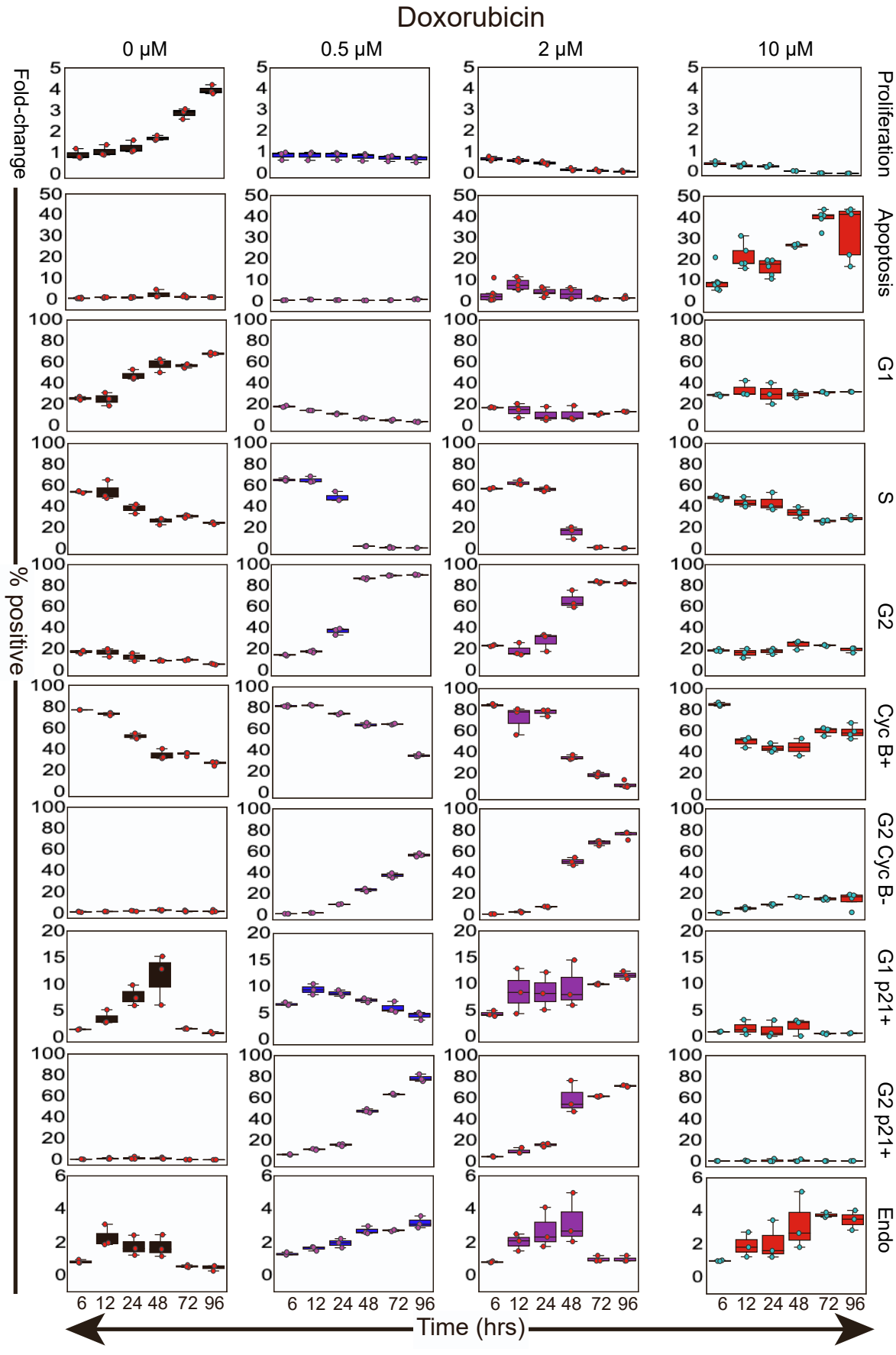

Figure S1: Boxplots of raw response data.

Boxplots of raw response data vs. time. Y-axis values represent fold-change for proliferation values, and percent positive values for responses measured by flow cytometry. Overlaid dots represent individual biological replicates.

Netterfield et al., Figure S2

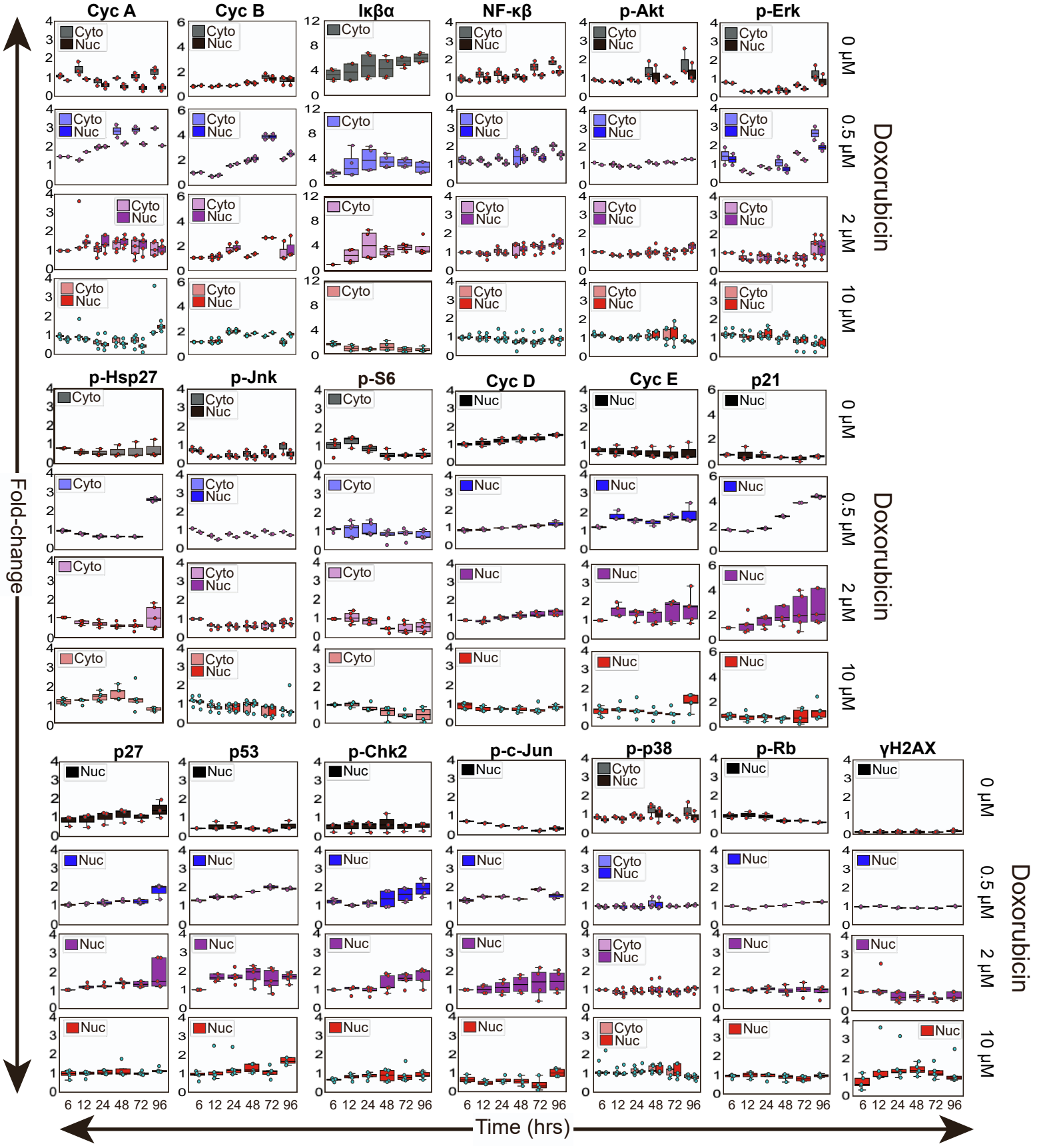

Figure S2: Boxplots of raw signals data.

Boxplots of raw signals data vs. time. Y-axis values represent fold-change of the mean intensity normalized to the 2 μM dose at the 6 hour timepoint for both the nuclear (Nuc) and cytoplasmic (Cyto) compartments. Overlaid dots represent individual biological replicates.

Netterfield et al., Figure S3

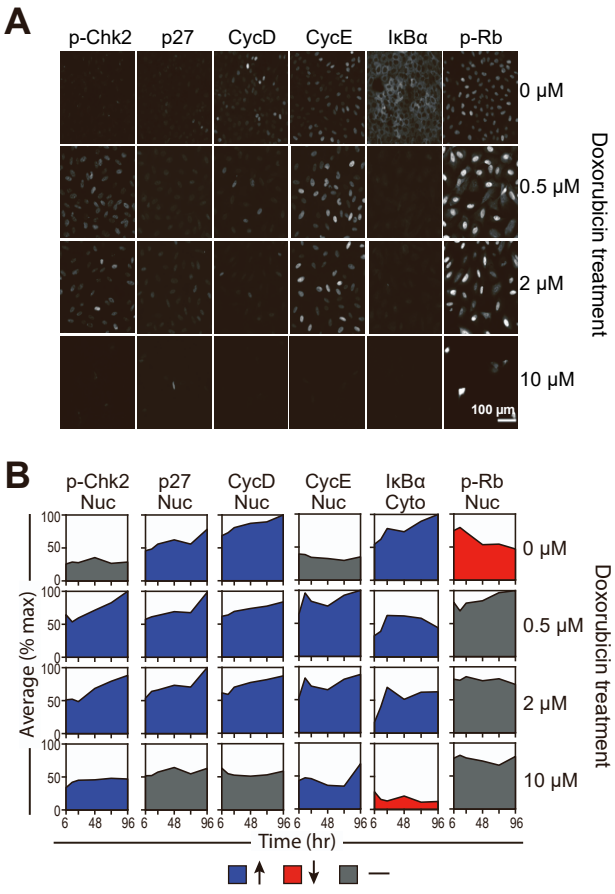

Figure S3: Quantification of remaining signaling measurements.

A) Representative immunofluorescence images of remaining signals not shown in figure 3.

B) Quantification of the mean fluorescence intensity (normalized to the maximum value across time and drug treatments) over time in either the nuclear or cytoplasmic compartment, depending on the given protein measured. Tick marks on the x-axis represent 6, 24, 48, 72, and 96 hrs. Images are representative of 250-6,000 individual cells per biological replicate, depending on the dose of doxorubicin.

Netterfield et al., Figure S4

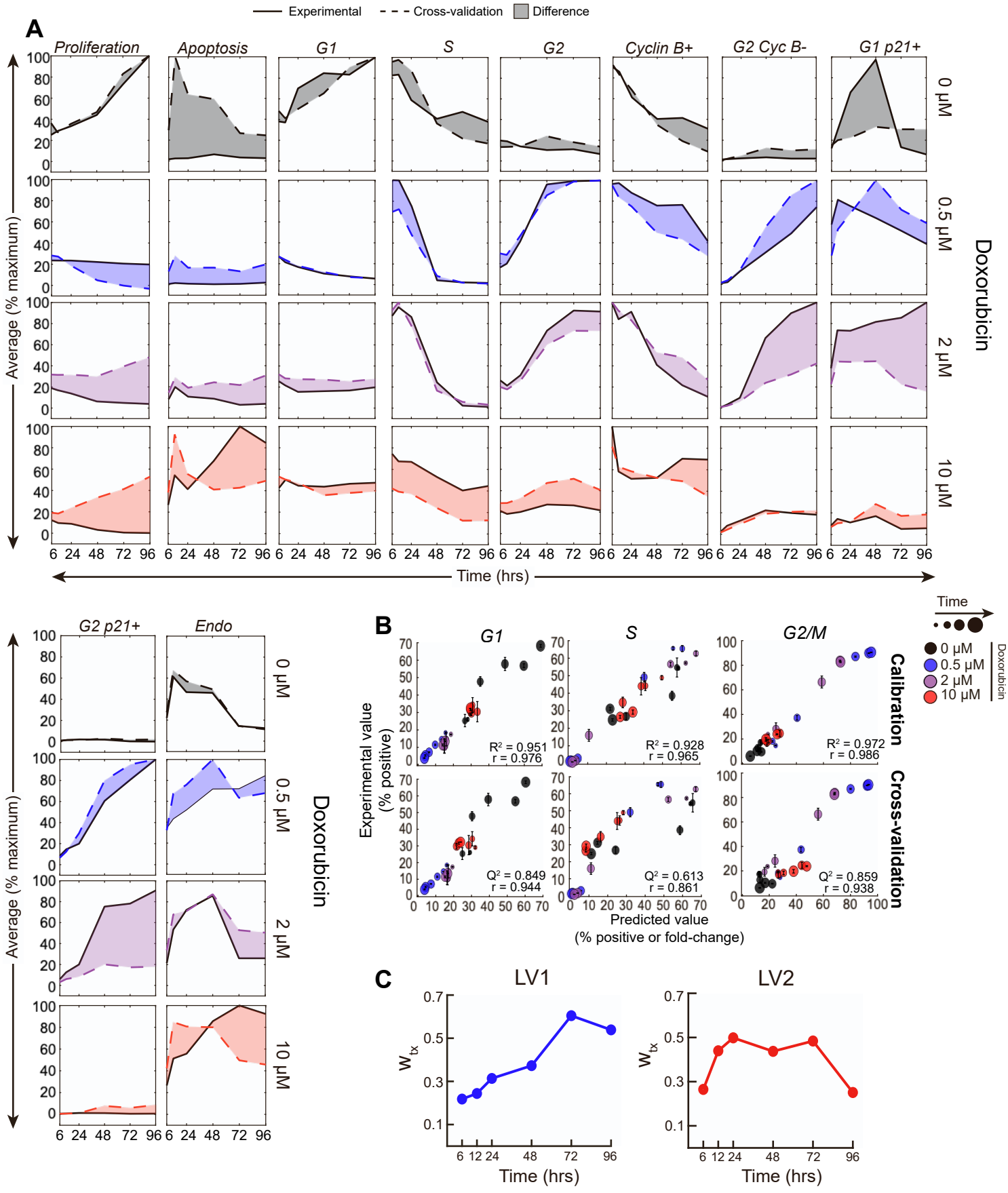

Figure S4: Constructed t-PLSR model can most accurately predict cell cycle distributions, and time weights reveal which timepoints are most heavily weighted on constructed LVs.

A) The mean fluorescence intensity (normalized to the maximum value across time and drug treatments) vs. time is plotted for each of the predicted responses, with the solid lines representing the experimental values, the dotted lines representing the cross-validation predictions, and the shaded area highlighting the difference between the two curves.

B) Experimental vs. predicted values of the G1, S, and G2 responses from the calibration and cross-validation model. R^2, Q^2, and Pearson correlation values are also shown. Dot sizes increase with time.

C) Calibration model time weights (w_{tx}) for LV1 (blue curve, left panel) and LV2 (red curve, right panel).

Netterfield et al., Figure S5

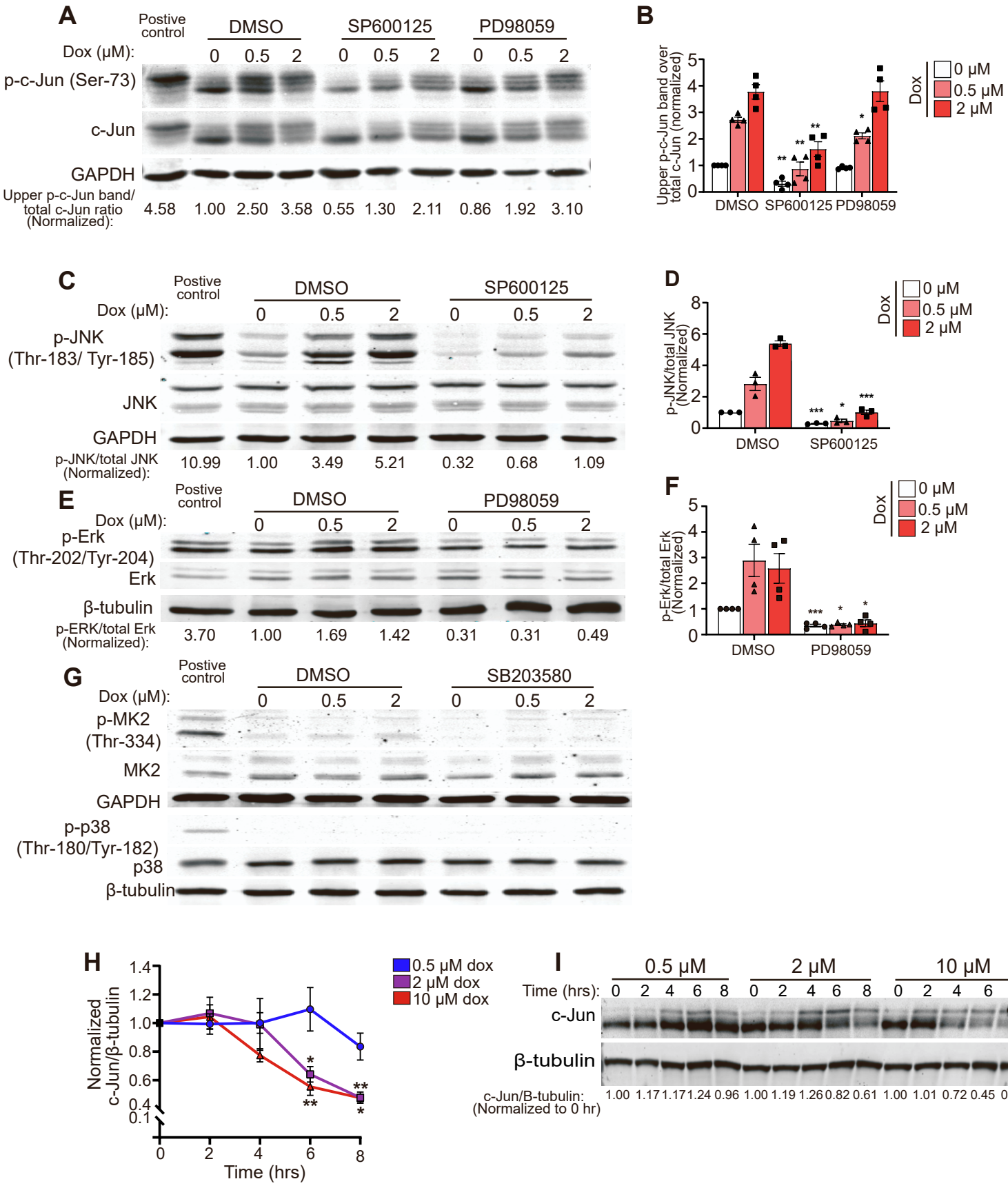

Figure S5: Western blotting data of components of the JNK, Erk, and p38MAPK pathways with or without SP600125, PD98059, or SB203580.

A) Representative western blot probed for p-c-Jun (Ser-73), c-Jun, and GAPDH in U2OS cells that were treated with doxorubicin for four hours, and cells were either co-treated with vehicle (DMSO), or with either 10 μM SP600125 (SP, JNKi) or 10 μM PD98059 (PD, Meki). Cells were lysed 6 hours after doxorubicin treatment for western blotting. Samples were run with a positive control of U2OS cells treated with 25 μg/mL anisomycin for 15 minutes.

B) Quantification of the ratio of the upper p-c-Jun(Ser-73) band to total c-Jun. Bars represent the mean ± SEM of four biological replicates, and bars represent SEM

C) Representative western blot of p-JNK (Thr-183/Tyr-185), JNK, and GAPDH in U2OS cells that were treated with either vehicle (0 μM) or doxorubicin (0.5 μM and 2 μM) for four hours, and cells were either co-treated with vehicle (DMSO), SP600125 (SP, JNKi) or PD98059 (PD, Meki. Samples were run with a positive control of U2OS cells treated with 25 μg/mL anisomycin for 15 minutes.

D) Quantification of p-JNK to total JNK ratio, normalized to DMSO, 0 μM condition. Bars represent mean ± SEM of three biological replicates.

E) Representative western blot of p-Erk (Thr-202/Tyr-204), Erk1/2, and β-tubulin in U2OS samples in the same treatment conditions as subpanel A. Samples were run with a positive control of 100 nM PMA treatment for 30 minutes.

F) Quantification of p-Erk to total Erk1/2 ratio, normalized to DMSO, 0 μM condition. Bars represent mean ± SEM of four biological replicates. Western blots are representative of two biological replicates. ***: $p < 0.001$, **: $p < 0.01$, *: $p < 0.05$ with a two-tailed t-test with Bonferroni correction tested vs. the respective doxorubicin dose in the vehicle inhibitor control in subpanels B, D, and F.

G) Representative western blots of p-MK2 (Thr-334), MK2, p-p38 (Thr180/Tyr-182), p38, GAPDH, and β-tubulin in in U2OS cells that were treated with either vehicle (0 μM) or doxorubicin (0.5 μM and 2 μM) for four hours, and cells were either co-treated with vehicle (DMSO), or SB203580 (SB, p38i). Samples were run with a positive control of U2OS cells treated with 25 μg/mL anisomycin for 15 minutes.

H) Quantification of total c-Jun over β-tubulin after treatment with either 0.5 μM, 2 μM, or 10 μM doxorubicin normalized to 0 hour timepoint. Media was replaced with drug free 1% FBS media at

the 4 hour timepoint. Points represent mean ± SEM of four biological replicates of three or four biological replicates. **: $p < 0.01$, *: $p < 0.05$ vs. the 0.5 μM dose with a one-way ANOVA and post-hoc Tukey's post-hoc test.

I) Representative western blot of total c-Jun and β-tubulin after treatment with either 0.5 μM, 2 μM, or 10 μM doxorubicin normalized to 0 hour timepoint.

Netterfield et al., Figure S6

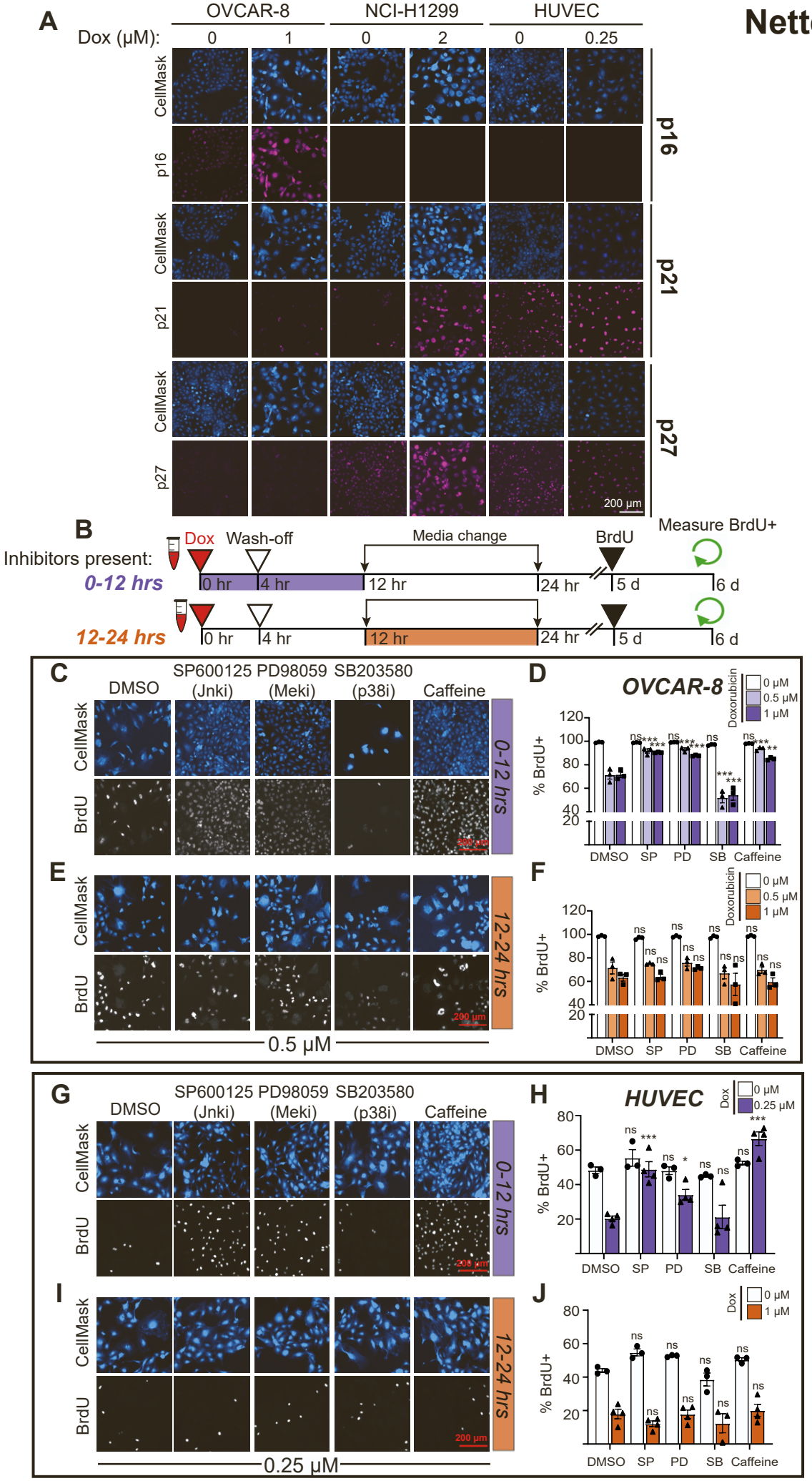

Figure S6: OVCAR-8 and HUVEC cells make the early decision to senesce through the JNK and Erk pathways, and overexpress CDK inhibitors p16, p21, or p27.

A) Representative immunofluorescence for p16, p21, and p27 (magenta) in OVCAR-8, NCIH1299, and HUVEC cells four days after a 4 hour pulse of vehicle of doxorubicin. Cells were also stained for CellMask blue to visualize cell morphology (blue). Scale bar represents 200 μm. Images are representative of 100-300 individual cells, depending on the dose of doxorubicin.
B) Schematic of inhibitor pulse experiment, as seen in figure 6A.
C) Representative immunofluorescence (IF) of BrdU incorporation into DNA in OVCAR-8 cells treated with inhibitors (10 μM for SP600125, PD98059, and SB203580 drugs, and 1 mM of caffeine) for 0-12 hrs and co-stained with HCS CellMask Blue. Scale bar represents 200 μm. Images are representative of about 1,500-7,500 individual cells per biological replicate, depending on condition.
D) Quantification of the percent of nuclear BrdU+ in OVCAR-8 cells after the 0-12 hour inhibitor condition.
E) Representative IF of BrdU incorporation into DNA in OVCAR-8 cells treated with inhibitors for 12-24 hrs and co-stained with HCS CellMask Blue. Scale bar represents 200 μm. Images are representative of 1,500-7,500 individual cells per biological replicate, depending on condition.
F) Quantification of the percent of nuclear BrdU+ in OVCAR-8 cells after the 12-24 hour inhibitor condition.
G) Representative immunofluorescence (IF) of BrdU incorporation into DNA in HUVEC cells treated with inhibitors (10 μM for SP600125, and SB203580 drugs, 5 μM for PD98059, and 1 mM of caffeine) for 0-12 hrs and co-stained with HCS CellMask Blue. Scale bar represents 200 μm. Images are representative of 7,000-18,000 individual cells per biological replicate, depending on condition.
H) Quantification of the percent of nuclear BrdU+ in HUVEC cells after the 0-12 hour inhibitor condition.
I) Representative IF of BrdU incorporation into DNA in HUVEC cells treated with inhibitors for 12-24 hrs and co-stained with HCS CellMask Blue. Images are representative of 7,000-18,000 individual cells per biological replicate, depending on condition.
J) Quantification of the percent of nuclear BrdU+ in HUVEC cells after the 0-12 hour inhibitor condition. For all bar graphs, bars represent mean ± SEM of three or four biological replicates.

***: $p < 0.001$, **: $p < 0.01$ *: $p < 0.05$ with a two-way ANOVA and post-hoc Dunnett's test for subpanels D, F, H, and J. All comparisons were vs. the DMSO treatment at the same dose of doxorubicin.

Netterfield et al., Figure S7

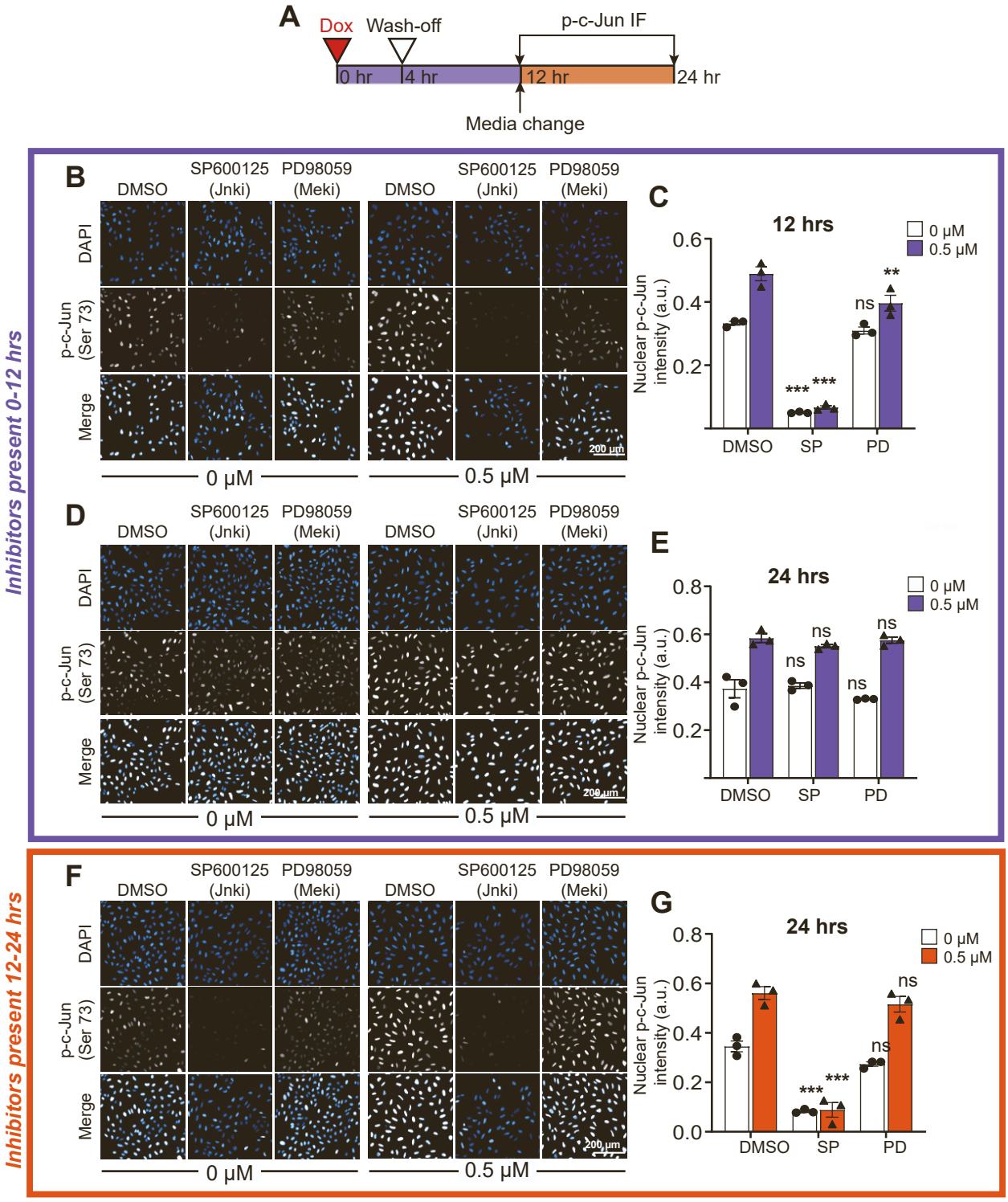

Figure S7: Time course of p-c-Jun(Ser 73) show inhibitor-dependent decreases in phosphorylation levels in the first 12 hours after doxorubicin treatment in U2OS cells.

A) Schematic of the experiment performed.

B) Representative images of cells immuno-stained for p-c-Jun(Ser-73) and DAPI co-treated with inhibitors the first 12 hours of the experiment, and fixed at the 12 hour timepoint. Images are representative of 1,500-2,500 individual cells per biological replicate, depending on the condition.

C) Quantification of the nuclear mean p-c-Jun(Ser-73) intensity 12 hour timepoint.

D) Representative images of cells immune-stained for p-c-Jun(Ser-73) and DAPI co-treated with inhibitors the first 12 hours of the experiment, and fixed at the 24 hour timepoint. Images are representative of 1,500-4,0000 individual cells per biological replicate, depending on the condition.

E) Quantification of the nuclear mean p-c-Jun(Ser-73) intensity for the 24 hour timepoint after early inhibitor.

F) Representative images of cells immune-stained for p-c-Jun(Ser-73) and DAPI co-treated with inhibitors the 12-24 hour window of the experiment, and fixed at the 24 hour timepoint. Images are representative of 1,500-4,000 individual cells per biological replicate, depending on the condition.

G) Quantification of the nuclear mean p-c-Jun(Ser-73) intensity for the 24 hour timepoint after late inhibitor. For subpanels C, E, and G, bars represent the mean ± SEM of three biological replicates. ***: $p < 0.001$ **: $p < 0.01$ with a two-way ANOVA and post-hoc Dunnett's test when compared to the DMSO vehicle control at the same doxorubicin dose.

Netterfield et al., Figure S8

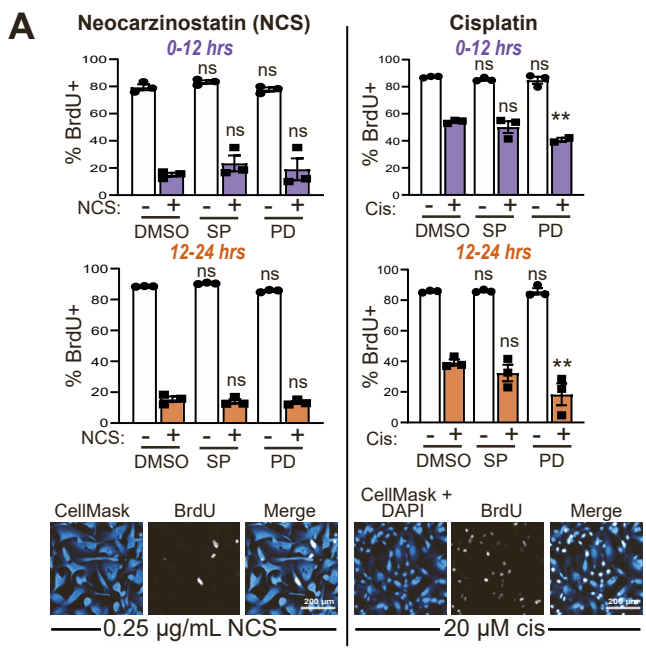

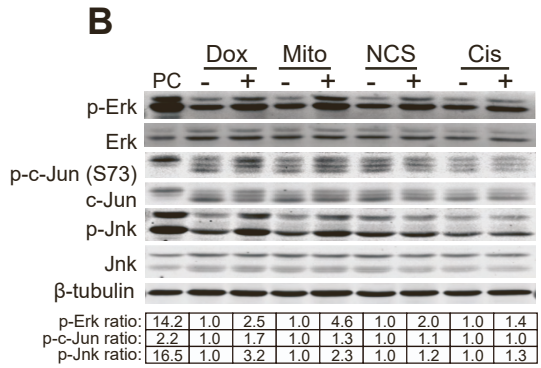

p-Erk ratio:	14.2	1.0	2.5	1.0	4.6	1.0	2.0	1.0	1.4
p-c-Jun ratio:	2.2	1.0	1.7	1.0	1.3	1.0	1.1	1.0	1.0
p-Jnk ratio:	16.5	1.0	3.2	1.0	2.3	1.0	1.2	1.0	1.3

Figure S8: Neocarzinostatin and cisplatin treatment do not respond to SP600125 or PD98059, induce replications stress, or activation of the JNK and Erk pathways

A) Immunofluorescence images and quantification of SP600125 and PD98059 inhibitor pulse experiments (similar experimental details as in fig 6A-I) with either 4 hour pulse of 0.25 μg/mL neocarzinostatin (NCS), 20 μM cisplatin (+) or vehicle (-). U2OS cells were stained with anti-BrdU and HCS CellMask Blue six days after mitoxantrone treatment, with quantification of nuclear BrdU positivity six days after drug treatments. Bars represent the mean ± SEM of three biological replicates. CellMask blue was visualized with gamma=0.6 in order to better visualize the nuclear and cytoplasmic compartments. Images are representative of 5,500-31,000 individual cells per biological replicate, depending on the condition.

B) Representative western blots for phospho and total JNK, Erk, and c-Jun 6 hours after the addition of drug. The positive controls for phospho- JNK and c-Jun was treatment with 25 μg/mL anisomycin for 15 minutes, and the positive control for phosphor-Erk was 100 nM PMA for 30 minutes. Blots are representative of four experiments. See figure 7J for quantification across biological replicates.